New occurrence of Ag-Hg-Cu mineralization in the Tassafte area, NE edge of the Saghro inlier, Ediacaran-Cambrian transition (Eastern Anti-Atlas, Morocco)

Z. Yajioui, L. Badra, A. Mahmoudi
Department of Geology, Faculty of Sciences, Moulay Ismail University, Meknes, Morocco

A. Lima
Departamento de Geociências, Ambiente e Ordenamento do Território, Faculdade de Ciências da Universidade do Porto

B. Karaoui
Faculty of Sciences and Techniques, Moulay Ismail University, Errachidia, Morocco

Abstract. The Tassafte Ag-Hg-Cu mineralization, located about 20 km to the East of Imiter Mine (Ag, Hg), at the NE edge of Saghro inlier, Eastern Anti-Atlas, represents a key zone to study and understand the mineralization history in the Anti-Atlas belt. It exposes E-W-oriented polymetallic mineralization veins hosted within Ediacaran formations and throughout Cambrian formations. The main metallic minerals are represented by argentite, amalgam of Ag-Hg and rarely native silver; copper minerals mainly comprise chalcopyrite, chalcocite, covellite, bornite, and copper oxides. The gangue minerals are mainly constituted by quartz and barite. Preliminary results of our finding show that the Ag-Hg-Cu mineralization in the NE of the Saghro inlier is presumably younger than what has been assumed previously. The mineralization is probably related to the Variscan to Alpine orogenies.

1 Introduction

The Anti-Atlas in Morocco consists of Paleozoic cover overlying Precambrian basement which is exposed within several inliers: Bas Draâ, Ifni, Kerdous, Tagragra-Akka, Agadir Melloul-Iguerda, Igherm, Zenaga, Siroua, Bou Azzer, Saghro and Ougnat (Fig. 1-A). These mountains are considered as a large metallogenic province for mineral exploration and exploitation (Bouchta et al. 1977; Mouttaqi et al. 2011), positioned at the NW margin of the West African Craton. Its evolution was related to a poly-phase tectono-magmatic history (from Eburnean to Alpine orogeny).

In the Eastern Anti-Atlas, the Saghro inlier is composed of meta-sedimentary Cryogenian basement that crops out in restricted areas know as Imiter-, Sidi Feleh-, Bou Skour-, Kelaa Megouna sub-inlier. The Ediacaran Ouarzazate supergroup consists of volcano-sedimentary successions overlying the basement (Gasquet et al. 2005; Tuduri et al., 2018). This supergroup itself is overlain by Cambrian sedimentary series. The Saghro inlier contains several ore deposits of precious and base metals, such as Imiter- (Ag-Hg), Tiouit- (Au-Cu), Thaghassa- (Au-Ag), and Bou Skour mine (Cu) (Mouttaqi et al. 2011; Tuduri et al. 2018). The mineralizations are hosted within Cryogenian meta-sediments and Ediacaran volcano-sedimentary rocks (Fig.1-B).

Previous studies argued that the mineralization events in the Eastern Anti-Atlas are linked to the extensional regime during late Ediacaran magmatic activities (Levresse 2001; Cheilletz et al. 2002; Gasquet et al. 2005; Bouabdellah and Slack 2016). However, recent data reported from the Imiter mine indicate a younger age for the silver mineralization and it is assumed to be related to the CAMP (Central Atlantic Magmatic Province; Triassic-Jurassic transition) magmatism during the opening of the central Atlantic ocean (Borisenko et al. 2014; Essarraj et al. 2016).

The current work reports for the first time on an Ag-Hg-Cu mineralization in the Tassafte mining district (Eastern Anti-Atlas belt), where the mineralization is hosted within both, Ediacaran and Cambrian formations.

2 Results

The Tassafte mining district is located at the NE edge of the Saghro inlier, about 25 km to the South of Tinghir city and 20 km to the East of the Imiter mine. In this area, two lithostratigraphic units were distinguished (Fig. 2), which correspond to the Ediacaran complex in the southern sector and to Cambrian formations in the northern part.

2.1 Country rocks

In the Tassafte area, the ore veins are hosted within Precambrian to Cambrian formations. The Precambrian is presented by Ediacaran volcano-sedimentary succession in which different lithofacies are identified that comprise rhyolitic ignimbrite, basalt to andesite lava, fallout deposit and a hydroclastic complex. These rocks are unconformably overlain by Cambrian sediments. The lower Cambrian comprises the Igoudine Formation, composed of polygenic conglomerates, the Imouslek\Issafene Formations that consist of alternating carbonates and shales, and fine quartzite beds that represent the Asrir formation. The Middle Cambrian is

composed by greenish shale that represents the Jbel

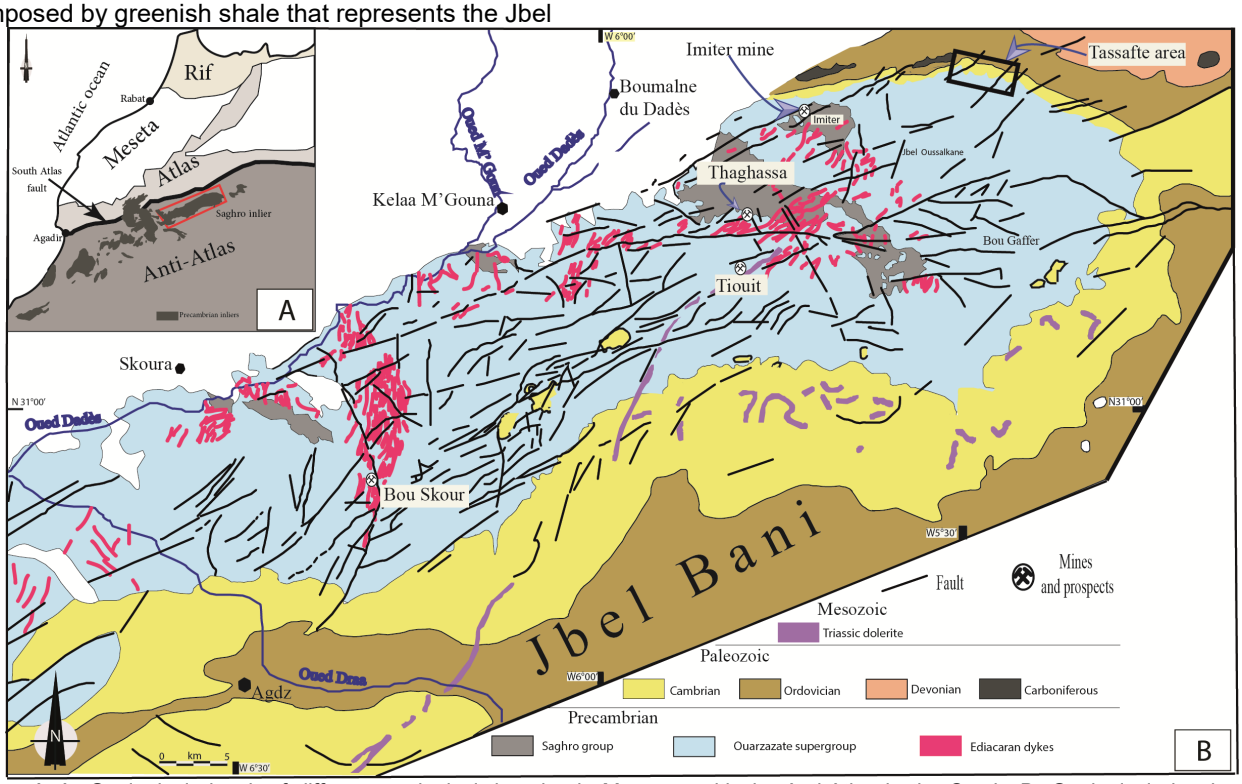

Figure 1. A- Geological sketch of different geological domains in Morocco, with the Anti-Atlas in the South. B- Geological sketch of the Saghro inlier with black box showing the location of the Tassafte mining area; updated after Tuduri (2005).

Wawrmast Formation showing interbedded lenses of carbonates and sandstone; the top is characterized by white massive quartzitic sandstones of Jbel Afrou Formation (Fig. 2).

2.2 Ore structures

In the Tassafte area, the ore deposits formed along an E-W shear system, in which the veins are oriented from N80 to N120. These ore structures are hosted in Ediacaran units and continuing within the Cambrian successions. The veins exhibit a thickness varying from some centimeter to decameter and they extend along 1 to 2 Km. They are generally dipping to the south about 55° to 90°, except the main major fault which marks the cartographic limit between the Ediacaran basement and the Cambrian cover and which is dipping to the North (85 to 70°N).

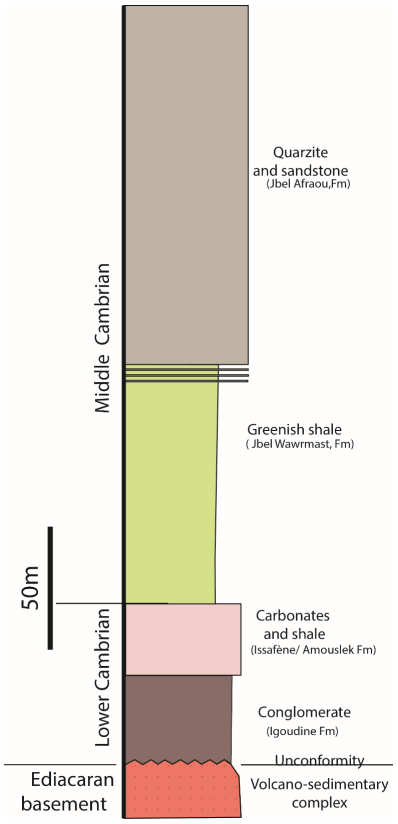

Figure 2. Schematic profile of the lithostratigraphic units that host the ore mineralization in the Tassafte area

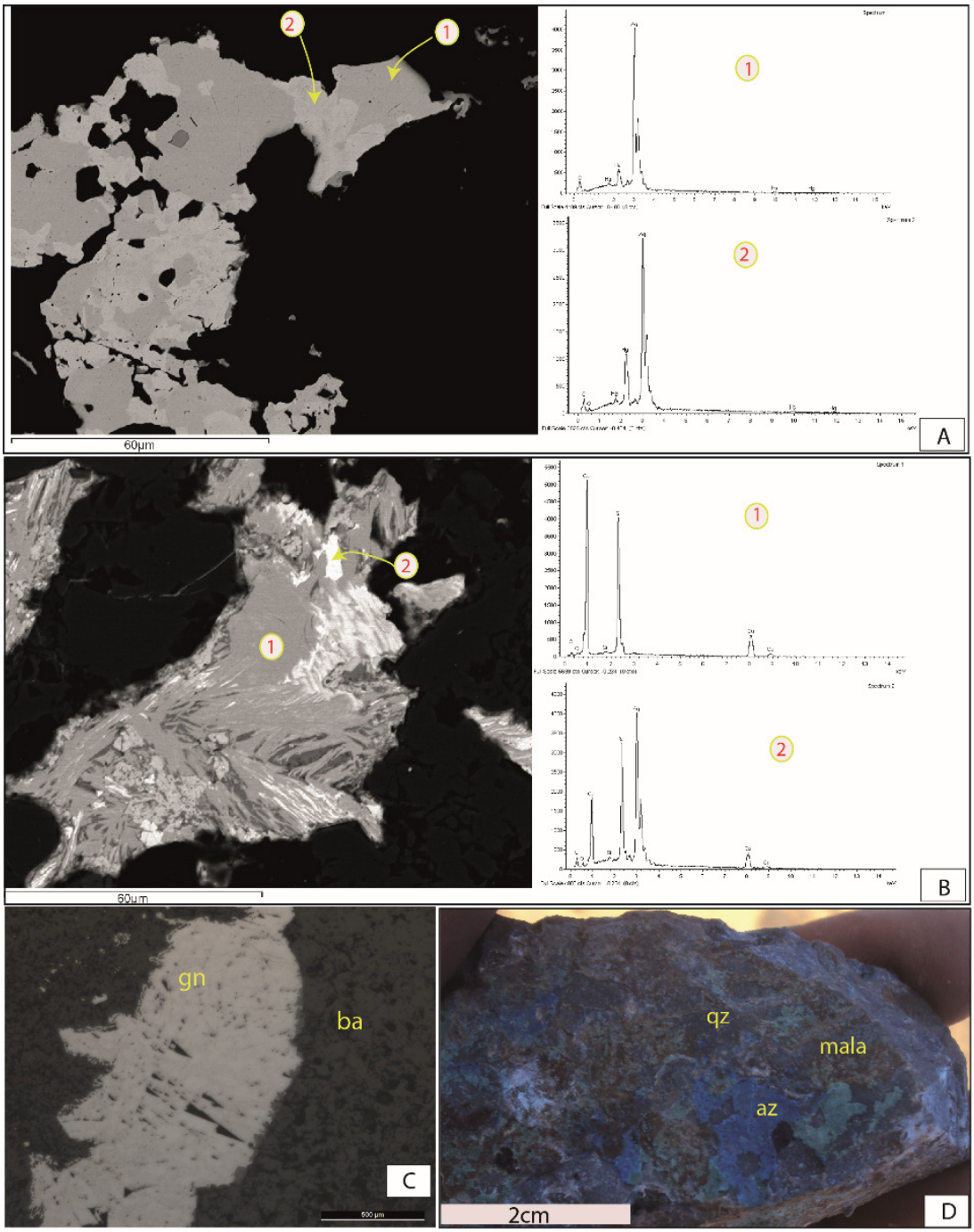

Figure 3. A- BSE image shows amalgam Ag-Hg mineral with different proportion of Ag and Hg that is confirmed byEDX analyses displayed on the right (Number 1 and 2 in circles). B- BSE image shows chalcopyrite and grey copper and their EDX analysis on the right. (Number 1 and 2 in circles). C- Thin section in reflected light image shows galena (gn) mineral within barite (ba) gangue. D- Malachite (mala) and azurite (az) mineralization within microcrystalline quartz gangue (qz).

2.3 Mineralization

Our preliminary results about the mineralization on the Tassafte mining area show a polymetallic mineralization within barite and quartz gangues. In the following, we present a brief description:

-Ag and Hg mineralization

The silver minerals are represented as argentopyrite, argentite, native silver and as an Ag-Hg amalgam (Fig. 3-A). The silver is also associated with grey copper.

-Cu mineralization

The copper minerals are largely present as copper sulfide (mainly chalcopyrite, chalcocite, covellite, bornite) or as a sulfosalt (grey copper) (Fig. 3-B, D). In addition, copper carbonate hydroxides are present as azurite and malachite.

-Zn mineralization

Is represented mainly by sphalerite or also within the

oxide stage in the form of zinc oxide.

-Pb mineralization

The Pb is present mainly as galena (Fig. 3-C).

-Gangue minerals

The gangue is represented by quartz that formed within several generations. They are microcrystalline quartz and geodic ones. Second gangue mineral is barite that show different texture such as massive and colloform.

Conclusions and prospective

The Tassafte mining area is located at the NE part of the Saghro inlier, about 20 km to the East of the Imiter mine. In this district the mineralization are formed in veins with centimetric to metric thickness. They are E-W-trending and they are hosted within Ediacaran and Cambrian successions. The mineralization is represented by copper minerals in the form of sulfide (chalcopyrite, chalcocite, covellite, bornite) or as carbonates hydroxide (malachite and azurite). In addition, the Ag mineralization forms an amalgam of Ag and Hg, or it is present as argentite and argentopyrite. This mineralization is also associated with galena and sphalerite.

Previous studies about the Ag-Hg-Cu mineralization specifically in the Imiter mine considered the mineralization to be restricted to the late Ediacaran age (Levresse 2001; Gasquet et al. 2005; Bouabdellah and Slack 2016). We present data indicating that at least part of the Ag-Hg-Cu-Pb-Zn mineralizations are younger and probably related to Variscan to Alpine orogenies.

Our prospective concerning the mineralization of the Tassafte area, consist of a deep study of the mineralization including fluid inclusions, isotopes, in order to understand the source and the genetic model of this mineralization. A comparison with Imiter mine and similar mining areas in the Anti-Atlas will be also carried out.

Acknowledgements

Many thanks to Ancemar Mining Company for their logistic support.

References

Borisenko AS, Lebedev VI, Borovikov AA, et al (2014) Forming conditions and age of native silver deposits in Anti-Atlas (Morocco). Dokl Earth Sci 456:663–666. doi: 10.1134/S1028334X1406021X

Bouabdellah M, Slack JF (2016) Mineral Deposits of North Africa. Springer

Bouchta R, Boyer F, Routhier P, et al (1977) l'aire cuprifere de l'Anti-Atlas (Maroc); permanence et aretes riches. Comptes Rendus l'Academie Sci Paris

Cheilletz A, Levresse G, Gasquet D, et al (2002) The giant Imiter silver deposit: Neoproterozoic epithermal mineralization in the Anti-Atlas, Morocco. Miner Depos 37:772–781. doi: 10.1007/s00126-002-0317-0

Essarraj S, Boiron MC, Cathelineau M, et al (2016) Basinal brines at the origin of the Imiter Ag-Hg deposit (Anti-Atlas, Morocco): Evidence from LA-ICP-MS data on fluid inclusions, halogen signatures, and stable isotopes (H, C, O). Econ Geol 111:1753–1781. doi: 10.2113/econgeo.111.7.1753

Gasquet D, Levresse G, Cheilletz A, et al (2005) Contribution to a geodynamic reconstruction of the Anti-Atlas (Morocco) during Pan-African times with the emphasis on inversion tectonics and metallogenic activity at the Precambrian-Cambrian transition. Precambrian Res 140:157–182. doi: 10.1016/j.precamres.2005.06.009

Levresse G (2001) Contribution à l'établissement d'un modèle génétique des gisements d'Imiter (Ag-Hg), Bou Madine (Pb-Zn-Cu-Ag-Au) et Bou Azzer (Co-Ni-As-Au-Ag) dans l'An ti-Atlas marocain

Mouttaqi A, Rjimati EC, Maacha L, et al (2011) LES PRINCIPALES MINES DU MAROC / Main Mines of Morocco

Tuduri J (2005) Processus de formation et relations spatio-temporelles des minéralisations à or et argent en contexte volcanique Précambrien (Jbel Saghro, Anti-Atlas, Maroc). Implications sur les relations déformation-magmatisme-volcanisme-hydrothermalisme. Université d'Orléans

Tuduri J, Chauvet A, Barbanson L, et al (2018) The Jbel Saghro Au(–Ag, Cu) and Ag–Hg Metallogenetic Province: Product of a Long-Lived Ediacaran Tectono-Magmatic Evolution in the Moroccan Anti-Atlas. Minerals 8:592. doi: 10.3390/min8120592

The Xiasai vein-type Ag–Pb–Zn deposit in the Yidun Terrane, SW China: source and timing of magmatism and mineralization

Yan–Jun Li, Jun–Hao Wei, Jun Tan, Le–Bing Fu, Huan Li
School of Earth Resources, China University of Geosciences, China

Abstract. The Xiasai-Lianlong metallogenic belt in the central Yidun Terrane hosts numerous Sn–Ag and (Sn–) Ag–Pb–Zn deposits, which are spatially associated with Cretaceous granites. The Xiasai Ag–Pb–Zn deposit (0.27 Mt Pb+Zn, 1028 t Ag, and 20000 t Sn), is the largest deposit in the belt and is related to a monzogranite intrusion. The deposit consists of (quartz-) sulfides in veins, resulting from three successive mineralization stages (I-III). Rb–Sr isochron dating of sphalerite samples yielded an age of 99 ± 3 Ma and zircon U–Pb LA–ICP–MS dating of the monzogranite gave ages between 102 ± 1 and 101 ± 1 Ma. The $\delta^{34}S$ values of eleven sphalerite separates range from −9.7 to –3.1‰ and those from nineteen galena samples from –10.5 to –4.9‰. The estimated $\delta^{34}S$ value of the ore-forming fluid is –8.5‰, using the sulfur isotopic fractionation of sphalerite-galena pairs that are assumed to be in equilibrium. Eighteen sulfides from sub-stages II-2 and II-3 have relatively homogeneous Pb isotopic compositions, which are similar with the ones of K-feldspars from the Xiasai monzogranite. Geochronological and isotope data support a magmatic-hydrothermal origin for the Xiasai Ag–Pb–Zn deposit.

1 Introduction

Ag–Pb–Zn vein-type deposits are one of the most important types of Ag and/or Pb–Zn mineralization, and many of them have been regarded as the distal part of the magmatic-hydrothermal systems with proximal porphyry and/or skarn Cu–Mo mineralization (e.g., Sillitoe 2010; Lawley et al. 2010; Bonsall et al. 2011; Li et al. 2017; Liu et al. 2016; Zhai et al. 2019). Ore-related granitoids are dominated by granodiorites, granites, monzogranites, and granite porphyries, which generally have geochemical affinities of I- and S-type, or even A-type granites (Li et al. 2012, 2017; Liu et al. 2016; Jiang et al. 2018).

The 0.27Mt Xiasai Ag–Pb–Zn deposit in the central Yidun Terrane (YDT), SW China, is a new example for hydrothermal vein-type mineralization. It was regarded as a vein-type deposit associated with a Cretaceous A-type granite (Qu et al. 2002; Hou et al. 2007). This study presents S–Pb isotope geochemistry, sphalerite Rb–Sr, and zircon LA–ICP–MS U–Pb geochronology for the Xiasai Ag–Pb–Zn deposit and associated monzogranite to further constrain source and timing of magmatism and mineralization.

2 Geology of ore deposit

The YDT lies between the Qiangtang and the Songpan–Garze terranes and is separated by two oceanic suture zones, i.e., the Jinshajiang suture to the west, and the Garze–Litang suture to the north and east (Wang et al. 2013). Three types of ore deposits belts have been recognized in the YDT: volcanogenic massive sulfides (VMS), porphyry–skarn Cu–Mo, and Sn–Ag polymetallic belts (Hou et al. 2007). The Sn–Ag belt (Xiasai–Lianlong metallogenic belt) is located in the central YDT, and is composed of four large deposits, two medium-sized deposits and numerous smaller Ag polymetallic deposits.

The Xiasai Ag–Pb–Zn deposit (0.27 Mt Pb+Zn, 1028 t Ag, and 20000 t Sn) is controlled by NNW-trending faults and is located in the northern part of the Xiasai monzogranite (XSM) (Fig. 1). The XSM has a weakly peraluminous A-type granite composition, with high SiO2, alkalis, and FeOt contents, and low CaO, MgO, and TiO2 contents. The host-rocks consist of grey slates, sandstones, intermediate to felsic volcanic rocks, and tuffs, belonging to the upper part of the Triassic Tumugou Formation.

Two types of mineralization, i.e., Sn-bearing veins and Ag–Pb–Zn-bearing veins occur in the Xiasai deposit. The Sn mineralization consists of cassiterite-quartz veins in a proximal location within 800m of the XSM. The Ag–Pb–Zn mineralization is hosted in (quartz-) sulfides veins that are located distal and to the north of the XSM with distance of ~500–3500 m (Fig. 1). Nine Ag–Pb–Zn ore bodies have been recognized and they commonly occur as lodes, lenses, and disconnected pods. The Ag–Pb–Zn mineralized veins exhibit horizontal and vertical zonation in the mineral assemblages. It can be divided into three zones from south to north, i.e., a Sn rich zone, a Zn–Cu-rich zone, and a Pb–Ag-rich zone (Fig. 1). A horizontal and vertical alteration zonation is developed. Three alteration zones are recognized from south to north, i.e., epidote+actinolite+garnet zone, quartz+sericite+chlorite zone, and weak quartz+sericite zone. Three hydrothermal stages are recognized in the Xiasai deposit, i.e., stage I (quartz-cassiterite veins), stage II (Cu– Zn–Pb–Ag), and stage III (quartz+calcite veins). In addition, the stage II can be further divided into three sub-stages, i.e., sub-stage II-1 (Apy+Po), sub-stage II-2 (Ccp+Sp), and sub-stage II-3 (Gn+Ag-bearing minerals).

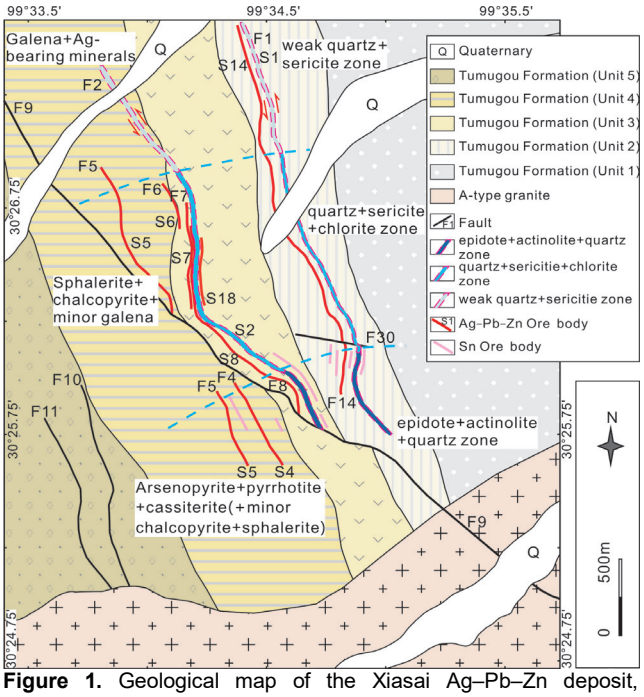

Figure 1. Geological map of the Xiasai Ag–Pb–Zn deposit, showing the location and distribution of the ore bodies and the relationship between mineralization, alteration zonation, the XSM, and NNW-trending faults.

3 Geochronology and isotope geochemistry

3.1 Ages for mineralization and ore-related monzogranite

Rb–Sr isotopic dating were performed using a Thermo TRITON thermal-ionization mass spectrometer (TIMS) at the Wuhan Isotope Laboratory, Chinese Academy of Geological Sciences. More details about the method and procedure can be found in Duan et al. (2014) and Yang et al. (2015). Eight sphalerite samples have Rb contents of 0.022–2.215 ppm and Sr contents of 0.173–7.143 ppm. Their $^{87}Rb/^{86}Sr$ ratios vary from 0.029 to 6.303 and $^{87}Sr/^{86}Sr$ values from 0.71051 to 0.73367. The data of seven samples constitute a good linear array on $^{87}Sr/^{86}Sr$ vs. $^{87}Rb/^{86}Sr$ correlation diagram with Rb–Sr isochron age of 99 ± 10 Ma (R^2 = 0.992). The $^{87}Rb/^{86}Sr$ ratios for the ZnS phase of samples K18-1S and 4755-1S are 26.51 and 19.09, and $^{87}Sr/^{86}Sr$ values are 0.76130 and 0.75226. Nine samples, including seven sphalerite phases and two ZnS phases, also constitute a good linear array on $^{87}Sr/^{86}Sr$ vs. $^{87}Rb/^{86}Sr$ correlation diagram with an age of 99 ± 3 Ma (Fig. 2). This data is interpreted to represent the age of the Cu–Zn mineralization in the Xiasai Ag–Pb–Zn deposit.

Two samples (XS–5 and XS–1) from the XSM were selected for LA–ICP–MS U–Pb dating of zircon at the State Key Laboratory of Geological Processes and Mineral Resources, China University of Geosciences in Wuhan. Eighteen analyses have been carried out on the sample XS–5. Most data plot (n = 14) on or near the concordia curve, and some (n = 4) are shifted to the right side of the concordia curve (Fig. 3), which is probably generated by the analytical uncertainty of ^{207}Pb

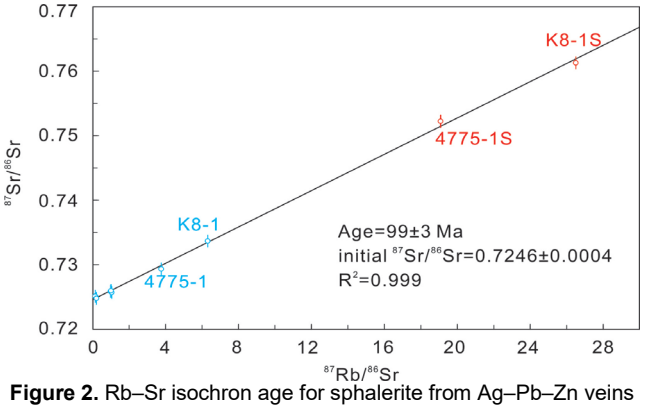

Figure 2. Rb–Sr isochron age for sphalerite from Ag–Pb–Zn veins

measurements and traces of common lead. The $^{206}Pb/^{238}U$ ages of eighteen spot analyses range from 96 ± 3 to 109 ± 4 Ma, and yield an average $^{206}Pb/^{238}U$ age of 102 ± 1 Ma (MSWD = 0.9). Nineteen analyses have been conducted on the sample XS–1. The $^{206}Pb/^{238}U$ ages of fourteen analyses range from 95 ± 3 to 106 ± 3 Ma. These data yield an average $^{206}Pb/^{238}U$ age of 101 ± 1 Ma (MSWD = 1.4) (Fig. 3).

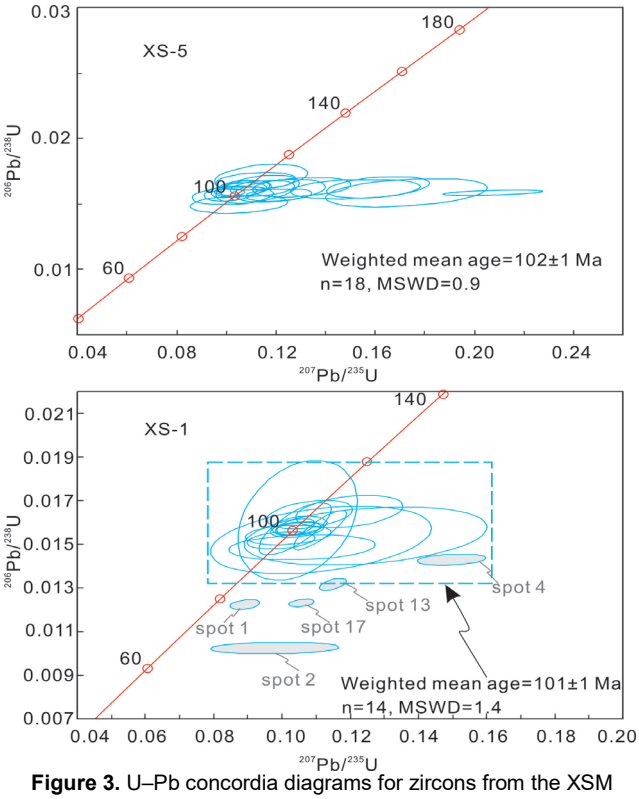

Figure 3. U–Pb concordia diagrams for zircons from the XSM

3.2 Sulfur and lead isotopic compositions

The $\delta^{34}S$ values of five sphalerite separates range from −7.6 to –3.1‰ with an average of –6.0‰, and those for five galena samples range from –10.1 to –6.7‰ (mean = –8.2‰) (Fig. 4). The measured $\delta^{34}S$ values of sphalerite and galena are similar to those from six sphalerite (–9.7 to –5.5‰) and fourteen galena (–10.5 to –4.9‰) samples found in previous studies (Liu 2003; Ying et al. 2006; Zou et al. 2008). Meanwhile, $\delta^{34}S$ values of six

pyrite and four pyrrhotite separates are comprised between –6.4 and –1.2‰, and –7.1 and –6.5‰, respectively. Pyrite has higher $\delta^{34}S$ relative to sphalerite and galena. Combined with literature values, the $\delta^{34}S$ values of 41 sulfides from the Xiasai deposit range from –10.5 to –1.2‰, with an arithmetic mean of –7.0 ± 3.5‰.

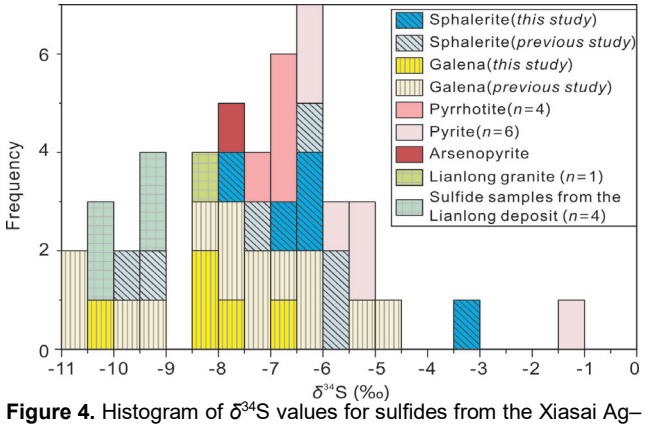

Figure 4. Histogram of $\delta^{34}S$ values for sulfides from the Xiasai Ag–Pb–Zn deposit

Five galena samples have Pb isotopic ratios of $^{206}Pb/^{204}Pb$ = 18.711 –18.748 (average = 18.727), $^{207}Pb/^{204}Pb$ = 15.711–15.752 (average = 15.730), and $^{208}Pb/^{204}Pb$ = 39.104–39.225 (average = 39.158). In addition, thirteen other sulfides including ten galena, two sphalerite, and one pyrrhotite samples have $^{206}Pb/^{204}Pb$ = 18.687–18.920 (average = 18.767), $^{207}Pb/^{204}Pb$ = 15.675–15.956 (average = 15.770), and $^{208}Pb/^{204}Pb$ = 38.979–39.851 (average = 39.331) (Ying et al. 2006; Zou et al. 2008). The lead isotopic compositions of galena samples analyzed in this study and previous sulfides ($^{206}Pb/^{204}Pb$ = 18.711–18.748, $^{207}Pb/^{204}Pb$ = 15.711–15.752, and $^{208}Pb/^{204}Pb$ = 39.104–39.225) are similar to those at the Lianlong skarn Ag–Sn deposit, which has $^{206}Pb/^{204}Pb$, $^{207}Pb/^{204}Pb$, and $^{208}Pb/^{204}Pb$ ratios of 18.618–18.710, 15.630–15.738, and 38.199–39.176, respectively (Fig. 5; Qu et al. 2001).

Five K-feldspar separates from the XSM have $^{206}Pb/^{204}Pb$, $^{207}Pb/^{204}Pb$, and $^{208}Pb/^{204}Pb$ of 18.702–18.731, 15.680–15.718, and 39.000–39.128, respectively, and are distinctly lower than those of the whole-rock samples from the RYC granite (Fig. 5). Compared with the two types of samples from granites, the ore sulfides from the Ag–Pb–Zn deposit tend to have similar lead isotopic compositions to K-feldspar from the XSM.

4 Discussions

4.1 Albian-Cenomanian magmatism and Ag–Pb–Zn mineralization

Cretaceous granites in the central YDT have been dated at 93–60 Ma by Ar–Ar on biotites and K-feldspars separates, as well as whole-rock Rb–Sr isochron (Qu et al. 2002; Ying et al. 2006). The U–Pb ages for the XSM are between 102 ± 1 and 101 ± 1Ma, which are coeval

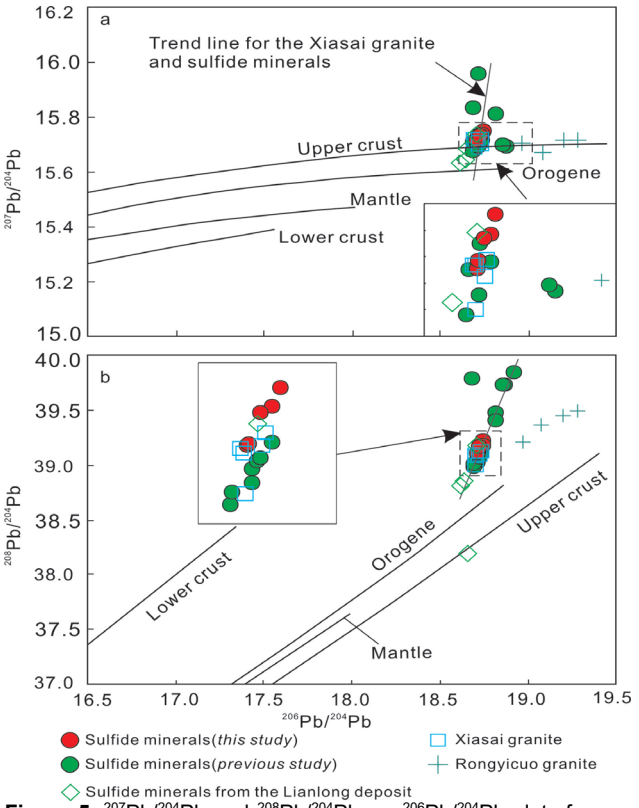

Figure 5. $^{207}Pb/^{204}Pb$ and $^{208}Pb/^{204}Pb$ vs. $^{206}Pb/^{204}Pb$ plots for ores and monzogranite from the Xiasai Ag–Pb–Zn deposit

with the ages of the Genie biotite monzogranite (LA–ICP–MS U–Pb age on zircons of 105 ± 2 Ma, Wang et al. 2008) and the Chuershan granite (LA–ICP–MS U–Pb age on zircons of 104 ± 1 Ma, Reid et al. 2007) in the YDT. Therefore, it is suggested that the crystallization age of the granites is between 105 to 101 Ma. The younger Ar–Ar and Rb–Sr ages obtained likely reflect post-crystallization episodes related to hydrothermal alterations. The Rb–Sr dating method for different phases of sphalerite was applied to obtain constraints on the age of the Pb–Zn mineralization (Duan et al. 2014; Yang et al. 2015). The Rb–Sr isochron age of 99 ± 3 Ma obtained for sphalerite from sub-stage II-2 is interpreted as the age of Ag–Pb–Zn mineralization. The age for sphalerite is identical within uncertainty to zircon U–Pb age of the XSM in the Xiasai district, thus indicating that the mineralization and the granitic magmatism are coeval.

4.2 Source of ore-forming materials

41 sulfides from the Xiasai deposit have $\delta^{34}S$ values ranging from –10.5 to –1.2‰ (arithmetic mean = –7.0 ± 3.5‰) with an overall disequilibrium of sulfur isotopes among sulfides during the evolution of the deposit. The sulfur isotopic compositions for the Xiasai deposit are slightly higher than the ones of sulfides from the adjacent Lianlong skarn-type Sn–Ag deposit in central YDT (–10.5 to –9.5‰, Qu et al. 2001). The $\delta^{34}S$ value of the estimated ore-forming fluid for the Xiasai deposit is –8.5‰, using the sulfur isotopic fractionation of sphalerite-galena pairs that are assumed to be in

equilibrium. It is similar to the $\delta^{34}S$ value of one whole-rock sample from the Lianlong granite which was associated to skarn-type Sn–Ag mineralization (–8.1‰; Qu et al. 2001). The result indicates that the sulfur may be derived from the XSM. In addition, Wang et al. (2015) proposed that the low $\delta^{34}S$ values for hydrothermal Ag–Pb–Zn veins and skarn type Sn–Ag deposits in the central YDT were interpreted as magmatic in origin resulting from partial crustal melting of A-type granites.

The Pb isotopic compositions for ores from the Xiasai Ag–Pb–Zn deposit are identical to those of K-feldspar from the XSM. This probably indicates a common source of Pb and a possible genetic relationship between the XSM and Ag–Pb–Zn mineralization. The controversy regarding the discrimination diagrams for Pb isotopes indicates complex Pb sources for sulfides and granitic intrusions (Wang et al. 2015). Ores and K-feldspar from the XSM in the Xiasai deposit share the same linear relationship in the $^{207}Pb/^{204}Pb$ and $^{208}Pb/^{204}Pb$ vs. $^{206}Pb/^{204}Pb$ diagrams (Fig. 5), which could suggest a two-component mixing model involving crust and mantle components. This conclusion can be corroborated by Lu–Hf isotope on zircons from the XSM ($\varepsilon_{Hf}(t)$ = –2.7 to 0.6 and T_{DM2} = 925–1095 Ma).

5 Conclusions

Zircon U–Pb dating of the XSM and the Rb–Sr isochron age for sphalerite confirms that the granitic magmatism and the formation of hydrothermal Ag–Pb–Zn mineralization were coeval during the Lower to Upper Cretaceous (Albian–Cenomanian). The S isotopic composition is similar to the $\delta^{34}S$ value of the LL granite, indicating that the sulfur may be derived from the Albian granitic intrusions. The Pb isotopic composition of sulfides from the Ag–Pb–Zn mineralization is consistent with the ones of K-feldspar from the monzogranite, suggesting a common origin.

Acknowledgements

This study was co-supported by the Natural Science Foundation of China (grant 41672083), the Fundamental Research Founds for National Universities, China University of Geosciences (Wuhan) (grants CUGCJ1817 and CUGQYZX1708), and the Chinese Scholarship Council (support for Yan–Jun Li during his stay at Aarhus University, Denmark).

References

Bonsall TA, Spry PG, Voudouris PC, Tombros S, Seymour KS, Melfos V (2011) The geochemistry of carbonate-replacement Pb–Zn–Ag mineralization in the Lavrion district, Attica, Greece: Fluid inclusion, stable isotope, and rare earth element studies. Econ Geol 106:619–651

Duan QF, Cao L, Zeng JK, Zhou Y, Tang ZY, Li K (2014) Rb–Sr dating of sphalerites from Shizishan Pb–Zn deposit in Huayuan ore concentration area, western Hunan, and its geological significance. Earth Sci–J China Univ Geos 39:977–986 (in Chinese with English abstract)

Hou ZQ, Zaw K, Pan GT, Mo XX, Xu Q, Hu YZ, Li XZ (2007) Sanjiang Tethyan metallogenesis in S.W. China: Tectonic setting, metallogenic epochs and deposit types. Ore Geol Rev 31:48–87

Jiang WH, Li H, Wu JH, Zhou ZK, Kong H, Cao JY (2018) A newly found biotite syenogranite in the Huangshaping polymetallic deposit, South China: insights into Cu mineralization. J Earth Sci 29:537–555

Lawley C, Richards JP, Anderson RG, Creaser RA, Heaman LM (2010) Geochronology and geochemistry of the MAX porphyry Mo deposit and its relationship to Pb–Zn–Ag mineralization, Kootenay arc, southeastern British Columbia, Canada. Econ Geol 105:1113–1142

Li YJ, Wei JH, Chen HY, Tan J, Fu LB, Wu G (2012) Origin of the Maoduan Pb–Zn–Mo deposit, eastern Cathaysia Block, China: geological, geochronological, geochemical, and Sr–Nd–Pb–S isotopic constraints. Mineral Deposita 47:763–780

Li ZK, Bi SJ, Li JW, Zhang W, Cooke DR, Selby D (2017) Distal Pb–Zn–Ag veins associated with the world-class Donggou porphyry Mo deposit, southern North China craton. Ore Geol Rev 82:232–251

Liu Q (2003) Geological characteristics and genesis of Xiasai silver-polymetallic deposit in western Sichuan Province. Mineral Deposits 22:121–127 (in Chinese with English abstract)

Liu YF, Jiang SH, Bagas L (2016) The genesis of metal zonation in the Weilasituo and Bairendaba Ag–Zn–Pb–Cu–(Sn–W) deposits in the shallow part of a porphyry Sn–W–Rb system, Inner Mongolia, China. Ore Geol Rev 75: 150–173

Qu XM, Hou ZQ, Zhou SG (2001) Metallogenic geological characteristics of the Lianlong skarn-type Sn–Ag polymetallic deposit in western Sichuan. Acta Geos Sin 23:223–228 (in Chinese with English abstract)

Qu XM, Hou ZQ, Zhou SG (2002) Geochemical and Nd, Sr Isotopic study of the post– orogenic granites in the Yidun Arc Belt of Northern Sanjiang Region, Southwestern China. Resour Geol 52:163–172

Reid A, Wilson CJL, Shun L, Pearson N, Belousova E (2007) Mesozoic plutons of the Yidun Arc, SW China: U–Pb geochronology and Hf isotopic signature. Ore Geol Rev 31:88–106

Sillitoe RH (2010) Porphyry copper systems. Econ Geol 105: 3–41

Wang BQ, Wang W, Chen WT, Gao JF, Zhao XF, Yan DP, Zhou MF (2013b) Constraints of detrital zircon U–Pb ages and Hf isotopes on the provenance of the Triassic Yidun Group and tectonic evolution of the Yidun Terrane, Eastern Tibet. Sediment Geol 289:74–98

Wang QW, Wang KM, Kan ZZ, Fu XF (2008a) Granites and associated minerogenetic series of ore deposits in western Sichuan Province. Geological Publishing House, Beijing p 1–305 (in Chinese)

Wang XS, Bi XW, Hu RZ, Leng CB, Yu HJ, Yin GH. (2015) S-Pb isotopic geochemistry of Xiuwacu magmatic hydrothermal Mo-W deposit in Zhongdian area, NW Yunnan: Constrains on the sources of metal. Acta Petrol Sin 31:3171–3188 (in Chinese with English abstract)

Yang HM, Liu CP, Duan RC, Gu XM, Lu SS, Tan JJ, Cai YX, Zhang LG, Qiu XF (2015) Rb–Sr and Sm–Nd isochron ages of Bokouchang Pb–Zn deposit in Tongren, Guizhou Province and their geological implication. Geotecton et Metallog 39:855–865 (in Chinese with English abstract)

Ying HL, Wang DH, Fu XF (2006) Timing and lead and sulfur isotope composition of Xiasai granite and silver polymetallic deposit in Batang, Sichuan Province. Mineral deposits 25:135–146 (in Chinese with English abstract)

Zhai DG, Liu JJ, Cook NJ, Wang XL, Yang YQ, Zhang AL, Jiao YC (2019) Mineralogical, textural, sulfur and lead isotope constraints on the origin of Ag–Pb–Zn mineralization at Bianjiadayuan, Inner Mongolia, NE China. Mineral Deposita 54:47–66

Zou GF, Zheng RC, Hu SH, Chen CJ, Jiang HC, Wu HB (2008) Geological features of the Xiasai silver-polymetallic deposit in West Sichuan, China. J Chengdu Univ Tech (Sci & Tech Edition) 35:93–102 (in Chinese with English abstract)

Hydrothermal native element-arsenide (five-element) mineralizations

Manuel Scharrer, Stefan Kreissl, Gregor Markl
Eberhard Karls Universität Tübingen, Tübingen, Germany

Abstract. The hydrothermal native element-arsenide mineralization (five-element) type comprises native Ag and/or native Bi as well as Ni-, Co-, and Fe-arsenides and –sulfarsenides. Due to the current surge in Co-demand, this mineralization type has regained recent economic interest. Thus, it is of interest to further understand the paragenetic and possible spatial relation of Co-bearing minerals and the formation mechanism/process of this mineralization type. This is achieved through an extensive literature review in combination with newly calculated stability relations.

The mineralization is host rock independent, but spatially linked to sources of reducing agents (as this is the cause of precipitation). This reduction process results in a thermodynamically controlled characteristic Ni- → Co- → Fe-diarsenides sequence, as well as a transition from native elements to mono- to di-arsenides. The temporal Ni → Co → Fe trend has also been described to occur on a special scale, and since it is ubiquitous, it may be used as a tool in constraining Co rich sections of a deposit. The formation of this mineralization is, however, not only thermodynamically, but also kinetically controlled, as is evident by the abundant dendritic textures. Kinetics favor a sulfate-sulfide disequilibrium which enables an aqueous sulfide poor system that allows for arsenide formation.

1 The mineralization

Hydrothermal ore deposits that are dominated by Ni-Co-arsenides ± native elements have been labeled "five-element vein type", "five element association", "nickel-cobalt-native silver ore type", “Bi-Co-Ni-As-U-Ag-Formation”, and "Ag-Co-Ni-As-Bi type" (e.g., Bastin 1939, Baumann et al. 2000, Kissin 1992, Kissin et al. 1988, Markl et al. 2016, Müller 1860). We propose that this mineralization type should better be termed “Ni-Co-Fe-arsenide type” or “native element-arsenide mineralization”, as it always contains hydrothermal Ni-, Co-, and Fe-arsenides and/or sulfarsenides together with variable quantities of native elements (silver, bismuth, arsenic, antimony), metal alloys and in rare cases gold, uraninite, antimonides and Cu arsenides (e.g. Bagheri et al. 2007; Hiller and Schuppan 2008; Staude et al. 2007).

The hydrothermal native element-arsenide mineralization has been subject to centuries of exploration and mining. Although economic interest has decreased over time, the ever-increasing recent demand for Co due to in large part the renewable energy industry, this mineralization type has sparked new economic interest. Furthermore, the arsenides are commonly associated with other economically interesting elemental enrichments (such as Ag, Cu, Au; e.g., Bouabdellah et al. 2016, Bagheri et al. 2007) Their current economic importance is evident for example the Bou Azzer mine (Slack et al. 2017) and the recent exploration in Slovakia (Dobšiná and Kolba deposits) by European Cobalt Ltd (Kumova 2017).

The following description (Fig. 1) of the mineralization is compiled, evaluated and generalized by Scharrer et al (in review) from publications on a large number of localities worldwide. These among others include: Anārak, Iran (e.g., Bagheri et al. 2007); Belorechenskoe deposit, Russia (Pekov et al. 2010); Black Hawk district, USA (e.g., Gillerman and Whitebread 1953); Bou Azzer, Morocco (e.g. Bouabdellah et al. 2016); Cobalt-Gowganda, Canada (Bastin 1949; Petruk 1968; Petruk 1971; Marshall and Watkinson 2000); Dobšiná, Slovakia (Kiefer et al. 2017); Great Bear lake, Canada (e.g., Robinson and Ohmoto 1973); Kongsberg, Norway (Kotková et al. 2017); Odenwald, Germany (Heimig 2015; Burisch et al. 2017); Ore mountains Germany and Czech Republic (e.g., Hofmann 1986; Baumann et al. 2000; Lipp and Flach 2003; Hiller and Schuppan 2008); Pyrenees, Spain (e.g., Fanlo et al. 2006); Schladming, Switzerland (Paar and Chen 1979); Schwarzwald, Germany (Staude et al. 2007; Staude et al. 2012); Spessart, Germany (Wagner and Lorenz 2002) ; Valais, Switzerland (Kreissl et al. 2018); Zálesí, Czech Republic (Dolníček et al. 2009)

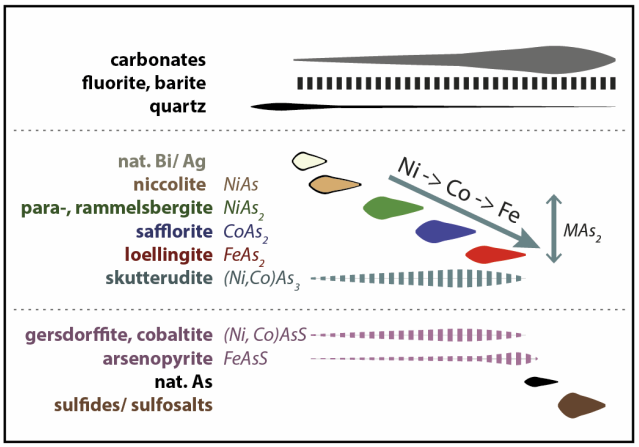

Figure 1. Simplified Paragenetic sequence of the arsenide and sulfide stage.

The native element-arsenide assemblage (arsenide stage) forms an intermediate stage within a polystage, polymetallic mineralization sequence. The typical dendritic growth of the initial minerals native silver,

native bismuth and niccolite (Ni-monoarsenide), which act as crystallization nuclei to subsequent minerals, define the overall characteristic rosette type texture of the ores. Niccolite typically forms subsequent to the native elements and is in turn overgrown by the generalized consecutive sequence of Ni-, Co-, and Fe-diarsenides (Fig. 1). This mineral sequence has also been reported to be spatially resolvable (Petruk 1968).

Several generations of tri- and sulfarsenides are common and crystallize at random intervals and in variable abundance, but are generally more common towards the end of the arsenide stage (Fig. 1). The Ni→Co→Fe sequence is at times also visible for the tri- and sulfarsenides, but the data on this in the literature is scarce. The arsenide minerals and native elements commonly occur in a gangue of carbonates (typically calcite, dolomite, ankerite or more rarely siderite; Markl et al. 2016), where fluorite, barite, and quartz may be present, but are generally much rarer (Bastin 1939).

There is a gradual transition from the arsenide stage to the subsequent sulfosalt-bearing and base-metal sulfide- mineralization stages. Typical minerals of this stage are Ag-, Sb-, As-bearing sulfosalts together with native arsenic, and base-metal sulfides. These are present in the form of overgrowth and/or replacement textures producing a complex and locally variable mineral succession.

This generalized mineralogical succession is very similar (independent of localities), and only the absolute abundance between minerals varies. It should, however, be noted that this mineral sequence is only generalized and may not always be visible in individual samples.

2 Genesis

2.1 Precipitation mechanism

The formation temperature (fluid inclusion data) of the arsenide stage varies greatly between localities (50-400 °C) and no systematic cooling has been observed (e.g. Bouabdellah et al. 2016, Markl et al. 2016; and references therein), which indicates a principally temperature-independent formation mechanism. The fluids are highly saline (up to 50 wt% NaCl eq. containing dominantly NaCl and $CaCl_2$ (e.g., Bouabdellah et al. 2016, Markl et al. 2016). The fluid source has been strongly debated, between and for individual locatlities (e.g., Bou Azzer: Bouabdellah et al. 2016; e.g., Cobalt-Gowganda: Petruk 1968, Echo-Bay: Robinson and Ohmoto 1973) and there seem to be several fluid sources. Thus, the source is irrelevant for the formation of this mineralization, as long as the fluid carries the necessary metals.

The conspicuously similar mineralization sequence implies common formation conditions/mechanisms for this mineralization type, independent of location. However, several different formation mechanisms have been proposed in the past (Burisch et al. 2017; Kissin 1993; Kreissl et al. 2018; Markl et al. 2016; Ondrus et al. 2003a; Robinson and Ohmoto 1973). Most of these differ to some degree, but involve some sort of redox change. The abundant minerals, native bismuth, native silver, arsenides and native arsenic are only stable under reduced conditions, whereas their constituent elements are soluble under more oxidized conditions, Markl et al. (2016) and Burisch et al. (2017) related the formation of native element-arsenide assemblages to a process of strong and rapid reduction. Furthermore, hydrocarbons have been identified in fluid inclusions, also indicating very reduced conditions (e.g., Odenwald: Burisch et al. 2017; Cobalt-Gowganda: Kerrich et al. 1986; Bou Azzer: Essarraj et al. 2016 and Imiter: Levresse et al. 2016). Lastly, a close spatial association of ores and reducing agents such as siderite, sulfide, and/or graphite-rich host rocks and organic-rich shales has been described for several localities (e.g., Cheilletz et al. 2002; Kissin 1993 and references therein, Kreissl 2018; Lipp and Flach 2003). From an exploration point of view, this signifies that the hydrothermal native element-arsenide mineralization is spatially independent of the host rock or specific fluid source, but is constrained to the presence of various reducing agents.

3 Methodology

Thermodynamic modeling was done using the Thermoddem database of 2017 (Blanc et al. 2012) with internally consistent additions and the Phase 2 application of the Geochemist's Workbench 12 ® (Bethke 2007). For thermodynamic modeling procedures, thermodynamic data selection and estimation, as well as fluid composition compilation and constraints see Scharrer et al. (in review).

4 Genetic model

4.1 Mineral sequence

According to thermodynamic predictions, the initial minerals that precipitate during fluid reduction are native silver and native bismuth (Fig. 2). This is in perfect agreement with petrographic descriptions (see above). The subsequent formation of Ni-monoarsenide and then Ni-, Co- and Fe diarsenide (that is present in nearly all localities) is also in accordance with thermodynamic predictions at mildly basic to acidic conditions (Fig. 2). Ni-monoarsenide only forms at neutral to basic pH, which enables the formation of Ni-diarsenide without abundant initial Ni-monoarsenide. The arsenide sequence (Ni→Co→Fe) is determined not only by the decreasing stability of the minerals, but also by the increasing thermodynamic stability of the aqueous Cl- and O-complexes from Ni to Co and followed by Fe. Thus, during reduction, the fluid is successively depleted in elements (e.g., Bouabdellah et al. 2016) due to this precipitation sequence. This sequence, but not the absolute abundance of the arsenides, is largely independent of Ni, Co and Fe concentration in the fluid, as it would require a three order of magnitude difference in concentration to change. A nearly complete miscibility is present between the diarsenides in natural samples (not considered in the thermodynamic calculations).

Thus, such a large difference in concentration would result in some minerals not forming.

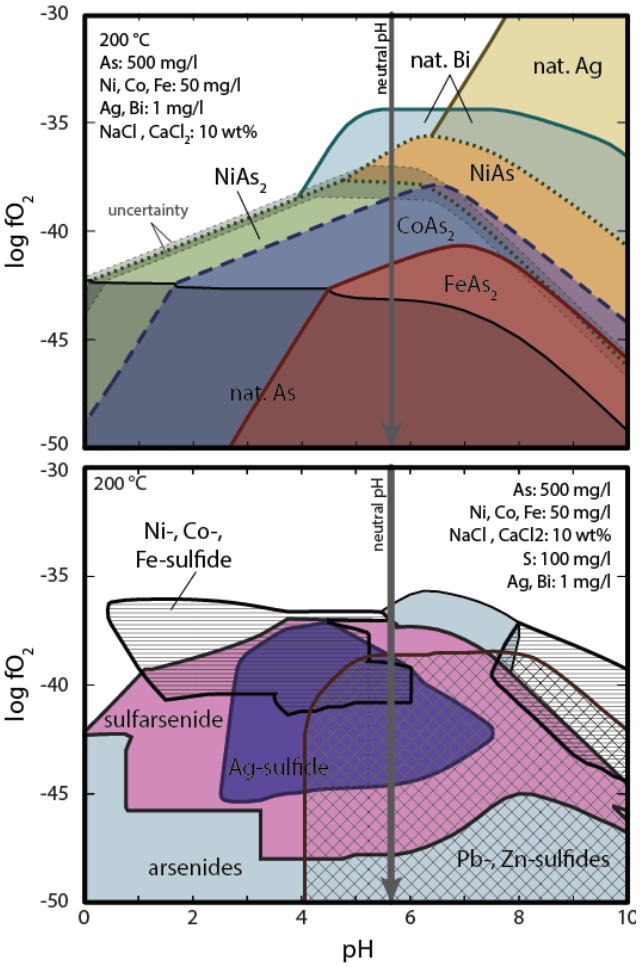

Figure 2. Thermodynamic model of the Ni-Co-Fe-As (top) and Ni-Co-Fe-Pb-Zn-As-S system (bottom) modified from Scharrer et al (in review).

4.2 Sulfide enigma

Concerning liberations and extraction during processing, it can be vital to understand the mineralogy and their textural occurrence. Although normally, arsenides dominate, some occurrences present a predominance of sulfarsenides over arsenides (e.g., Dobšiná: Kiefer et al. 2017; Kongsberg: Kotková et al. 2017; Valais: Kreissl et al. 2018). Thus, at these locations the Co/As ratio of the ore is expected to be significantly larger, since the undesired arsenic is replaced by sulfur.

Sulfarsenides become thermodynamically stable even at low sulfide concentrations (<<10 mg/kg S) until the present aqueous sulfide has been precipitated as sulfarsenides. At these conditions, they form co-genetically with the arsenides which is featured in natural samples as sulfarsenide or sulfide-rich arsenide bands within arsenide rosettes. Thus, it is likely that these textures represent a local and short-lived increase of the sulfide activity in an otherwise sulfide-deficient solution.

If, however, more sulfide is present, the sulfarsenides become predominant over the arsenides and no arsenides would form (Fig. 2). The only exception is the Ni-monoarsenide that is stable at higher oxidation states than the Ni-sulfarsenide. Furthermore, Ni-, Co-, and Fe-sulfides as well as base metal sulfides and sulfosalts become stable. These minerals are however, all absent in the arsenide stage and only, in part, become relevant in the subsequent sulfide stage. Thus, the sulfide content of the mineralizing fluid has to be low in order to form the arsenide- and native element- dominated mineralization at hand. For sulfide to be scarce, either sulfur has to be limited or a disequilibrium between sulfate and sulfide is present during reduction. Although both scenarios can occur in nature, the thermodynamic disequilibrium is certainly an important factor since sulfate-sulfide kinetics are very sluggish at low temperatures (<200 °C; Ohmoto and Lasaga 1982) and some localities show cogenetic sulfate in the form of barite together with arsenide (Lipp and Flach 2003; Staude et al. 2012). The importance of kinetics and the fast precipitation process is indicated by the dendritic textures of the initial ore minerals (Markl et al. 2016). Thus, our proposed slower reduction of sulfate to sulfide than arsenate/arsenite to arsenide might also be relevant at temperatures well above 200°C.

The transition to the sulfide stage is indicated by the formation of sulfosalts and base metal sulfides. This and the typical reaction textures of native silver and native bismuth to sulfosalts indicates the increase in sulfide at the transition from the arsenide to the sulfide stage. This can be attributed to either the delayed reduction of sulfate to sulfide or by an influx of sulfide/mixing of a sulfide bearing fluid.

Acknowledgements

Special thanks to Philippe Blanc for implementing thermodynamic data into the Thermoddem database. We also want to thank Wolfgang Bach, Thomas Wenzel, Sebastian Staude, Udo Neumann and Samuel Scharrer for feedback and/ or help plotting the thermodynamic model.

References

Bagheri H, Moore F, Alderton D (2007) Cu–Ni–Co–As (U) mineralization in the Anarak area of central Iran. J Asian Earth Sci 29:651-665.

Bastin ES (1939) The nickel-cobalt-native silver ore type. Econ Geol 34:40-79.

Bastin ES (1949) Deposition and resolution of native silver at Gowganda, Ontario. Econ Geol 44:437-444.

Baumann L, Kuschka E, Seifert T (2000) Lagerstätten des Erzgebirges. Enke, Stuttgart.

Bethke CM (2007) Geochemical and biogeochemical reaction modeling. Cambridge University Press.

Blanc P, Lassin A, Piantone P, Azaroual M, Jacquemet N, Fabbri A, Gaucher EC (2012) Thermoddem: A geochemical database focused on low temperature water/rock interactions and waste materials. Appl Geochem 27:2107-2116.

Bouabdellah M, Maacha L, Levresse G, Saddiqi O (2016) The Bou Azzer Co–Ni–Fe–As (±Au±Ag) district of Central Anti-Atlas (Morocco): A long-lived late Hercynian to Triassic magmatic-hydrothermal to low-sulphidation epithermal system In:

Bouabdellah M, Slack JF (eds) Mineral Deposits of North Africa. Springer, Cham, Switzerland, pp 19.
Burisch M, Gerdes A, Walter BF, Neumann U, Fettel M, Markl G (2017) Methane and the origin of five-element veins: Mineralogy, age, fluid inclusion chemistry and ore forming processes in the Odenwald, SW Germany. Ore Geol Rev 81:42-60.
Cheilletz A, Levresse G, Gasquet D, Azizi-Samir M, Zyadi R, Archibald DA, Farrar E (2002) The giant Imiter silver deposit: Neoproterozoic epithermal mineralization in the Anti-Atlas, Morocco. Miner Deposita 37:772-781.
Dolníček Z, Fojt B, Prochaska W, Kučera J, Sulovský P (2009) Origin of the Zálesí U–Ni–Co–As–Ag/Bi deposit, Bohemian Massif, Czech Republic: fluid inclusion and stable isotope constraints. Miner Deposita 44:81.
Essarraj S, Boiron M-C, Cathelineau M, Tarantola A, Leisen M, Boulvais P, Maacha L (2016) Basinal brines at the origin of the Imiter Ag-Hg deposit (Anti-Atlas, Morocco): Evidence from LA-ICP-MS data on fluid inclusions, halogen signatures, and stable isotopes (H, C, O). Econ Geol 111:1753-1781.
Fanlo I, Subías I, Gervilla F, Manuel J (2006) Textures and compositional variability in gersdorffite from the Crescencia Ni–(Co–U) showing, Central Pyrenees, Spain: primary deposition or re-equilibration? Can Mineral 44:1513-1528.
Gillerman E, Whitebread DH (1953) The Uranium-bearing Nickel-cobalt-native Silver Deposits in the Black Hawk District, Grant County, New Mexico US Geol Surv Bull. US Government Printing Office, pp 313.
Heimig C (2015) Ni-Co-As-Ag-Bi-Mineralisationen aus dem Odenwald Petrology and Mineral Resources. Eberhard Karls university, Tübingen, Germany, pp 119.
Hiller A, Schuppan W (2008) Geologie und Uranbergbau im Revier Schlema-Alberoda Bergbau in Sachsen. pp 200.
Hofmann (1986) Die Freiberger Mineralien. Lapis 11:13-60.
Kerrich R, Strong D, Andrews A, Owsiacki L (1986) The silver deposits at Cobalt and Gowganda, Ontario. III: Hydrothermal regimes and source reservoirs-evidence from H, O, C, and Sr isotopes and fluid inclusions. Can J Earth Sci 23:1519-1550.
Kiefer S, Majzlan J, Chovan M, Števko M (2017) Mineral compositions and phase relations of the complex sulfarsenides and arsenides from Dobšiná (Western Carpathians, Slovakia). Ore Geol Rev 89:894-908.
Kissin SA, Kisvarsany G, Grant S (1988) Nickel-cobalt-native silver (five-element) veins: A riftrelated ore type North american conference on tectonic control of ore deposits and the vertical and horizontal extent of ore systems. Univ. Missouri Press, Rolla, pp 12.
Kissin SA (1992) Five-element (Ni-Co-As-Ag-Bi) veins. Geoscience Canada 19:113-124.
Kissin SA (1993) The geochemistry of transport and deposition in the formation of five-element (Ag-Ni-Co-As-Bi) veins Eight Quadrennial International Association on the Genesis of Ore Deposits Symposium. Schweizerbart'sche Verlagsbuchhandlung, pp 14.
Kotková J, Kullerud K, Šrein V, Drábek M, Škoda R (2017) The Kongsberg silver deposits, Norway: Ag-Hg-Sb mineralization and constraints for the formation of the deposits. Miner Deposita:1-15.
Kreissl S, Gerdes A, Walter B, Neumann U, Wenzel T, Markl G (2018) Reconstruction of a >200 Ma multi-stage “five element” Bi-Co-Ni-Fe-As-S system in the Penninic Alps, Switzerland. Ore Geol Rev 95:746-788.
Kumovav (2017) European Cobalt Ltd annual financial report for the year endend 30 June 2017
Levresse G, Bouabdellah M, Cheilletz A, Gasquet D, Maacha L, Tritlla J, Banks D, Rachid ASM (2016) Degassing as the Main Ore-Forming Process at the Giant Imiter Ag–Hg Vein Deposit in the Anti-Atlas Mountains, Morocco Mineral Deposits of North Africa. Springer, pp 22.
Lipp U, Flach S (2003) Wismut-, Kobalt-, Nickel-und Silbererze im Nordteil des Schneeberger Lagerstättenbezirkes Bergbau in Sachsen. pp 215.
Markl G, Burisch M, Neumann U (2016) Natural fracking and the genesis of five-element veins. Miner Deposita 51:703-712.
Marshall D, Watkinson D (2000) The Cobalt mining district: Silver sources, transport and deposition. Exploration and Mining Geology 9:81-90.
Müller H (1860) Der Erzdistrict von Schneeberg im Erzgebirge. Cotta's Gangstud 3:1-223.
Ohmoto H, Lasaga AC (1982) Kinetics of reactions between aqueous sulfates and sulfides in hydrothermal systems. Geochim Cosmochim Ac 46:1727-1745.
Ondrus P, Veselovsky F, Gabasova A, Drabek M, Dobes P, Maly K, Hlousek J, Sejkora J (2003a) Ore-forming processes and mineral parageneses of the Jáchymov ore district. J GeSci-Czech 48:157-192.
Paar DIDW, Chen T (1979) Gersdorffit (in zwei Strukturvarietäten) und Sb-hältiger Parkerit, Ni3 (Bi, Sb) 2 S2, von der Zinkwand, Schladminger Tauern, Österreich. Tscher Miner Petrog 26:59-67.
Pekov IV, Levitskiy VV, Krivovichev VG (2010) Mineralogy of the Belorechenskoye deposit (Northern Caucasus, Russia). Mineral Almanac 15:1-96.
Petruk W (1968) Mineralogy and origin of the Silverfields silver deposit in the Cobalt area, Ontario. Econ Geol 63:512-531.
Petruk W (1971b) Mineralogical characteristics of the deposits and textures of the ore minerals. Can Mineral 11:108-139.
Robinson B, Ohmoto H (1973) Mineralogy, fluid inclusions, and stable isotopes of the Echo Bay U-Ni-Ag-Cu deposits, Northwest Territories, Canada. Econ Geol 68:635-656.
Scharrer M, Kreissl S, Markl G (in review) The mineralogical variability of hydrothermal native element-arsenide (five-element) mineralizations and the role of aqueous sulfide
Staude S, Wagner T, Markl G (2007) Mineralogy, mineral compositions and fluid evolution at the Wenzel hydrothermal deposit, Southern Germany: Implications for the formation of Kongsberg-type silver deposits. Can Mineral 45:1147-1176.
Staude S, Werner W, Mordhorst T, Wemmer K, Jacob DE, Markl G (2012) Multi-stage Ag–Bi–Co–Ni–U and Cu–Bi vein mineralization at Wittichen, Schwarzwald, SW Germany: geological setting, ore mineralogy, and fluid evolution. Miner Deposita 47:251-276.
Wagner T, Lorenz J (2002) Mineralogy of complex Co-Ni-Bi vein mineralization, Bieber deposit, Spessart, Germany. Mineralogical Magazine 66:385-407.

A new look at the geology of the White Pine Cu-Ag deposit and the Midcontinent Rift System

Simon M. Jones[1,2], Jonathan Cloutier[1,3], Timothy D. Raub[1], Anthony R. Prave[1]
[1]*University of St Andrews, UK*
[2]*First Quantum Minerals Ltd*
[3]*University of Tasmania (CODES)*

Abstract. The White Pine Cu-Ag deposit in the Midcontinent Rift System (MRS) is one of the archetype sediment-hosted stratiform copper deposits, with an initial resource of ~10Mt contained Cu metal. A reinterpretation of reflection seismic data shows the basin lacks many features characteristic of rifts such as syn-sedimentary faults and alluvial fans. Mineralisation is hosted in the ~1.1 Ga Oronto Group, between braided fluvial sandstone and conglomerate of the Copper Harbor Formation, and siltstones and shales of the Nonesuch Formation deposited in an estuarine setting during a marine transgression. New stable isotope and petrographic data reveal the ingress of seawater into the Copper Harbor Formation aquifer that facilitated the leaching of metals from basaltic detritus during diagenesis. The mineral paragenesis suggests that rapid burial compaction of the aquifer, in tandem with incipient inversion, drove fluid flow. Formation waters re-utilised earlier petroleum migration pathways, flowing towards the margins of the sag basin where they were focused by faults on the margins of a paleo-topographic high. Metals were deposited in a zoned sequence during thermochemical sulphate reduction across a redox front of liquid petroleum and *in situ* organic matter.

1 Introduction

Sediment-Hosted Stratiform Copper (SHSC) deposits are one of the major sources of Cu worldwide. They are believed to form in rift basins containing evaporite sequences, from the interaction of moderate temperature, highly saline, oxidised and metal-bearing brines with reduced lithologies such as organic-rich shales or liquid hydrocarbon traps (Hitzman et al. 2005). The Midcontinent Rift System (MRS) of the American Mid-west is anomalous to other rift systems containing SHSC deposits as it contains an unusually large volume of mafic rocks, no known evaporite sequences, significant native copper mineralisation, and is hosted in shales of lacustrine origin rather than marine (Elmore 1989). Previous interpretations of reflection seismic data identified syn-sedimentary and syn-volcanic faults on the basin margins (Cannon et al. 1989; Dickas & Mudrey 1997). The sedimentary fill of the basin was interpreted as early alluvial fans shedding conglomerates into a half-graben subsequently filled by lacustrine siltstones and shales (Daniels 1982).

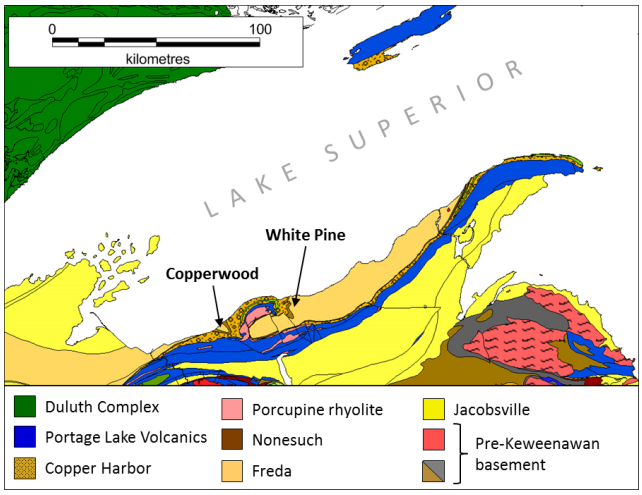

Figure 1. Simplified geological map of western Lake Superior region showing the location of the principal Cu-Ag deposits.

Prevailing models for the formation of SHSC mineralisation at White Pine, Copperwood and nearby prospects suggest fluids were driven by volcanism (Brown 2014a), gravity compaction (Swenson et al. 2004), meteoric recharge (Brown 2014b) or a combination thereof. A second phase of mineralisation is interpreted to have formed around thrust faults during subsequent (Grenville orogeny) basin inversion at 1047 ± 35 Ma (Ruiz et al. 1984; Mauk et al. 1992). Here we present new interpretations of reflection seismic data, new data on core and outcrop including C-O isotopes on carbonate rocks, sulphur isotopes on sulphide minerals and H-O isotopes on authigenic clays. A detailed paragenesis is compiled from petrography and drill core observations with peak temperature estimates and characterisation of alteration minerals derived from X-Ray Diffraction (XRD). We combine these data into a holistic understanding of the mineral system, the geodynamic and structural evolution of the basin, the stratigraphic framework for the Oronto Group, the changing nature of the pore fluids within these rocks and the factors that influenced the timing of fluid flow.

2 Geological setting

The MRS is a c. 2000 kilometre-long arcuate feature of dense and magnetic rocks in the eastern portion of the Laurentian continent, interpreted commonly as a failed rift (Cannon 1994; Stein et al. 2014). That is based on reflection seismic data in which basin-margin, syn-volcanic and syn-sedimentary faults have been inferred

(Cannon et al. 1989; Dickas and Mudrey 1997). The basin fill consists of a lower sequence c. 20 km thick of basaltic volcanic rocks and an upper sequence c. 10km thick of sedimentary rocks that constitute the Keweenaw Supergroup (Ojakangas et al. 2001). Volcanic rocks are overlain by the Oronto Group, which from the base upwards includes the Copper Harbor, Nonesuch and Freda formations. The Copper Harbor Formation contains lithic arenites and conglomerates interpreted as alluvial fans (Elmore 1984) with multiple minor volcanic units (Baumann et al. 2018). The Nonesuch Formation conformably overlies the Copper Harbor Formation (Daniels 1982), comprising siltstones and shales including organic-rich and micritic beds and is interpreted to be of a lacustrine origin (Elmore 1989), although organic geochemistry studies have highlighted evidence of marine influences (e.g. Hieshima and Pratt 1991). The Freda Formation is a brown-coloured alluvial sandstone of greater textural and compositional maturity than the Copper Harbor Formation (Daniels 1982). In the western Lake Superior sub-basin, the Oronto Group is unconformably overlain by the sub-arkosic Jacobsville Sandstone (Kalliokoski 1982). Placed within the context of a rift basin, the Copper Harbor Formation alluvial fans were shed into half grabens filled subsequently with lacustrine siltstones and shales of the Nonesuch Formation (Daniels 1982). Contrasting explanations for why the MRS failed to extend to develop oceanic crust include compression related to the Grenvillian Orogeny (Cannon 1994) or extension accommodated elsewhere on the margin of Laurentia (Stein et al. 2014).

3 Results

3.1 Basin architecture

A total of 21 reflection seismic lines have been collected across Lake Superior, imaging the subsurface to a depth of up to ~30km (e.g. Behrendt et al. 1988). Our interpretation of the seismic data shows that the volcanic rocks, including the Portage Lake Volcanic (PLV) flows, display a draped geometry with units thickening towards the centre of the basin. An unconformity surface truncates the top of the volcanic units, cutting deeper into stratigraphy at topographic highs and at the margins of the basin. The low resolution of the seismic data prohibits the identification of individual formations above this unconformity. Clinoforms within the lower Oronto Group show clear onlap of units onto this unconformity surface and infill a pre-existing topography. Clinoforms within the lower Oronto Group, interpreted to be Copper Harbor Formation, prograde systematically northward into the basin centre. The uppermost units imaged in the seismic data lie above an unconformity although it is unclear if the surface is the base of the Freda Formation, Jacobsville Sandstone or another unit. Late reverse faults are present on the northern and southern margins of the basin. The faults ramp up through stratigraphy becoming steeper near the surface and displaying offsets of 10 - 20 km. All volcanic and sedimentary units show constant thicknesses across faults.

3.2 Stratigraphy and sedimentology

The surface at the top of the PLV is a gentle undulating surface with a locally-developed paleosol, overlain unconformably by a relatively well-sorted sandstone unit. The Copper Harbor Formation varies from 115 m to ~1400 m in thickness and its lower part is dominated by conglomerate with well-rounded cobble to boulder-sized clasts of mostly basalt reworked from the underlying PLV Group. Beds are 2-3m thick and display imbrication and subtle upward fining. Upwards, the conglomerate becomes interbedded with trough and planar cross-bedded sandstone, in upward fining channelized beds. The topmost units are dominated by sandstone that locally fines up into shale and contains stromatolites, evaporite minerals, flaser bedding and features indicative of a sabkha. The distribution of these facies extends over tens of kilometres laterally, with grainsize fining vertically and laterally away from basement highs. The Copper Harbor – Nonesuch Formation contact is conformable and is commonly interbedded over several meters. The basal Nonesuch Formation contains abundant organic-rich shales, microbial mat textures, syneresis and desiccation cracks, flat-top ripples and heterolithic bedding. These units are overlain by a more homogenous fine-grained, dark siltstone recognisable across the basin. The unit also contains abundant flaser bedding. A third unit at the top of the Nonesuch Formation contains coarser-grained sands and silts with hummocky-cross stratification and evidence of cyclical flow reversals. Brown fluvial sandstones of the Freda Formation lie unconformably above the Nonesuch Formation on an erosional surface which cuts downward through stratigraphy towards the southwest.

3.3 Mineral paragenesis

Approximately 200 thin sections were examined with a focus on the paragenetic sequence and spatial distribution of authigenic minerals. Framework grains in the Copper Harbor Formation show hematite coatings that appear coeval with early tangential anisopachous smectitic rims. The smectite content varies from zero to completely filling pore throats. The upper Copper Harbor Formation from the White Pine and Copperwood areas shows evidence of widespread hematite destruction resulting in a colour change from red-brown to grey or beige across an area of ~25 x 25km. A zone of neoformed isopachous chlorite rims is present in the lower Nonesuch and uppermost Copper Harbor formations beneath White Pine. Chlorite rims overgrew and possibly replaced earlier smectite rims. The zone of chlorite alteration attains a maximum thickness of up to 10 m on the southwest side of the White Pine fault. Pyrobitumen (solidified petroleum) fills many interstitial pores, post-dating chlorite rims, with which it displays a close spatial association. Native copper commonly mantles pyrobitumen in interstitial pores and copper sulphides replace pyrite that has nucleated on the surfaces of detrital and authigenic chlorite grains.

Syntaxial quartz overgrowths commonly fill pores and post-date copper mineral grains. Quartz cements are particularly well developed in quartz-rich sandstones and around grains that are not rimmed by smectite or chlorite. Grain dissolution textures, including framework quartz grains, are commonly infilled by a late poikilotopic calcite cement.

3.4 White Pine deposit geology

The bulk of copper mineralisation is hosted in carbonaceous siltstones and shales of the basal Nonesuch Formation. The zonation of ore minerals, from the base upwards, includes ~0 to 5m of native copper, a chalcocite zone up to ~10m thick, and an upper ~50cm thick zone of bornite, chalcopyrite and greenockite (CdS). Native silver is concentrated in the uppermost ~30cm of the Copper Harbor Formation. Native copper mineralisation is stratigraphically restricted to pyrobitumen-bearing Copper Harbor Formation sandstones and the lowermost Nonesuch Formation. Copper mineral zonation is peneconcordant and stratigraphically highest near the Porcupine rhyolite dome. Copper minerals are most often present in mm-scale sand laminae within the shales, with minor amounts in mm to cm-scale reverse faults. The copper mineral species in these reverse faults shows the same gross zonation pattern as disseminated copper mineralisation. The White Pine fault displays ~200 m of normal offset and evidence of syn-sedimentary movement (down to the southwest) that includes coarser sediments, thickened stratigraphy and erosional scouring in the hangingwall. The fault both focused and partitioned chlorite alteration, interstitial pyrobitumen and native copper mineralisation; the zones of which tend to be thickest in its hangingwall. Irregular, late pyrobitumen veins show a close spatial and genetic relationship to faulting, and are cut by and re-utilised by calcite veins. High angle (~60˚) inverted normal faults offset mineralisation by 10s of meters.

3.5 Stable isotopes

Stable isotope analyses were completed on sulphide, carbonate and silicate phases from drill core samples across the basin. White Pine, Copperwood and other prospects displaying a similar style of mineralisation show a wide range of $\delta^{34}S$ values, of -24.2 to +29.9‰. A prospect containing structurally controlled chalcocite mineralisation displayed a bimodal distribution of $\delta^{34}S$ values of -25 and +15‰. Mineralisation from a stratigraphically lower basalt-hosted deposit and the Mount Bohemia diorite intrusion displays a tight cluster of values close to 0‰, suggesting a different and homogenous source of S. C and O isotopes were analysed in early and late concretions, micrite beds, interstitial cement and several vein generations. The $\delta^{18}O$ values varied from ~25‰ for early diagenetic features, ~18‰ for cement and ~15‰ for veins. Calcite cement from mineralised samples contains isotopically lighter C and O of ~-9 and ~18‰, respectively. Pre-ore authigenic chlorite coatings on framework grains record the δD and $\delta^{18}O$ of pore water shortly before ore formation. Samples were taken from several prospects across the basin and preliminary δD_{fluid} data (-1.4 to 26.2‰) show evidence of a marine-dominated fluid. Oxygen isotope data are pending.

3.6 X-Ray diffraction

The <2μm matrix component of 190 samples was separated by centrifuge and decantation techniques, and analysed by XRD. Samples from the Iron River Syncline, a sub-basin southwest of White Pine, contain montmorillonite, beidellite, chlorite and minor vermiculite. Illite crystallinity values indicate peak temperatures of ~130˚C (n=4). Samples from White Pine and Copperwood contain variable amounts of illite and chlorite, and record temperatures of ~150˚C (n=34) and 135˚C (n=6) respectively. Northeast of White Pine, in a deeper portion of the basin, sandstones containing chlorite, illite and laumontite matrix minerals record peak temperatures of between 170 and 180˚C (n=4).

4 Discussion

Copper Harbor Formation sediments onlap an unconformity surface above the PLV Group, infilling an undulating paleo-topography. Sedimentary features within the Copper Harbor Formation are indicative of a braided fluvial deposit and we find no evidence to support the interpretation that it records syn-rift sedimentation. Lithofacies indicative of marine settings that occur in the uppermost Copper Harbor Formation and lowermost Nonesuch Formation suggest deposition in tidally-influenced shallow-marine setting: abundant desiccation cracks, evaporite minerals and sabkha features are evidence of periodic subaerial exposure. We envisage an embayment or estuarine setting in which circulation was sufficiently restricted so as to promote the preservation of organic matter.

The marine transgression that initiated Nonesuch Formation deposition would have resulted in seawater displacing meteoric water in the pores of the underlying Copper Harbor Formation. This is confirmed by the isotopically heavy δD_{fluid} values calculated from authigenic chlorite rims. The presence of evaporite minerals in the lower Nonesuch Formation suggests residual brines may also have percolated down into the Copper Harbor Formation aquifer, thus providing Cl^- ligands for metal transport.

Isopachous authigenic chlorite in the uppermost Copper Harbor Formation beneath White Pine is absent at grain-grain contacts suggesting formation during mesodiagenesis, after the onset of compaction. Chlorite and smectite rims appear to have inhibited silica cement, and in the case of chlorite, prevented over-compaction and pore collapse. Bleaching of hematite rims at White Pine and Copperwood is interpreted to be the result of iron dissolution at sites of high fluid flux. The attenuation of the aquifer around the Porcupine rhyolite forced ore-forming fluids to higher stratigraphic levels. Thicker shale units in the hanging walls of syn-

sedimentary faults (e.g. White Pine fault) promoted ore deposition lower in the stratigraphy. The top of the native copper zone varies in concert with that of the copper sulphide zones above, and formed in the same paragenetic window, suggesting sulphides and native metals formed coevally under a common redox architecture. Sulphur isotope data imply thermochemical sulphate reduction was the main precipitation mechanism of the sulphides. The presence of minor amounts of ore in small-scale thrust faults that contain exclusively copper minerals suggests that the mineralisation extended into incipient basin inversion.

Paleo-temperature estimates correlate with inferred burial depths (and subsequent exhumation along the Keweenaw fault) and thus call into question interpretations suggesting thermal perturbations being driven by volcanism.

5 Conclusion

The Copper Harbor Formation was deposited on a paleo-topographic surface as a permeable and metal-rich source rock. A marine incursion into the basin resulted in a restricted embayment or estuarine setting that produced carbonaceous shales and brines which percolated into underlying sandstones. Breakdown of volcanic detritus in the Copper Harbor Formation during eo- and mesodiagenesis liberated metals into saline pore waters, initially producing (Mg-Fe) chlorite grain coatings that preserved aquifer porosity. Migrating petroleum was focused towards the edges of the basin and by basin-normal structures at White Pine and Copperwood deposits. Progressively deeper burial and compaction of the Copper Harbor Formation drove oxidised and saline Cu-Ag-bearing brines into these petroleum trap sites where metals precipitated upon reduction of the brines by liquid petroleum or *in situ* organic matter in shales. Sulphur was sourced primarily from thermochemical sulphate reduction of seawater. Normal geothermal gradients in the basin preclude volcanic thermal inputs as a fluid drive mechanism and meteoric recharge is discounted due to the abundant evidence of seawater influence. The location of ore deposits at topographic highs on the margins of the basin, and the timing of ore deposition (during compaction and sediment loading) suggest burial compaction as the dominant fluid drive mechanism. The process of mineralisation spanned incipient inversion, during which the same redox architecture governed metal zonation in the deposits. Mineralisation likely ceased when sediment-loading decelerated and primary permeability in the Copper Harbor Formation aquifer was degraded by pore-clogging quartz and calcite cements.

Acknowledgements

The authors wish to thank First Quantum Minerals for their generous funding of this project. Highland Copper for access to cores and samples and field logistics support. NERC funding for stable isotope studies and geochronology have also been instrumental.

References

Baumann, S.D., Dylka, S.K. and Malone, D.H., 2018. Lithostratigraphic subdivisions of the Mesoproterozoic Copper Harbor Formation (Oronto Group) in Michigan and Wisconsin, USA. STRATIGRAPHY, 15(2):135-152.

Behrendt, J.C., Green, A.G., Cannon, W.F., Hutchinson, D.R., Lee, M.W., Milkereit, B., Agena, W.F. and Spencer, C., 1988. Results from GLIMPCE deep seismic reflection profiles over the mid-continent rift system. Geology, 16:81-85.

Brown, A.C., 2014. Low-temperature sedimentary copper deposits.

Brown, A.C., 2014. Latent thermal effects from Porcupine Volcanics calderas underlying the White Pine-Presque Isle stratiform copper mineralization, northern Michigan. Economic Geology, 109(7):2035-2050.

Cannon, W.F., 1994. Closing of the Midcontinent rift-A far—field effect of Grenvillian compression. Geology, 22(2):155-158.

Cannon, W.F., Green, A.G., Hutchinson, D.R., Lee, M., Milkereit, B., Behrendt, J.C., Halls, H.C., Green, J.C., Dickas, A.B., Morey, G.B. and Sutcliffe, R., 1989. The North American Midcontinent rift beneath Lake Superior from GLIMPCE seismic reflection profiling. Tectonics, 8(2):305-332.

Daniels Jr, P.A., 1982. Upper Precambrian sedimentary rocks: Oronto Group, Michigan-Wisconsin. Geology and tectonics of the Lake Superior basin: GSA Memoir, 156:107-133.

Dickas, A.B., Mudrey, M.G., Ojakangas, R.W. and Green, J.C., 1997. Segmented structure of the middle Proterozoic Midcontinent rift system, North America. SPECIAL PAPERS-GEOLOGICAL SOCIETY OF AMERICA, pp.37-46.

Elmore, R.D., 1984. The Copper Harbor Conglomerate: A late Precambrian fining-upward alluvial fan sequence in northern Michigan. Geol. Society of America Bulletin, 95(5):610-617.

Elmore, R.D., Milavec, G.J., Imbus, S.W. and Engel, M.H., 1989. The Precambrian Nonesuch Formation of the North American mid-continent rift, sedimentology and organic geochemical aspects of lacustrine deposition. Prec. Res. 43(3):191-213.

Hieshima, G.B. and Pratt, L.M., 1991. Sulfur/carbon ratios and extractable organic matter of the Middle Proterozoic Nonesuch Formation, North American Midcontinent rift. Precambrian research, 54(1):65-79.

Hitzman, M., Kirkham, R., Broughton, D., Thorson, J. and Selley, D., 2005. The sediment-hosted stratiform copper ore system. Economic geology, 100.

Kalliokoski, J., 1982. Jacobsville Sandstone. Geology and Tectonics of the Lake Superior Basin: GSA Mem. 156,147-156.

Mauk, J.L., Kelly, W.C., Van Der Pluijm, B.A. and Seasor, R.W., 1992. Relations between deformation and sediment-hosted copper mineralization: Evidence from the White Pine part of the Midcontinent rift system. Geology, 20(5):427-430.

Ojakangas, R.W., Morey, G.B. and Green, J.C., 2001. The Mesoproterozoic midcontinent rift system, Lake Superior region, USA. Sedimentary Geology, 141:421-442.

Ruiz, J., Jones, L.M. and Kelly, W.C., 1984. Rb-Sr dating of ore deposits hosted by Rb-rich rocks, using calcite and other common Sr-bearing minerals. Geology, 12(5):259-262.

Stein, C.A., Stein, S., Merino, M., Randy Keller, G., Flesch, L.M. and Jurdy, D.M., 2014. Was the Midcontinent Rift part of a successful seafloor-spreading episode? Geophysical Research Letters, 41(5):1465-1470.

Swenson, J.B., Person, M., Raffensperger, J.P., Cannon, W.F., Woodruff, L.G. and Berndt, M.E., 2004. A hydrogeologic model of stratiform copper mineralization in the Midcontinent rift system, northern Michigan, USA. Geofluids, 4(1):1-22.

Textural and mineralogical constraints on the mode of formation of the Bou Azzer Co-Ni arsenide mineralization (Anti-Atlas, Morocco): Tectonic implications.

Enora Tourneur, Alain Chauvet
University of Montpellier, France

Kalin Kouzmanov
University of Geneva, Switzerland

Johann Tuduri
BRGM, France

Stanislas Sizaret
ISTO, Geosciences Campus, France

Abstract. The Bou Azzer inlier is thought to represent a suture zone within a Neoproterozoic orogeny. The Bou Azzer inlier is composed of an assumed ancient oceanic crust of serpentinized ultramafic rocks, gabbro and basaltic pillow rocks. This inlier hosts the Co-Ni ore deposit of Bou Azzer with two types of mineralization: i) massive, elongated ore bodies, known as "*contact"* type mineralization, along the contact between serpentinite, quartz diorite and Precambrian volcanic rocks; and ii) a "*cross-cutting*" type represented by faults that cut all units, only mineralized at the vicinity of the "*contact*" type. A detailed mineralogical and textural study brings new arguments on the ore-formation processes at Bou Azzer. First, it appears that both types of mineralization are developed within a progressive and continuous tectono-hydrothermal stage as shown by the mineralogical evolution. Second, the "contact" type exhibits two aspects: i.e., Laminated Contact Mineralization (LCM) and Breccia-Related Contact Mineralization (BRCM) that are related to different initial textures of the pre-mineralization host rocks. Third, Ni-Co mineralization seems to have developed by replacement of spinel/magnetite grains of the serpentinite. All these observations are consistent with ore formation along a tectonic contact which explains the existence of serpentinite fragments slope breccia.

1 Introduction

Various cobalt mineralization styles on Earth cannot be attributed to a single ore-forming model. At least, six major mineralization styles are known: 1) sediment-hosted stratiform Cu-Co deposits (Fay and Barton 2012); 2) ortho-magmatic sulfide deposits (Naldrett et al. 1998); 3) Co from lateritic profiles mainly exploited for Ni (Orloff 1968); 4) Co-rich crusts associated with Mn-nodules within seawater hydrothermal oxidizing venting environment (Hein et al. 2000); 5) hydrothermal/volcanogenic deposits (the Bou Azzer district) (Leblanc 1975; En-naciri 1995); 6) Five elements (Ni-Co-As-Ag-Bi) vein-type deposits (Kissin 1988; Markl et al. 2016; Burish et al. 2017). At Bou Azzer, two types of ore bodies exist – the "contact" and the "cross-cutting" types. Yet, their mode of formation remains unclear, especially regarding their relationship with large-scale geodynamic processes. In this study, we present and discuss: i) mineralogical and paragenetic features that favor coeval processes of formation for the two mineralization types at Bou Azzer; ii) new textural observations helping to discuss the pre-mineralization tectonic context and its implication on the presently admitted classical model of Precambrian ophiolite for the Bou Azzer inlier (Leblanc 1976, Gasquet et al. 2005).

2 The Bou Azzer – El Graara inlier and the deposits

The Bou Azzer – El Graara inlier, oriented NW-SE, is located in the central part of the Moroccan Anti-Atlas, south of Ouarzazate. This inlier is composed of a dismembered but complete sequence of an assumed ancient oceanic crust made of serpentinized ultramafic rocks overlaid by gabbroic and basaltic pillow rocks (Leblanc 1975, 1976, 1981; Bodinier et al. 1984). This area is thus interpreted as being a suture zone related to the Neoproterozoic orogeny (e.g. Choubert 1963; Leblanc and Lancelot 1980; Saquaque 1992). The tectono-magmatic evolution of this area (Tuduri et al. 2018) involves a first event, associated with the emplacement of large volumes of high-K calc-alkaline magmas in meta-sediments that were deformed under transpressive tectonic control (the Lower Complex). A second transtensive deformational event is associated with intense magmatism, volcanism and deposition of volcano-clastic sediments (the Upper Complex). The Precambrian group of Ouarzazate, characterizing the Upper Complex, is composed of dacitic to rhyolitic ignimbrites and andesitic tuffs (Mifdal and Peucat 1985); all intruded by a calc-alkaline to highly potassic plutonic rocks. All these Precambrian units are covered by the Cambrian sedimentary cover (Pouit 1966; Bouchta et al.

1977; Gasquet et al. 2001).

3 Textural and paragenetic constraints on the mineralization

3.1 The Co-Ni ore deposits of Bou Azzer

Two types of ore bodies occur in the Bou Azzer district, as defined by Leblanc (1975) and En-naciri (1995) (Fig. 1):

i) The massive "*contact"* type is composed by Co-Ni-Fe arsenides hosted within a siliceous or carbonaceous gangue. This mineralization is developed systematically at the contact between serpentinites and quartz-diorite and/or Upper complex volcanic rocks, located south and north of the serpentinite occurrences, respectively.

ii) The "*cross-cutting"* type is composed of Co-Fe arsenide mineralization, within K-feldspar, quartz and carbonate veins. These veins intersect all units, and are only mineralized at the vicinity of the "contact" type ore bodies.

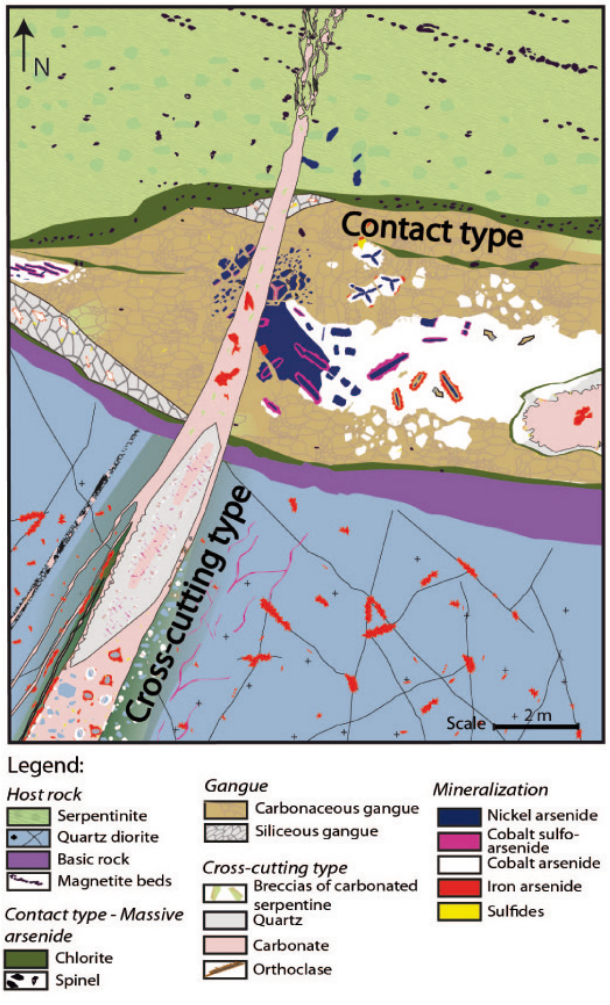

Figure 1. Model of formation of the Bou Azzer Co-Ni-rich arsenide ore deposit showing the distribution of the mineralization stages within the "*contact"* and the "*cross-cutting"* type mineralization.

Six paragenetic stages are recognized at Bou Azzer: 1) a Ni-arsenide stage with nickeline (NiAs) and rammelsbergite ($NiAs_2$); 2) a Co-arsenide stage with skutterudite ($CoAs_3$) and safflorite ($CoAs_2$); 3) a Co-sulfo arsenide stage with cobaltite (CoAsS); 4) a Fe-arsenide stage with loellingite ($FeAs_2$); 5) a Fe sulfo-arsenide stage with arsenopyrite (FeAsS); and 6) a sulfide stage with chalcopyrite, sphalerite, galena, and fahlores. The six stages are observed within the contact type mineralization, all included in a carbonaceous and a siliceous gangue, whereas only the last four stages occur in the "cross-cutting" type.

A petro-structural model is proposed in order to integrate the six mineralization stages within three main events which lead to the formation of the Bou Azzer deposits (Fig. 1):

1) a Ni-Co-rich arsenide stage composed of nickeline, rammelsbergite and subsequent cobaltite and skutterudite;

2) the formation of the siliceous or carbonaceous gangue associated with the late Co-rich arsenide and the earlier Fe-rich sulfo-arsenide minerals;

3) the formation of the cross-cutting structures mainly hosts the final stage of the Co-rich arsenide mineralization and the Fe-Cu-bearing sulfide minerals, both occurring in veins mainly composed of K-feldspar (minor), quartz and carbonate.

3.2 Textural observations on the massive type

A detailed textural analysis of the "contact" type mineralization led to the following observations:

1. The massive arsenide-rich parts of the mineralization show two distinct textural features:

- Massive lenses of lamellar nickeline surrounded by skutterudite sometimes alternating with carbonate forming a banded texture (Fig. 2a).

- Massive lenses of arsenides with isolated nuclei of elongated rammelsbergite surrounded by cobaltite, carbonate, skutterudite and chalcopyrite, all included within large euhedral skutterudite and with late carbonate (Fig. 2b);

2. The gangue of the contact mineralization is mainly carbonaceous and may exhibit several inherited fragments of serpentinite (Fig. 3a), indicating the nature of the host rock (serpentinite) prior to the formation of the mineralized structure;

3. Skutterudite is commonly fractured, with neo-serpentine infilling (Fig. 3b). This demonstrates that the serpentinization was still active during at least the earliest mineralization stages.

4. Spinels and rammelsbergites entirely replaced by spinel are observed within the serpentinite close to the contact (Fig. 3b). Spinels are systematically bordered by magnetite (Fig. 3c) or rammelsbergite (Fig. 3b). In addition, cathodoluminescence imaging shows relics of spinel frequently occurring in the core of the carbonaceous gangue (Fig. 3c). This demonstrates again that serpentinite was the precursor of the mineralized gangue.

5. Cathodoluminescence imaging of the carbonaceous gangue shows that two textures co-exist: i) one dominated by large euhedral crystals evolving

toward, ii) fragmented grains with a lot of space between them. This last texture seems to be related to dilatation breccia formed within a stress-free open space (Fig. 3d) (Jébrak 1997; Chauvet 2019).

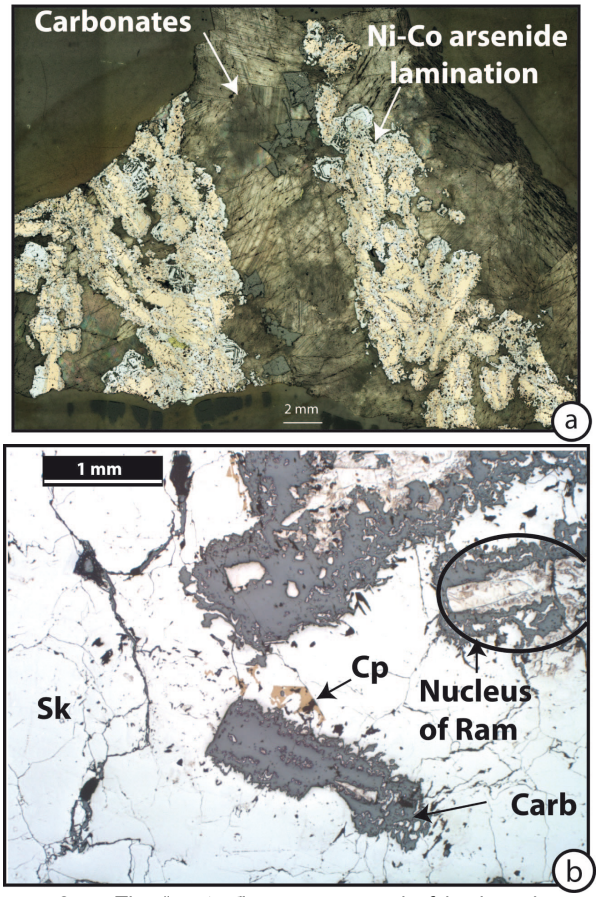

Figure 2. a. The "*contact*" type composed of laminated contact mineralization (LCM) of Ni-Co rich arsenide then surrounding by carbonate (image in reflected light). **b.** Nucleus of Rammelsbergite surrounding by skutterudite, carbonate, chalcopyrite, in a massive gangue of skutterudite and carbonates, indicates a brecciated-related environment of the contact mineralization (BRCM) (image in reflected light). Carb: carbonate, Co: Cobalt, Cp: Chalcopyrite, Ni: Nickel, Ram: Rammelsbergite, Sk: skutterudite

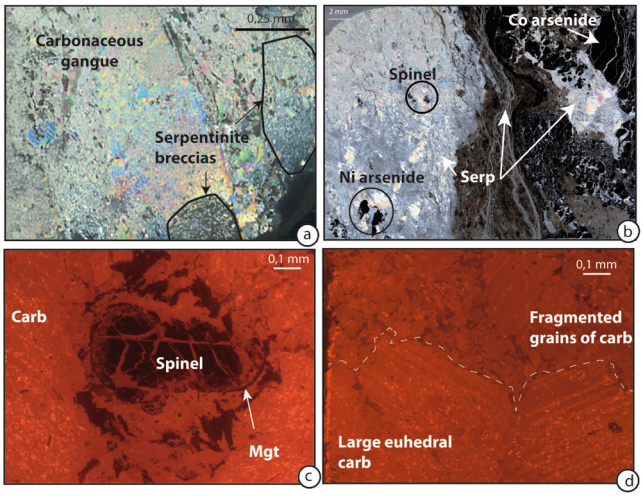

Figure 3. a. Fragments of a previously serpentinite in the carbonaceous gangue (image in polarized light) **b.** Few information of texture is visible: fractured skutterudite by serpentinite, spinel entirely replaced by rammelsbergite, spinel is observed in the serpentinite host rock (image in polarized light). **c.** Spinel is included also in the carbonaceous gangue of the "contact" type, is bordered by magnetite (image of cathodoluminescence – CL). **d.** The carbonaceous gangue shows two types of texture: brecciated texture of thin carbonates and euhedral texture of large carbonates (image of CL). Carb: carbonate, Co: Cobalt, Mgt: Magnetite, Ni: Nickel, Ram: Rammelsbergite, Serp: serpentinite

4 Formation of the Bou Azzer ore deposit and tectonic implications

We draw two main conclusions from the textural and mineralogical analysis of the Bou Azzer mineralization:

- The mineralogical evolution of both "contact" and "cross-cutting" mineralization types results from a progressive and continuous process that begins with Ni-Co ore formation followed by Co-Fe-Cu-rich stages. The Ni-Co stages are encountered exclusively within the "contact" type while the Co/Fe/Cu stages developed in both structures. This suggests that both mineralization types, i.e. the contact and the cross-cutting ones, are produced during the same tectono-mineralogical event, although the "contact" type ore bodies formed first.

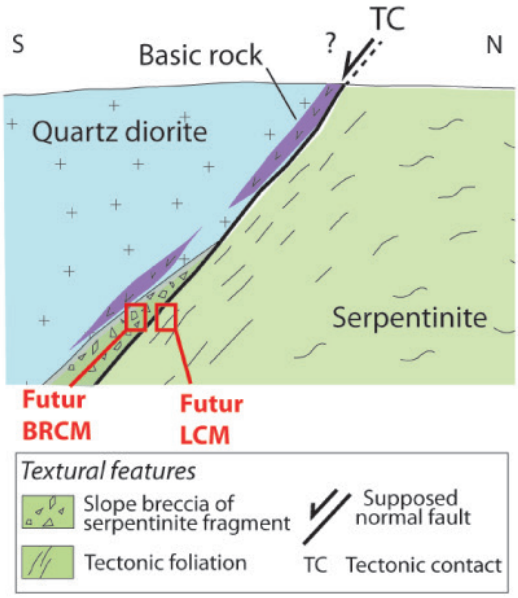

Figure 4. An example of hypothetic tectonic context consistent with the formation of serpentinite breccia that serves as receptacle for mineralization. In that case, fault motion need to be normal. (BRCM: Brecciated-related contact mineralization; LCM: Laminated contact mineralization)

- The textural features within the "*contact*" type demonstrate that these domains result from replacement and hydrothermal processes that affect a serpentinite rock. Textural constraints indicate that most of the ore bodies derived from serpentinite breccia could form Breccia-related Contact Mineralization (BRCM); although some may have been formed by the transformation of banded serpentinite levels, Laminated Contact Mineralization (LCM) (Fig. 4). It is suggested that such brecciated areas, characterized by high permeability, are favorable domains for fluid circulation

and subsequent ore formation.

- The occurrence of spinel relics bordered by magnetite and rammelsbergite confirms the hypothesis of replacement of serpentinite levels. It is suggested that spinel and magnetite fragments are at the origin of the Ni/Co-rich arsenides whereas serpentinite ones formed the gangues.

A first hypothesis regarding the tectonic context of ore formation at Bou Azzer is illustrated in figure 4. The brecciated levels, as precursors for the formation of the contact orebodies can result from the activity of normal faults and the geometrical constraints of the inlier. Such normal faults may have helped the exhumation of the serpentinized mantle in this area. However, they are inconsistent with the obduction scenario.

Acknowledgements

Managem and CTT mining companies are acknowledged for their support during field work and access to the mine sites. Part of the laboratory work was supported by the TelluS Program of CNRS/INSU. We also acknowledge Christophe Nevado and Doriane Delmas for their meticulous works on thin sections.

References

Bodinier JL, Dupuy C, Dostal J (1984) Geochemistry of Precambrian ophiolites from Bou Azzer, Morocco. Contributions to Mineralogy and Petrology 87(1):43–50. doi.org/10.1007/BF00371401

Bouchta R, Boyer F., Routhier P, Saadi M, Salem M (1977) L'aire cuprifère de l'Anti-Atlas (Maroc) : permanence et arêtes riches. C. R. Acad. Sc. Paris 284:503–506

Bursich M, Gerdes A, Walter B, Neumann U, Fettel M, Markl G (2017) Methane and the origin of five-element veins: Mineralogy, age, fluid inclusion chemistry and ore forming processes in the Odenwald, SW Germany. Ore Geology Reviews 81:42-61. doi.org/10.1016/j.oregeorev.2016.10.033

Chauvet A. (2019) Structural Control of Ore Deposits: The Role of Pre-Existing Structures on the Formation of Mineralised Vein Systems. Minerals 9(1):56

Choubert G. (1963) Histoire géologique du Précambrien de l'Anti-Atlas de l'Archéen à l'aurore des temps primaires. Notes et Mémoires du Service Géologique du Maroc 162:352

El Hadi H, Simancas JF, Martínez-Poyatos D, Azor A, Tahiri A, Montero P, Fanning CM, Bea F, González-Lodeiro F (2010) Structural and geochronological constraints on the evolution of the Bou Azzer Neoproterozoic ophiolite (Anti-Atlas, Morocco). Precambrian Research 182:1-14

En-naciri A (1995) Contribution à l'étude du district à Co, As, (Ni, Au, Ag) de Bou Azzer, Anti-Atlas (Maroc). Données minéralogiques et géochimiques: Etude des inclusions fluides. MGeol thesis University of Orleans

Gasquet D, Levresse G, Cheilletz A, Azizi-Samir MR, Mouttaqi A (2005) Contribution to a geodynamic reconstruction of the Anti-Atlas (Morocco) during Pan-African times with the emphasis on inversion tectonics and metallogenic activity at the Precambrian-Cambrian transition. Precambrian Research 140:157–182. doi.org/10.1016/j.precamres.2005.06.009

Hein JR, Koschinsky A, Bau M, Manheim FT, Kang JK, Roberts L (2000) Cobalt rich ferromanganese crusts in the pacific: In Marine mineral deposits, 1st edition, CRC Press, New York, pp 239–279

Inglis JD, D'Lemos RS, Samson SD, Admou H (2005) Geochronological Constraints on Late Precambrian Intrusion , Metamorphism, and Tectonism in the Anti-Atlas Mountains. The Journal of Geology 113:439–450

Jébrak M. (1997) Hydrothennal breccias in vein-type ore deposits: A review of mechanisms, morphology and size distribution. Ore Geology Reviews 12:111-134

Kissin SA (1992) Five-element (Ni-Co-As-Ag-Bi) veins: Geoscience Canada 19(3):113–124

Kissin SA (1988) Nickel-cobalt-native silver (five elemnt) veins: A rift-related ore type, in Kisvarsanyi, G. and Grant, SK, eds., Proceedings Volume, North American Conference on Tectonic Control of Ore Deposits and the Vertical and Horizontal Extent of Ore Systems. University of Missouri-Rolla, pp. 268-279

Leblanc M (1975) Ophiolites précambriennes et gîtes arseniés de cobalt (Bou Azzer, Maroc). MGeol thesis University of Montpellier

Leblanc M (1976) Proterozoic oceanic crust at Bou Azzer. Nature 261:34–35

Leblanc M (1981) The Late Proterozoic ophiolites of Bou Azzer (Morocco): evidence for Pan-African plate tectonics. In A. Kröner (Editor), Precambrian Plate Tectonics, Amsterdam, pp 435-451

Leblanc M. Lancelot JR. (1980) Interprétation géodynamique du domaine panafrican (Précambrian terminal) de l'Anti-Atlas (Maroc) à partir de données geologique et géochronologique. Canadien Journal of Earth Sc 17:142-155

Markl G, Burisch M, Neumann U (2016) Natural fracking and the genesis of five-element veins. Mineralium Deposita 51(6):703–712. doi.org/10.1007/s00126-016-0662-z

Mifdal A, Peucat JJ (1985) Datations U/Pb et Rb/Sr du volcanisme acide de l'Anti-Atlas marocain et du socle sous-jacent dans la région de Ouarzazate. Apport au problème de la limite Précambrien-Cambrien. Sciences Géologique Bulletin 38:185–200

Naldrett AJ, Federenko VA, Lightfoot PC, Gorbachev NS, Doherty W, Asif M, Lin Sh, Johan Z (1998) A model for the formation of the Ni-Cu-PGE deposits of the Noril'sk Region: In International Platinum, Theophrastus Publication, St Petersburg, pp 92–106

Pouit G (1966) Paléogéographie et répartition des minéralisations stratifomes de cuivre dans l'Anti-Atlas occidental (Maroc). Chron Rech Min 356: 279-289

Saquaque A. (1992) Un exemple de suture-arc: Le Precambrien de l'Anti-Atlas centre oriental (Maroc). MGeol thesis Université Cadi Ayyad

Thomas RJ, Fekkak A, Ennih N, Errami E, Loughlin SC, Gresse PG, Chevalier LP, Liégeois JP (2004) A new lithostratigraphic framework for the Anti-Atlas Orogen, Morocco. Journal of African Earth Sciences 39:217-226. doi.org/10.1016/j.jafrearsci.2004.07.046

Tuduri J, Chauvet A, Barbanson L, Labriki M, Dubois M, Trapy PH, Maacha L (2018) Structural control, magmatic-hydrothermal evolution and formation of hornfels-hosted, intrusion-related gold deposits: Insight from the Thaghassa deposit in Eastern Anti-Atlas, Morocco. Ore Geology Reviews, 97:171–198. doi.org/10.1016/j.oregeorev.2018.04.023

Galena trace element geochemistry of the precious and base metal-rich deposits in the Cyclades District, Greece

Sandra C. Wind, David A. Schneider
University of Ottawa, Canada

Mark D. Hannington
University of Ottawa, Canada
GEOMAR-Helmholtz Centre for Ocean Research Kiel, Germany

Abstract. The extensional back-arc setting in the Aegean Sea hosts polymetallic ore deposits that are temporally associated with the emplacement of Miocene granitoids and occur adjacent to major detachment systems. Various types of mineral deposits (e.g., carbonate replacement, skarn, vein-type, and low- to high-sulfidation epithermal) formed during different stages of back-arc evolution and can be found in the metamorphic basement, unmetamorphosed hanging wall and Quaternary volcanic units along the active volcanic arc. A comparison of the trace elements in galena from twelve deposits across the Cyclades District was carried out by LA-Q-ICP-MS analyses to identify possible geochemical similarities and differences at regional and local scales. The new trace element data demonstrates the usefulness of galena as an abundant and widespread indicator mineral for ore-forming fluids in the Cyclades. In addition to spot analyses, traverses through galena reveal compositional zoning, which indicates that changes in the fluid chemistry are encountered during crystal growth. Despite these variations, galena from the same deposit show small variations in trace element concentrations that appear to be characteristic of the particular setting and host rocks. Regional differences in trace element concentrations in galena reflect the conditions of mineralization and metal sources in the Cyclades District.

1 Introduction

Precious and base metal-rich deposits in the Cyclades District are temporally associated with different stages of the geodynamic evolution of the arc and back-arc (e.g., Skarpelis 2002). Recent studies by Melfos and Voudouris (2017) and Menant et al. (2018) highlighted the temporal change in mineralization styles and commodities in the Cyclades District. Despite the long mining history and detailed studies of the individual deposits, paragenetic models for many deposit types occurring in the Cyclades District remain controversial. This study compares the geochemistry of the different mineral deposits using galena, a widespread and abundant host for many trace elements, as a guide to the ore-forming fluids and metal sources of the Cyclades District. Recent trace element studies in galena by LA-ICP-MS (George et al. 2015) have shown that galena can contain a large variety of trace elements (e.g., Ag, Bi, Se, Sb, Cd, Tl, Te) that are indicative of the different source rocks, magmatic-hydrothermal influences, and conditions of mineralization.

2 Geological setting

The Cyclades District extends from the Lavrion Peninsula, south of Athens towards Milos and Santorini along the active Hellenic Volcanic Arc. Subduction of the African plate beneath continental Europe created an extensional back-arc setting accommodated by low-angle, crustal detachments. Two major tectono-metamorphic units can be distinguished in the Cyclades: the metamorphic basement divided into the Upper and Lower Cycladic Nappe, which are separated by the Trans Cycladic Thrust (Fig. 1, after Grasemann et al. 2018), and the unmetamorphosed Pelagonian Unit in the hanging wall of the major detachment systems. Intrusion of Miocene granitoids started before 15 Ma (e.g., Tinos) in the north-east, whereas magmatism in the west only started after 11 Ma (e.g., Lavrion, Serifos). Economic mineral deposits occur in all tectono-metamorphic units and are temporally and spatially associated with the detachments and Miocene granitoids as well as Pliocene-Quaternary volcanics along the volcanic arc.

2.1 Cyclades mineral district

The Cyclades mineral district spans the transition from Middle Miocene to modern seafloor hydrothermal systems along the volcanic arc (Fig. 1). The deposits have been classified as carbonate replacement Pb-Zn-Ag-(Au), low- to high-sulfidation epithermal, polymetallic and precious metal vein, skarn and porphyry systems (e.g., Skarpelis 2002; Melfos and Voudouris 2017). Carbonate-hosted replacement Pb-Zn-Ag mineralization is often spatially related to major detachment faults and occurs at Lavrion and on the islands of Syros and Sifnos (e.g., Bonsall et al. 2011; Berger et al. 2013). Skarn deposits occur on the islands of Serifos and Tinos (e.g., Fitros et al. 2017). Low- to high-sulfidation epithermal gold deposits and subvertical detachment- and fault-related base and precious metal vein mineralization are found on Milos, Tinos, Kythnos, Antiparos, and Mykonos islands (e.g., Alfieris et al. 2013; Kevrekidis et al. 2015; Menant et al. 2013; Tombros et al. 2007; 2015). Rapid uplift along the arc front has exposed former submarine hydrothermal systems on the island of Milos. Here, Pb-

Zn-Ba-(Mn-Ag-Au) low- to intermediate-sulfidation epithermal deposits occur primarily in Quaternary volcanic rocks in the western part of Milos (e.g., Kilias et al. 2001; Marschik et al. 2010; Alfieris et al. 2013).

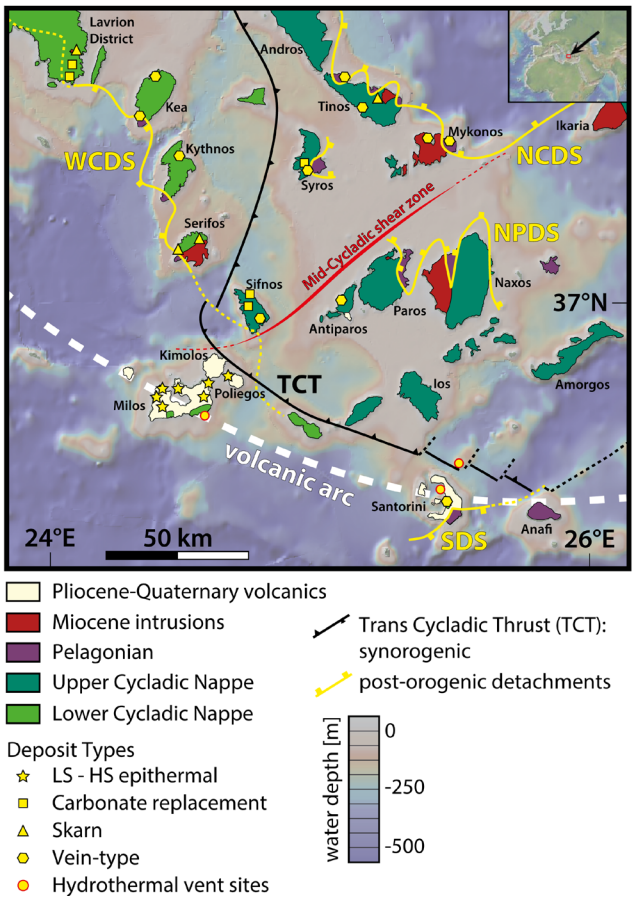

Figure 1. Simplified geological map of the Cyclades District (modified after Grasemann et al. 2018; Schneider et al. 2018). NCDS: North Cycladic Detachment System, WCDS: West Cycladic Detachment System, NPDS: Naxos-Paros Detachment System, SDS: Santorini Detachment System, LS-HS: Low- to high-sulfidation.

A common low-temperature mineral paragenesis is found in the different deposits in the western Cyclades with sphalerite, pyrite, galena and minor chalcopyrite and sulfosalts. In contrast, precious metal-rich vein-type deposits occur mainly in the northern and eastern Cyclades (e.g., Tinos, Mykonos, Antiparos) which are characterized by a galena-rich, chalcopyrite, pyrite and sulfosalt paragenesis with minor sphalerite and tellurides.

3 Trace elements in galena

To compare the geochemical signature of the mineral deposits in the Cyclades, galena mineral separates were prepared from 31 samples collected at twelve deposits on six islands (from north to south: Lavrion-9, Tinos-1, Mykonos-5, Serifos-3, Antiparos-2, Milos-11). Grain mounts were analyzed at the University of New Brunswick by LA-Q-ICP-MS (Agilent 7700x). Ablations were 30 seconds at 3 Hz with 30 seconds of washout and background collection. For each sample at least ten ablations on a minimum of seven grains were obtained, and a spot size of 45 µm was used. Reference standards include NIST610, MASS-1, GSE-1E, and Broken Hill Galena. Data reduction was performed using the MASS-1 sulfide reference material. In addition to the spot analyses, two trace element profiles were performed on galena from the Profitis Ilias drill core (P012, depth 317.8 m) on Milos and from the barite vein-type deposit on Mykonos (Panormos Bay). The profiles were performed with a 17 µm spot size and a speed of 5 µm/s.

Mineral deposits in the Cyclades District experienced only minor deformation and overprinting, which make galena a powerful indicator mineral of the ore-forming fluids and metal sources. The data support previously suggested potential of galena as host for a wide range of trace metals and metalloids (George et al. 2015), with the following trace elements detected in all of the analyzed galena: Ag, Sb, Cu, Cd, Tl, Bi. The most abundant trace elements are Ag and Sb, which are often correlated with each other (Fig. 2 and Fig. 3).

Table 1. Mean concentrations of trace elements obtained by spot analyses of galena of the different deposit types in the Cyclades mineral district. Trace elements are sorted from the most to the least abundant. Elements in bold have mean concentrations above 1000 ppm. Characteristic trace elements are highlighted in blue. n: number of analyzed samples, LCN: Lower Cycladic Nappe, UCN: Upper Cycladic Nappe, IS: Intermediate sulfidation, LS: Low sulfidation.

Location	Deposit name (n)	Deposit type	Host rock	Galena trace element concentration		
				major (>100 ppm)	minor (>1 ppm)	trace (<1 ppm)
Lavrion	Plaka (4)	Carbonate replacement	Marble, schist (LCN)	Ag, Sb	Sn, Cd, Mn, Cu	Tl, Bi, In, (Co, Te)
Lavrion	Kamariza (4)	Carbonate replacement	Marble, schist (LCN)	Ag, Sb	Cd, Sn, Cu, Bi, Te	Tl, In, (Co)
Lavrion	Sounio (1)	Carbonate replacement	Marble (LCN)	**Sb, Ag, Cu**	Cd, Sn	Tl, Bi, In
Tinos	Panormos Bay (1)	Quartz-veins	Marble (UCN)	Se, Ag, Sb, Te, Bi, Cd	Cu, Hg	Tl, Sn, In, Au
Mykonos	Cape Evros (2)	Barite-veins	Silica breccia, Miocene intrusion	Ag, Sb	Cd, Cu	Bi, In, Tl, Sn
Mykonos	Panormos Bay (3)	Barite-veins	Clastic sediments (Pelagonian)	**Sb, Ag,** As	Hg, Cu, Cd, Tl	(Bi, In, Sn)
Antiparos	Agios Georgios (2)	Quartz & barite-veins	Schist, marble (UCN)	Ag	Sb, Cd, Cu	Tl, Bi, Co, (In)
Serifos	Moutoulas (3)	Skarn	Schist, marble (LCN)	Ag, Sb	Bi, Cd, Mn, Cu	Tl, Sn, (Te, In)
Milos	Triades (3)	IS epithermal	Volcano-sedimentary (dacite)	Ag, Sb, Cu	Zn, Cd, As, Mn	Au, Tl, Bi, (Te)
Milos	Galana (4)	IS epithermal	Volcano-sedimentary (dacite)	Ag, Sb, Cu	Cd, Zn, Mn, Bi	Te, Tl, Au
Milos	Profitis Ilias (1)	IS epithermal	Rhyolite - rhyodacite	Te, Ag, Sb	Cd, Cu, Au, Mn	Bi, Tl, (Zn)
Milos	Kondaros (3)	LS-IS epithermal	Dacitic domes and lava flows	Ag, Sb	Cd, Cu	Tl, Bi

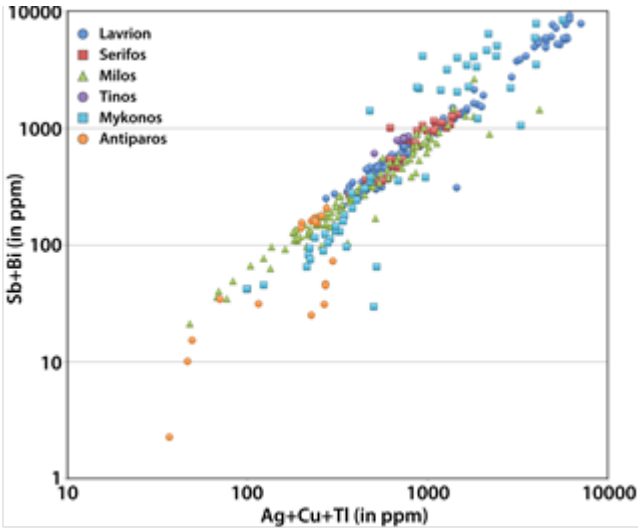

Figure 2. Major coupled substitution $(Ag,Cu,Tl)^{+}$ + $(Bi,Sb)^{3+}$ ↔ $2Pb^{2+}$ occurring in galena from the Cyclades mineral district. Concentrations are shown in ppm on a logarithmic scale.

The previously suggested coupled substitution of $(Ag,Cu,Tl)^{+}$ + $(Bi,Sb)^{3+}$ ↔ $2Pb^{2+}$ (George et al. 2015) is likely the main mechanism which incorporates Ag, Cu, Tl, Bi, and Sb into the crystal lattice (Fig. 2). Whereas Ag and Sb concentrations are greater than 100 ppm in galena from most deposits; Tl concentrations are <10 ppm. Mean concentrations for Bi are generally <10 ppm, except for Serifos and Tinos (Fig. 4). Copper concentrations vary significantly from 0.46 ppm to 5030 ppm between the deposits but also within a sample (Table 1).

Galena from the Cyclades has also low concentrations of Hg and Mn. Figure 3 shows the correlation between Ag, Sb, As, and Hg in galena from Mykonos (Panormos Bay). Silver and Sb show similar geochemical zoning, except for one rim of the crystal. The observed positive correlation between Ag and Sb in this profile is in contrast to described zonation patterns showing an inverse correlation of Sb and Ag, Bi, Se, Te, and Tl (George et al. 2015). A similar pattern is observed for Hg and As (Fig. 3), suggesting that pulses of Sb-Ag-Hg-As-rich fluids were encountered during crystal growth.

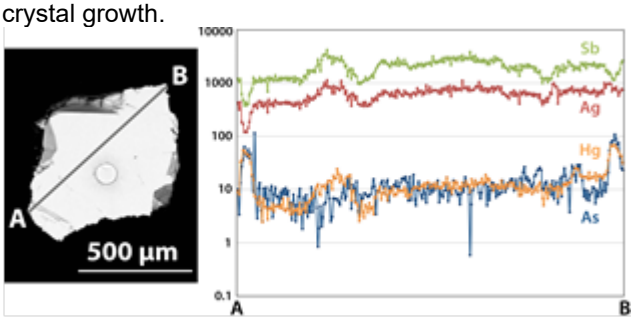

Figure 3. Profile through a galena from Mykonos (Panormos Bay). Sb, Ag, As, and Hg concentrations are displayed on a logarithmic scale in ppm.

4 Geochemistry of the Cyclades mineral district

Trace element concentrations in galena show systematic differences in the Cyclades mineral district and reflect the range of mineral deposit types (Table 1). Concentrations of Bi in galena are highly variable (Fig. 4). High Bi concentrations in galena from a skarn deposit on Serifos (Moutoulas) are in good agreement with the presence of native Bi reported by Fitros et al. (2017), and elevated Bi concentrations in galena for skarn deposits (George et al. 2015). High Bi concentrations were also detected in galena from the vein-type deposit on Tinos (Fig. 4, Panormos Bay), and together with high Se (average 805 ppm) and Te (average 312 ppm), the low standard deviations suggest these elements are present in solid solution. In general, galena from Tinos has the highest precious metal concentrations, with 707 ppm Ag and 0.04 ppm Au, and mean values of >300 ppm for Se, Sb, Te, and Bi and low mean concentrations of ≤1 ppm for Cu, Hg, Tl, In, and Sn. The abundance of precious metals in galena from Tinos is in good agreement with previously described Au-Ag-Te-rich mineral assemblages (Tombros et al. 2007), although the presence of Bi minerals was not noted. Trace elements in galena of the Panormos Bay vein-type deposit (Tinos) suggest higher mineralization temperatures than for most deposits in the Cyclades mineral district, and support an estimated minimum depth of 1 km and temperatures of 200–320 ºC (Tombros et al. 2007).

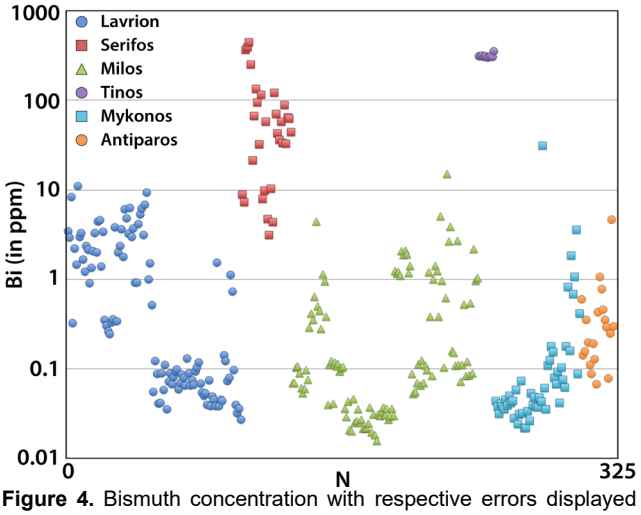

Figure 4. Bismuth concentration with respective errors displayed on a logarithmic scale in ppm for 340 different spot analyses in galena of the Cyclades mineral district. Concentrations are sorted from the lowest to the highest value for each analyzed sample.

On Mykonos galena has been analyzed from the polymetallic barite-vein deposits in Cape Evros and Panormos Bay, and generally low concentrations of trace elements have been detected for galena from Cape Evros (Table 1). Galena from Panormos Bay exhibits in contrast high mean concentrations in Ag (1700 ppm) and Sb (3000 ppm), as well as up to a few 100 ppm for As, Cu, and Hg (Fig. 3). High As and Hg

concentrations in galena of Panormos Bay (Mykonos) can be explained by an interaction of the ore-forming fluid with the surrounding clastic sedimentary host rock.

In contrast, galena from the vein-type deposit on Antiparos has the lowest analyzed concentrations of trace elements, with a mean Ag concentration of <250 ppm. This contrasts with microprobe analyses by Kevrekidis et al. (2015) who reported 0.17–2.90 wt.% Ag in galena from Antiparos.

Galena from most deposits has low concentrations of In and Sn, except for samples from the epithermal deposits on Milos. Indium concentrations in galena from the carbonate replacement deposits in the Lavrion District are generally below 1 ppm, but the mean concentrations of Sn are ~20 ppm. Galena from carbonate replacement deposits in Lavrion (Plaka area), skarn deposit on Serifos (Moutoulas) and epithermal deposits on Milos (Triades, Galana, Profitis Ilias) has low concentrations of Mn with a mean concentration of ~4 ppm in all samples. However, the low standard deviation for Mn in the profile through the drill core sample from Profitis Ilias suggests that this small amount of Mn may be present in solid solution in the galena. In addition, gold was detected in the galena samples from Milos (average 0.6 ppm at Triades, 0.05 ppm at Galana, and 5.5 ppm at Profitis Ilias), but have not been detected in samples from Kondaros, likely because of later silicification and metal leaching. Gold concentrations can reach up to 100 ppm in galena from the Profitis Ilias drill core sample, where Au likely occurs in Ag-Au-telluride inclusions, which was observed by a positive correlation between Au, Te and minor Ag in the profile trough a galena crystal. High Te concentrations (average 440 ppm), together with elevated Au concentrations suggest higher temperatures and pressures for mineralization at Profitis Ilias than at other epithermal deposits on Milos (Kilias et al. 2001).

5 Conclusion

Trace elements in galena from different deposits in the Cyclades mineral district are indicative of the deposit types, the conditions of mineralization, and the exposed host rocks. Galena from shallow crustal base metal deposits in the western Cyclades have similar concentrations of trace elements, whereas galena from vein-type deposits in the northern Cyclades have generally higher precious metal contents. Galena from Quaternary and recent mineralization along the active volcanic arc is also enriched in precious metals. These data highlight the potential of trace element geochemistry in galena as an indicator for different mineralization styles throughout the Cyclades mineral district, where only a few occurrences may be exposed.

Acknowledgements

Financial support for this work was provided by NSERC Discovery grants to MDH and DAS and a SEGCF student research grant to SCW. We thank Stephanos Kilias for his assistance in the field and the provided drill core sample of Milos. Hercules Katsaros and Nikos Leloudas are thanked for their assistance with underground sampling in Lavrion. We are grateful to Brandon Boucher and Christopher McFarlane from UNB for their help with LA-Q-ICP-MS analyses and data reduction.

References

Alfieris D, Voudouris P, Spry PG (2013) Shallow submarine epithermal Pb-Zn-Cu-Au-Ag-Te mineralization on western Milos Island, Aegean Volcanic Arc, Greece: Mineralogical, geological and geochemical constraints. Ore Geol Rev 53:159–180.

Berger A, Schneider DA, Grasemann B, Stockli D (2013) Footwall mineralization during Late Miocene extension along the West Cycladic Detachment System, Lavrion, Greece. Terra Nova 25:181–191.

Bonsall TA, Spry PG, Voudouris PC, Tombros S, St. Seymour K, Melfos V (2011) The geochemistry of carbonate-replacement Pb-Zn-Ag mineralization in the Lavrion District, Attica, Greece: Fluid inclusion, stable isotope, and rare earth element studies. Econ Geol 106:619–651.

Fitros M, Tombros SF, Williams-Jones AE, Tsikouras B, Koutsopoulou E, Hatzipanagiotou, K (2017) Physicochemical controls on bismuth mineralization: An example from Moutoulas, Serifos Island, Cyclades, Greece. Am Mineral 102:1622–1631.

Grasemann B, Huet B, Schneider DA, Rice AHN, Lemonnier N, Tschegg C (2018) Miocene postorogenic extension of the Eocene synorogenic imbricated Hellenic subduction channel: New constraints from Milos (Cyclades, Greece). Geol Soc Am Bull 130:238–262

George L, Cook NJ, Ciobanu CL, Wade BP (2015) Trace and minor elements in galena: A reconnaissance LA-ICP-MS study. Am Mineral 100:548–569.

Kevrekidis E, St. Seymour K, Tombros S, Zhai D, Liu J, Zouzias D (2015) The Agios Georgios argentiferous galena deposit on Antiparos island, Cyclades, Hellas and its relationship to the Paros leucogranite. Neues Jahrb Mineral 192:239–261.

Kilias SP, Naden J, Cheliotis I, Shepherd TJ, Constandinidou H, Crossing J, Simos I (2001) Epithermal gold mineralisation in the active Aegean Volcanic Arc: the Profitis Ilias deposit, Milos Island, Greece. Miner Deposita 36:32–44.

Marschik R, Bauer T, Hensler AS, Skarpelis N, Hölzl S (2010) Isotope geochemistry of the Pb-Zn-Ba(-Ag-Au) mineralization at Triades-Galana, Milos Island, Greece. Resour Geol 60:335–347.

Menant A, Jolivet L, Augier R, Skarpelis N (2013) The North Cycladic Detachment System and associated mineralization, Mykonos, Greece: Insights on the evolution of the Aegean domain. Tectonics 32:433–452.

Menant A, Jolivet L, Tuduri J, Loiselet C, Bertrand G, Guillou-Frottier L (2018) 3D subduction dynamics: A first-order parameter of the transition from copper- to gold-rich deposits in the eastern Mediterranean region. Ore Geol Rev 94:118–135.

Melfos V, Voudouris P (2017) Cenozoic metallogeny of Greece and potential for precious, critical and rare metals exploration. Ore Geol Rev 89:1030–1057.

Schneider DA, Grasemann B, Lion A, Soukis K, Draganits E (2018) Geodynamic significance of the Santorini Detachment System (Cyclades, Greece). Terra Nova 30:414–422.

Skarpelis N (2002) Geodynamics and evolution of the Miocene mineralisation in the Cycladic-Pelagonian belt, Hellenides. Bull Geol Soc Greece 34: 2191–2206.

Tombros S, St. Seymour K, Williams-Jones AE, Spry PG (2007) The Genesis of epithermal Au-Ag-Te mineralization, Panormos Bay, Tinos Island, Cyclades, Greece. Econ Geol 102:1269–1294.

Tombros SF, St. Seymour K, Williams-Jones AE, Zhai D, Liu J (2015) Origin of a barite-sulfide ore deposit in the Mykonos intrusion, Cyclades: Trace element, isotopic, fluid inclusion and Raman spectroscopy evidence. Ore Geol Rev 67:139–157.

Relations between matrix type and style of mineralization in sandstone ore, Nowa Sól Cu-Ag deposit, SW Poland

Tomasz Bieńko
Miedzi Copper Corp.

Abstract. Five types of cement have been recognized within white sandstones (the BS unit, Weissliegend sandstone) of the Nowa Sól deposit – anhydrite matrix, sulfide matrix, carbonate matrix, clay minerals matrix and silica matrix. A downward cement composition shift from anhydrite and sulfide to clay is visible in Weissliegend sandstones form the Nowa Sól deposit. The pervasiveness of alteration of detrial grains (mainly feldspar, detrial rutile and titanite) increases upwards, reaching maximum range beneath the base of the Kupferschiefer, regardless of its thickness. The uppermost part of the white sandstones contain two types of ore – massive sulfide cement and copper sulfides replacing feldspars, which are associated with ubiquitous anhydrite matrix. Chalcocite predominates within the sandstone ore, but it may be accompanied by other Cu-S-type sulfides, pyrite, galena, sphalerite and Ag-phases at the top of the BS unit, where ore mineral composition sharply increases.

1 Introduction

Sediment-hosted Cu-Ag deposits have been documented on the Fore-Sudetic Monocline and North Sudetic Through, Poland. Polymetallic mineralization is developed within sedimentary rocks ranging from terrestrial red beds to marine Weissliegend sandstones, shales, carbonates and anhydrites (Pieczonka et al., 2007). Historically, the richest copper mineralization was recognized within copper-bearing, organic rich shale, known as the Kupferschiefer. Thus, traditionally, sediment-hosted deposits in Europe are called Kupferschiefer-type. However, recently most of the mining operations on the Fore-Sudetic Monocline have focussed on three types of ore – carbonate (the Ca1 and Ca0 units), shale (the T1 unit) and sandstone (the BS unit). As the mining goes deeper, the contribution of the sandstone ore to the copper production in Poland increases. Sandstone ore in the recently discovered Nowa Sól deposit is usually chalcocite-dominated and is restricted to top of the BS unit.

2 Sediment-hosted Cu-Ag deposits on the Fore-Sudetic Monocline

2.1 Geology

The European Permian basin extends from central Poland to eastern coast of England. It is filled by a sequence of terrestrial – red sandstones (the Rotliegend Formation) – and marine sedimentary rocks – Weissliegend sandstones, shales, carbonates and evaporates (the Zechstein Formation) (Borg et al., 2012).

The Polish Lower Permian formation is composed of a thick sequence of terrestrial sediments intruded by intermediate volcanic rocks. The Zechstein Formation in Poland is developed in the form of 4 major evaporative cycles (cyclothemes; PZ1 Werra, PZ2 Strassfurt, PZ3 Leine and PZ4 Aller). The oldest cyclotheme, Werra, was deposited directly on the Rotliegend red beds or white sandstones, which are the product of marine re-deposition of terrestrial sandstones. Sediments of the Werra cycle are developed upward as copper-bearing shale (T1), which in some parts of the basin is underlain by the basal limestone (Ca0), the Zechstein limestone (Ca1), the lower anhydrite (A1d), the oldest salt (Na1) and the upper anhydrite (A1g) (Oszczepalski, 1999). The contact between clastic, mainly aeolian, sediments and reduced marine strata is basin-wide and concordant. The Zechstein sequence is covered by Triassic (terrestrial Lower and Middle Bundsandstein, marine Upper Bundsandstein, Muschelkalk and Keuper) and, in eastern part of Fore-Sudetic Monocline, Jurassic sediments of varying thickness. The uppermost part of the Fore-Sudetic Monocline profile consist of Cenozoic sands, silts, coals and clays (Fig. 3).

2.2 Types of ore and metal zonation

The north-eastward dipping Fore-Sudetic Monocline is a region of great mineral potential. The base of the Zechstein Formation, which in this area hosts 4 already documented tier 1 stratiform Cu-Ag deposits, is of the main exploration interest. Mineralization in the Polish Kupferschiefer deposits is not restricted to the copper-bearing shale. The position of the ore series is often much wider. Copper sulfides are observed in the upper part of Weissliegend sandstones, basal limestone, copper-bearing shale, Zechstein limestone and in some places also within the lower anhydrite (Pieczonka et al., 2007).

Sediment-hosted deposits located on the Fore-Sudetic Monocline exhibit metal zonation, which is highlighted by the distribution of sulfides within ore series (Oszczepalski, 1999; Alderton et al., 2016). Five zones of different mineralogical and geochemical features have been recognized within all copper deposits in Poland: (1) oxidized copper-depleted hematite-bearing zone (Rote Fäule), (2) Au-PGE-enriched transitional zone, (3) copper-bearing zone, (4) lead-zinc zone and (5) pyrite zone. This continuous transition from hematitic sediments to Cu-Ag-Pb-Zn-mineralized rocks is both vertical and horizontal. High-

grade copper ores are developed in the vicinity of large oxidized fields, where reduced facies hosting copper mineralization contact with hematite-dominated sediments (Oszczepalski, 1999; Borg et al., 2012). The mineral distribution and thickness of the ore zone depends on the position of a transgressive, oxidizing Rote Fäule facies and the composition of the lower Zechstein sediments.

The western part of the Fore-Sudetic Monocline is considered prospective for documenting high grade copper mineralization within the base of the Zechstein at depths exceeding 2000 meters (Speczik, 1995; Oszczepalski et al., 2016). This was proved by the extensive exploration program led by Miedzi Copper Corp. (Fig. 1), preceded by oil and gas industry drilling.

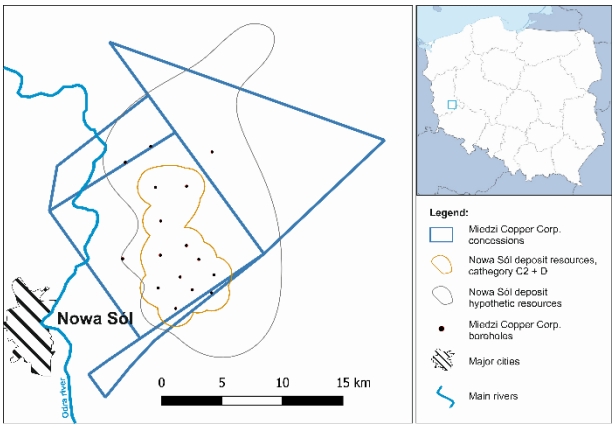

Figure 1. Location of the Nowa Sól deposit, Lubuskie voivodeship, SW Poland

3 Types of ores within the Nowa Sól deposit

An upward transition from white sandstones to evaporites marks the Zechstein sea transgression and a few minor transgressive-regressive cycles, that can be recognized within the Zechstein limestone. White sandstones are interpreted as upper parts of sand dunes that have been flooded by the Zechstein sea. This formerly aeolian sediment was deposited in an arid environment, then rapidly became the seafloor of the Zechstein sea (reducing environment). The Weissliegend unit is not always developed within the Lower Zechstein profile – in some places copper-bearing shale may be deposited directly on the terrestrial red beds, which are sometimes white, due to de-colorization processes.

Drilling program results show that different styles of mineralization can be recognized within the Nowa Sól deposit (Fig. 1). Along the rim of the Zielona Góra Oxidized Field, carbonate ores predominate, while northward, where the base of the Zechstein Formation dips, shale and sandstone ores play more important role. Copper-bearing shale, basal limestone and Zechstein carbonate host mineralization of different styles. Limestone ore is usually disseminated, but may be accompanied by coarse-grained aggregates and sulfide lenses. Shale ore is almost always of the highest grade. Mineralization of the Kupferschiefer unit is usually disseminated, but contains numerous lenses and veinlets parallel to lamination surfaces. Sandstone mineralization is usually disseminated and it is developed in the form of copper sulfides cement. On the top of Lower Permian unit, where sandstones contact with the copper-bearing shale, copper mineralization within sandstone may be massive.

4 Results

4.1 Materials and methods

This study is based on examination of thin section petrographic samples from deep exploration boreholes Its aim is to recognize the main types of sandstone ore within Nowa Sól deposit. All studied mineralized cores have been reexamined and profiled in order to describe CS/BS, BS/T1 and BS/Ca0 contact characteristics. Moreover, macro trends in mineralization style within white sandstone have been studied. All petrographic samples have been examined under polarized light optical Nikon Eclipse E-600 microscope and Zeiss Sigma Field Emission Scanning Electron Microscope.

4.2 White sandstones petrography

White sandstones of the Nowa Sól deposit are gray and light gray, fine-grained and subrounded. The cement is usually blocky and syntaxial. Porosity is always low. Rocks of this unit can contain thin argillaceous laminae, which are usually organic rich. Beneath the uppermost part of the BS unit, sandstones are composed of fine and coarse-grained sand interbeds. Disseminated copper mineralization can often be seen macroscopically. Footwall Weissliegend sandstones are medium and coarse-grained, often exhibit indistinct cross bedding and can be patched with red-colored cement. Thickness of white sandstones does not exceed 10 meters – copper mineralization is restricted only to upper few meters of that unit. The lower limit of sandstone ore is marked by the hematitic zone of oxidizing Rote Fäule.

Quartz is a major detrital mineral in BS sandstones. At the top of the BS unit well-sorted fine and very fine rounded quartz grains are present. Downward, poorly sorted subangular grains start to predominate. Potassium feldspar is the second most abundant detrital phase in the BS unit. It is usually subhedral or anhedral, coarse-grained and exhibits disequilibrium textures – feldspar grains are corroded, contain thin inclusions filled with copper sulfides, galena and anhydrite. While overall rock alteration is usually selectively pervasive or non-pervasive, the alteration of feldspars is usually pervasive (Fig. 2B). Alteration of feldspar to clay minerals is characteristic for the top of the Weissliegend unit. Biotite, zircon, apatite, garnet, ilmenite and plagioclase are present in minor amounts. Ilmenite from white sandstones shows partial to complete conversion into leucoxene-rutile and leucoxene. In the upper part of mineralized interval, conversion of ilmenite into

leucoxene is complete, while in the distal parts of the sandstone ore ilmenite is partly replaced by the aggregate of rutile and leucoxene (Fig. 2C). In high grade copper zones leucoxene is associated with aggregates of chalcocite grains, whereas in lower parts of mineralized intervals, a leucoxene-rutile association contain pyrite intergrowths.

4.3 Styles of mineralization

Disseminated copper mineralization predominates in the Nowa Sól deposit sandstones. The main ore mineral is chalcocite with minor digenite and covellite. Chalcocite is the major constituent of sulfide cement. It can form large, mono-mineral aggregates, filling voids between quartz grains. Sometimes it is accompanied by framboidal pyrite (Fig. 2A). In the uppermost parts of BS sandstones, chalcocite replaces feldspars, forming lenses and small intergrowths within these mineral phases.

Digenite and covellite are associated with pyrite, in which they are developed in form of thin intercalations. These concentric, rosette-shaped pyrite-covellite-digenite aggregates are ubiquitous in the upper parts of white sandstones, which are enriched in organic matter and contain ubiquitous framboidal pyrite. In the lower part of white sandstones, near the base of the BS unit, pyrite forms independent aggregates, which exhibit similar shape, but lack Cu-S sulfides. Pyrite is the major non-copper sulfide which is recognized throughout the whole profile of white sandstones. Cu-S sulfides are rarely associated with Cu-Fe-S sulfides, mainly chalcopyrite and bornite. Within Nowa Sól deposit such mineral paragenesis is uncommon, contrary to deep Lower Zechstein profiles from the northern part of Fore-Sudetic Monocline.

In boreholes which intersected high-grade mineralization both in Weissliegend sandstones and copper-bearing shale, sandstone ore consists of a range of mineral paragenesis. Chalcocite is the main Cu-S phase. Locally it may form sulfide cement. It is usually associated with minor digenite, covellite and pyrite. Large chalcocite aggregates form intergrowths with Ag-phases and pink bornite. Galena and sphalerite are commonly present. Feldspars may be completely replaced by chalcocite in massive copper mineralization within Weissliegend sandstones.

In the places where copper-bearing shale is present, sandstone ore may be developed in form of rhythmic sulfide bands. Each band is few centimeters wide and its upper limit is blurred, composed of disseminated copper sulfides, while its lower part is sharply-limited. One mineralized interval may be composed of few rhythmic sulfide bands composed of chalcocite.

4.4 Types of white sandstones and their contribution to the style of mineralization

Five types of white sandstones from the Nowa Sól deposit can be recognized: anhydrite-cemented, carbonate-cemented, sulfide-cemented, clay-cemented and silica-cemented. Anhydrite and carbonate cements are the most abundant types (Fig. 3). The former predominates at the uppermost part of the BS unit, while the latter forms matrix beneath the sulfate-dominated zone. Sulfate matrix is present in sandstones regardless of thickness of the copper-bearing shale.

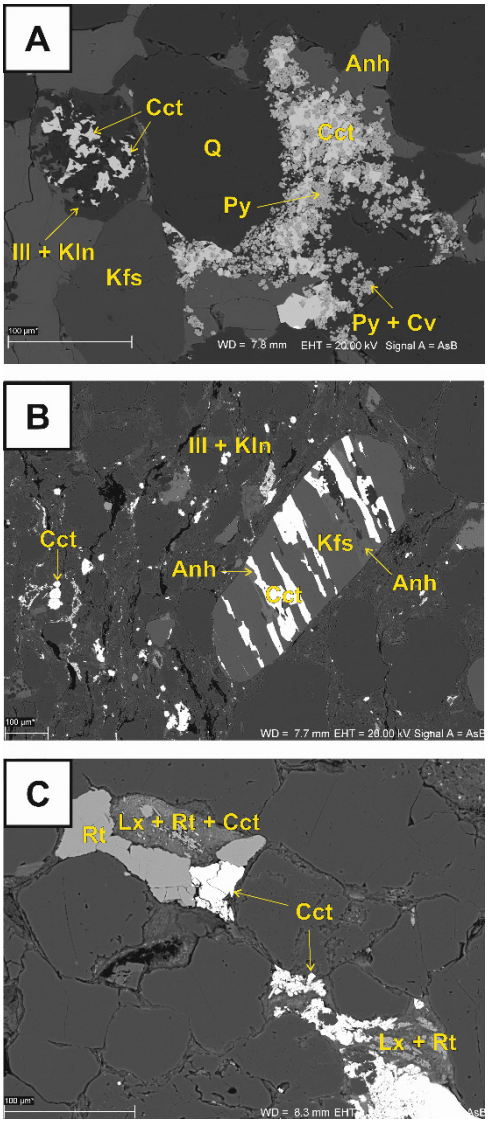

Figure 2. (A) Chalcocite (Cct) mineralization – sulfide cement associated with remnants of framboidal pyrite (Py) and pyrite-covellite-digenite (Py + Cv) rosette-like integrowths. Upper part of the sandstone ore; (B) Replacement of potassium feldspar (Kfs) detrital grain by chalcocite (Cct) and anhydrite (Anh). Dissaminated chalcocite (Cct) mineralization within illite-kaolinite (Ill + Kln) matrix. Upper part of the sandstone ore; (C) Rutile (Rt) and relict leucoxene (Lx + Rt) associated with very fine-grained Cu-S sulfides (Cct). Distal part of the sandstone ore. SEM images.

Sulfide-cemented sandstones, occur only in the areas of thick T1 unit and are composed mainly of chalcocite. Clay cement is well developed at the lower part of white sandstones unit, but is abundant in subordinate amounts along the whole BS profile. Silica matrix is present only in the most pervasively altered parts of the BS, where sulfides are the main constituent of the

cement.

In the uppermost part of the Weissliegend unit, which is usually copper-bearing, anhydrite predominates over carbonate, illite-kaolinite cement and silica. Mineralized sulfate-cemented sandstones exhibit pervasive feldspar replacement. Chalcocite is the major sulfide phase replacing potassium feldspar and it is usually associated with anhydrite. Individual chalcocite aggregates exhibit the crystal habit of feldspar. Thin lenses within feldspar grains are filled with chalcocite as well as anhydrite. Corroded feldspar grains are typically rimmed by anhydrite in which chalcocite and minor digenite are disseminated. Feldspars are also pervasively replaced by the clay minerals – mainly kaolinite. Within aggregates of kaolinite and illite anhydrite lenses are being reported. Quartz grains does not exhibit disequilibrium textures, but may be rimed by silica cement in high grade copper intervals.

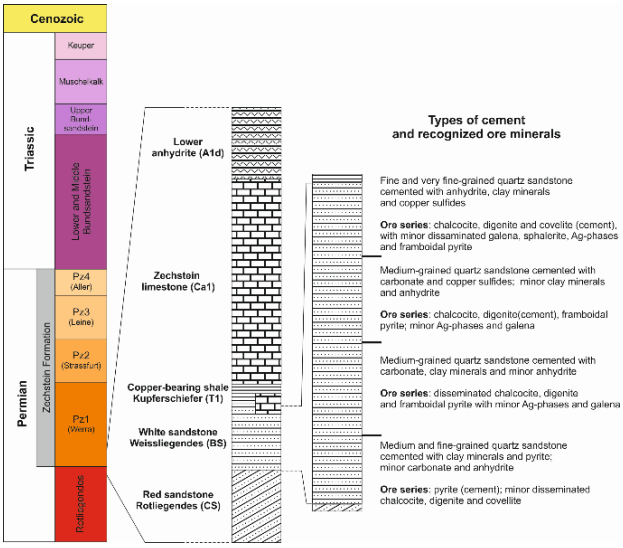

Figure 3. Profile of the lower Zechstein copper-silver ore series with particular reference to the white sandstone of Nowa Sól deposit (the BS unit).

Fine grained laminations are commonly reported within coarse-grained sandstone. The style of the copper mineralization is usually dependent on variability of grain size and its spatial characteristics (continuous lenses of fine-grained, sub angular material). Thus, disseminated copper ore exhibit regular patterns in the micro scale. In the coarse-grained zone sulfide phases form small aggregates (<100 μm) which are usually disseminated, while copper mineralization within fine-grained lenses is characterized by more massive habit.

5 Summary

The sandstone ore within the Nowa Sól deposit is almost mono-mineralic – composed almost entirely of chalcocite. However, style of mineralization and grade of copper ore varies throughout the profile of white sandstones. In areas, where Rote Fäule is developed a few meters beneath the T1 unit, copper mineralization is usually disseminated or may be represented by rhythmic sulfide bands. In regions where the top of Rote Fäule is situated tens of centimeters beneath the Kupferschifer, sandstone is chalcocite-cemented and mineralization is massive. The variability of grain size seems to be more important factor determining style of mineralization than the type of cement. However, the fact that anhydrite lenses and intergrowths within potassium feldspars and ilmenite relicts have been documented in all examined samples from the upper BS unit, suggests that the role of cement composition in the formation of ore should be taken into account. Leucoxene formation and the pervasiveness of ilmenite replacement suggests different intensity of mineralizing event (either in terms of time of residence of mineralizing fluids and its thermodynamic properties) at different parts of the BS unit. The pervasive replacement of feldspar and ilmenite by copper sulfides in the uppermost 20 centimeters of white sandstones may be strictly correlated with the part of the BS unit, which has been under the greatest influence of the Zechstein sea reducing conditions.

The major conclusions are: (1) the upper part of Weissliegend was deposited in reducing environment (framboidal pyrite, which is commonly replaced by copper sulfides); (2) organic-rich millimeter-wide clayey interbeds may have acted as first red-ox barrier for the ascending mineralizing fluid (Speczik, and Püttmann, 1987; Speczik, 1994); (3) anhydrite, which is present as a cementing factor, might have been a substrate of thermodynamic sulfate reduction (TSR), that may have generated sufficient amounts of H_2S to promote base metals precipitation (Machel, 1998) and (4) layers of variable grain size within coarse-grained sandstone may have acted as permeable channels for both ascending and descending fluids.

References

Alderton D.H.M., Selby D., Kucha H., Blundell D.J., 2016: A multistage origin for Kupferschiefer mineralization. Ore Geol. Rev. 79:535-543.

Borg G., Piestrzyński A., Bachmann G.H., Püttmann W., Walther S., Fiedler M., 2012: An Overviw of the European Kupferschiefer deposits. Soc. Of Econ. Geol. Special Pub. 16:455-486.

Machel H.G., 1998: Bacterial and thermochemical sulfate reduction in diagenetic settings – old and new insights. Sedimentary Geol. 140:143-175.

Oszczepalski S., 1999: Origin of the Kupferschifer polymetallic mineralization in Poland. Mineral. Deposita 34:599-613.

Oszczepalski S., Speczik S., Chmielewski A., Małecka K., 2016: Perspective copper resource of Poland. Min. Res. Management 32:5-30.

Pieczonka J., Piestrzyński A., Lenik P., Czerw H., 2017: Distribution of ore minerals in the copper deposit, Fore-Sudetic Monocline, SW Poland. Polish Geol. Inst. Bulletin 423:95-108.

Speczik S., 1994: Kupferschiefer mineralization in the light of organic chemistry of coal petrology studies. Geol. Quart. 38:639-650.

Speczik S., 1995: The Kupferschiefer mineralization of Central Europe: New aspects and major areas of future research. Ore Geol. Rev. 9:411-426.

Speczik S., Püttmann W., 1987: Origin of the Kupferschiefer mineralization as suggested by coal petrology and organic geochemical studies. Acta Geol. Pol. 37:167-187.

Proposed re-Interpretation of hydrothermal alteration, mineralization and host-rock oxidation to form the Keweenaw native copper lodes, Northern Michigan, U.S.A.

Alex C. Brown
Pierrefonds, Quebec, Canada

Abstract. Native copper deposition in the Keweenaw district, northern Michigan, is often said to have been accompanied by the destruction of pre-ore hematite. This contribution proposes instead that the pervasive deep-red pigmenting hematite of the permeable host sediments (and volcanic units) was deposited *after* native copper deposition and that native copper behaved as a chemical reductant which resisted the deposition of post-ore hematite in the immediate vicinity of native copper. Previous work proposed that native copper was deposited in the Keweenaw rift basin from moderately oxidized hybrid brines formed by mixing of downward infiltrating meteoric water and deep metamorphogenic water. The deposition of late hematite may have occurred as the result of late subsurface circulations of oxygen-rich, highland recharge-driven meteoric water.

1 Introduction

Early descriptions of the native copper ores of northern Michigan have stated repeatedly that widespread deeply reddish host rocks were hydrothermally bleached to salmon-red colors in the immediate vicinity of native copper (e.g., Butler and Burbank 1929; Cornwall 1956; White 1968; Weege and Pollach 1972). As such, the Keweenaw host-rocks would have attained their deep-red colorings before copper deposition. This communication notes however that, in areas of low-grade disseminated native copper mineralization within fine-grained clastic sediments, pervasive hematitic reddening appears to have invaded and enclosed *previously native copper-mineralized* sediment, and that deep hematitic reddening is absent in aureoles immediately surrounding isolated disseminated grains of native copper. Native copper behaved as a chemical reductant, equivalent to organic matter in redbeds containing reduction spots.

2 Prior observations and interpretations

The sequence of Keweenaw hydrothermal alterations, mineralization and reddening may be analogous to that found in redbeds showing centimetric-scale reduction spots: e.g., those of the Carboniferous redbeds of eastern Canada (Poll and Sutherland 1976; Brown 1976, 1977) (Figs. 1 and 2) and in the fluvial Abo Formation, New Mexico (Bensing et al. 2005). The reduction spots in the Abo Formation have less total iron compared to enclosing reddened (hematitic) fine-grained clastic sediment. Petrographic and SEM analyses indicate that the reduc-tion spots have never been reddened. Similarly, the

Figure 1. Carboniferous redbeds of Dorchester Cape district, New Brunswick, Canada, showing abundant centimetric-scale reduction spots with dark-greyish cores centered on organic matter. See Figure 2 for closer details.

Figure 2. Close view of greyish reduction spots shown in redbeds of Figure 1 (tip of geologic hammer for scale). Cores of reduction spots contain organic matter (wood debris) and are the sites of base-metal sulfide mineralization (especially copper sulfides, partially oxidized to malachite). See text for further explanations.

reduction spots of Carboniferous redbeds in Maritime Canada are typically circular or elliptical and are commonly centered on remnants of organic matter (wood fragments) which may be mineralized with pyrite, base-metal sulfides and other metals (e.g., Ag, U, V) (Brown 1976, 1977; Poll and Sutherland 1976). Organic

matter observed at the centers of reduction spots is interpreted to have maintained surrounding aureoles of reduction where pigmenting hematite could never have been chemically stable, as proposed by Bensing et al. (2005).

3 Observations on Keweenaw native copper

Aureole effects similar to those found in redbeds are recognized in the clastic sediments hosting native copper in the Keweenaw district of northern Michigan, especially where concentrations of native copper are low in fine-grained sediments (Fig. 3); high-grade native copper mineralization in coarse-grained host sediments is more difficult to interpret because massive amounts of native copper tend to mask hydrothermal alterations.

Figure 3 exhibits an apparent finger of "bleached" fine-grained clastic sediment beneath massive native copper in overlying coarse-grained sediment. The "bleached finger" is defined by rusty-red ferric hydroxide alteration immediately surrounding disseminations of native copper, the whole otherwise enclosed by pervasively deeply reddened sediment. In fact, each grain of native copper within the finger defines the center of a hematite-poor "knuckle" of hematite-poor sediment along that finger, separated from surrounding hematite-rich sediment by an approximately ½ cm aureole of unmineralized ferric hydroxide-altered fine-grained sediment.

Earlier reports (noted above) have attributed the so-called bleaching of pre-ore hematite to hot cupriferous hydrothermal solutions which altered the host sandstone-conglomerates during the deposition of native copper; hematite was destroyed by the ore-forming solution. That interpretation has met with skepticism because the cuprous chloride-bearing ore brines should have been *mildly oxidizing* in order to have carried significant amounts of copper (Brown 1971, 2006; Rose 1976, 1989); i.e., the ore solution should not have been hematite-destructive during native copper deposition.

4 Interpretation of processes and timing of Keweenaw native copper deposition

Most modern interpretations of the genesis of native copper lodes in the Keweenaw district justifiably assume that copper was leached from deep, hot, down-dip extensions of thick rift-filling mafic volcanics and interbedded sandstone-conglomerate host units during or after their northward tilt as a result of Grenvillian compression. Metamorphogenic fluids (Stoiber and Davidson 1959; Jolly 1974; Bornhorst and Mathur 2017), plausibly combined with deep highland-driven meteoric water (Brown 2006, 2008, 2018), ascended along permeable strata (e.g., amygdaloidal flow-top breccias and sandstone-conglomerates) to mineralize cooler, up-dip portions of those same permeable aquifers.

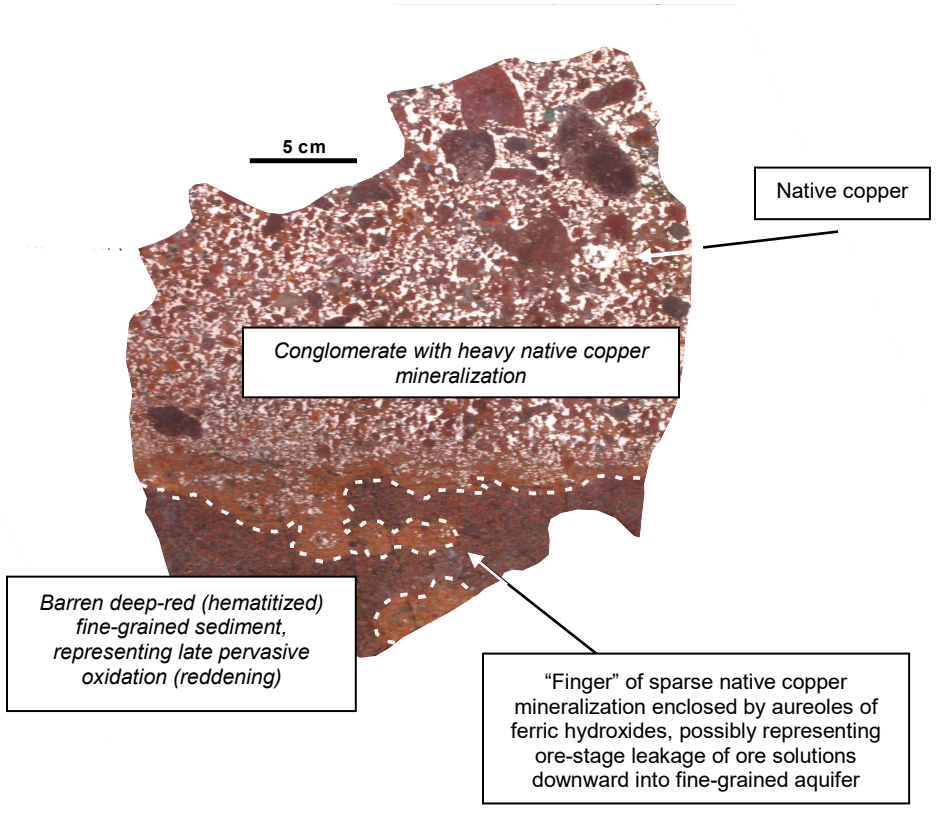

Figure 3. A cut and epoxy-sprayed slab of high-grade native copper ore from the Calumet and Hecla Conglomerate, Centennial no. 6 mine, Keweenaw copper district, northern Michigan. Native copper (whitish pink) is abundant in the conglomeratic portion (upper two-thirds) of the sample. In the underlying finer clastic portion of the sample, sparse grains of native copper are enclosed by hydrothermally "bleached" alteration. The white dashed line (added) separates all native copper mineralized sediment from barren, heavily hematitized, deep-red sediment in the lower

portion of the sample. See text for further explanations.

The addition of highland-driven meteoric water to form a hybrid ore solution was proposed principally to explain the transport of copper as chloride complexes in mildly oxidized brines. Otherwise, metamorphogenic fluids generated from mafic source rock should have had low redox levels defined by the ferrous-ferric stability limit, at which the maximum solubility of copper would have been too low to have formed an ore-forming cupriferous solution (Brown 2006).

5 Conclusion

The recommended explanation for the observed native copper mineralization and associated alterations is: (1) deep rift-basin leaching of copper by hybrid evolved meteoric/metamorphogenic waters; (2) ascent of the hot ore solution along Keweenaw aquifers and deposition of native copper lodes at cooler levels (between approx. 280 and 180ºC; Livnat et al. 1983), accompanied by partial destruction of mafic minerals and deposition of ferric hydroxides (Walker 1989); and (3) pervasive deep-red oxidation of Keweenaw aquifers by late oxygen-rich highland-driven meteoric waters.

Acknowledgements

The author has benefitted from a career of supported research and 15 more years of retirement during which he has enjoyed re-considering the genesis of sediment-hosted copper mineralization. He also wishes to thank Dave Broughton for bringing the Bensing et al. paper to his attention.

References

Bensing JP, Mozley PS, Dunbar NW (2005) Importance of clay in iron transport and sediment reddening: evidence from reduction features of the Abo Formation, New Mexico, U.S.A. J Sedimentary Research 75:562–571

Bornhorst TJ, Mathur R (2017) Copper isotope constraints on the genesis of the Keweenaw Peninsula native copper district, Michigan, USA. Minerals 7:185 doi.org/10.3390/min7100185

Brown AC (1971) Zoning in the White Pine copper deposit, Ontonogan County, Michigan. Econ Geology 66:543–573

Brown AC (1976) A study of stratiform copper deposits in Carboniferous strata of New Brunswick and Nova Scotia. Geol Surv Canada, Paper 75-1, Part A:598–600

Brown AC (1977) A study of stratiform copper deposits in Middle Carboniferous strata of New Brunswick and Nova Scotia. Geol Surv Canada, Paper 76-1A:110

Brown AC (2006) Genesis of native copper lodes in the Keweenaw district, northern Michigan: a hybrid evolved meteoric and metamorphogenic model. Econ Geology 101:1437–1444

Brown AC (2008) District-scale concentration of native copper lodes from a tectonically induced thermal plume of ore fluids on the Keweenaw Peninsula, northern Michigan. Econ Geology 103:1691–1694

Brown AC (2018) Copper isotope constraints on the genesis of the Keweenaw Peninsula native copper district, Michigan, USA: A comment. Minerals 8:506 doi.org/10.3390/min8110506

Butler BS, Burbank WS (1929) The copper deposits of Michigan. US Geol Surv, Prof Paper 144, 238 p

Cornwall HR (1956) A summary of ideas on the origin of native copper deposits. Econ Geology 51:615–631

Jolly WT (1974) Behavior of Cu, Zn, and Ni during prehnite-pumpellyite rank metamorphism of the Keweenawan basalts, Northern Michigan. Econ Geology 69:1118–1125

Livnat A, Kelly WC, Essene EJ, Rye RO (1983) P-T-X conditions of sub-greenschist burial metamorphism and copper mineralization, Keweenaw Peninsula, northern Michigan. Geol Soc America, Abstracts 15:629

Poll HW van de, Sutherland JR (1976) Cupriferous reduction spheres in upper Mississippian red beds of the Hopewell Group at Dorchester Cape, New Brunswick. Can Jour Earth Sci, 13:781–789

Rose AW (1976) The effect of cuprous chloride complexes in the origin of red-bed copper and related deposits. Econ Geology 71:1036–1048

Rose AW (1989) Mobility of copper and other heavy metals in sedimentary environments. Geol Assoc Canada, Spec Paper 36:97–110

Stoiber RE, Davidson ES (1959) Amygdule mineral zoning in the Portage Lake Lava Series, Michigan copper district; Part I, Part II. Econ Geology 54:1250–1460, 54:1444–1460

Walker TR (1989) Application of diagenetic alterations in redbeds to the origin of copper in stratiform copper deposits. Geol Assoc Canada, Spec Paper 36:85–96

Weege RJ, Polloch JP (1972) The geology of two new mines in the native copper district of Michigan. Econ Geology 67:622–633

White WS (1968) The native-copper deposits of northern Michigan, *in* Ridge JD, ed., Ore deposits of the United States, 1933–1967 (Graton-Sales Volume 1). American Inst Min Metall & Petrol Eng 303–326

Dairi: an example of Zn-Pb-Ag sediment-hosted deposit from Indonesia

Tomy Alvin Rivai, Kotaro Yonezu, Thomas Tindell, Akira Imai, Koichiro Watanabe
Department of Earth Resources Engineering, Kyushu University, Japan

Syafrizal
Department of Mining Engineering, Bandung Institute of Technology, Indonesia

Adrian J Boyce
Scottish Universities Environmental Research Centre, UK

Abstract. The Dairi Zn-Pb-Ag deposit is the first SEDEX deposit discovered in Indonesia thus understanding its genesis is key to future SEDEX exploration in Sumatra. Orebodies are hosted in Lower Carboniferous black shales-siltstones (stratiform orebodies) and dolostones (discordant orebodies) representing sag-phase sequence in the Dairi basin. The discordant orebodies are lower in stratigraphy and are conceptually understood as feeder zones to the overlying stratiform orebodies. The reduced and acid ore-forming fluid was moderately saline and warm (18-25 wt% NaCl eq., ~170°C) before being diluted by seawater (3 wt% NaCl eq., ~3°C). A geochemical halo around the stratiform orebodies is accompanied by ankerite and hyalophane. Reduced sulfur in the discordant orebodies is dominated by hydrothermal S isotope signature, whilst there is evidence of bacteriogenic sulfide in the stratiform orebodies.

1 Introduction

Sumatra has long been known as a source of Au in SE Asia. The ancient name of the island was *Svarnadvipa* which means the gold island reflecting its high Au endowment (Crow and van Leeuwen 2005). Gold occurs in classic epithermal deposits associated with Mesozoic and Cenozoic volcanic terrains covering nearly 75% of the island.

A reconnaissance survey to explore Au and base metal deposits in 1990s encountered an outcrop of stratiform, massive sulfide in black shales and siltstones as its immediate hanging wall and footwall along the Lae Sopokomil, Dairi (Middleton 2003). Although carbonate-hosted veins in North Sumatra were reported to be a source of base metals in the Dutch colonial era (van Bemmelen 1949), the discovery of the outcrop of stratiform, massive sulfide, which later is classified as a SEDEX deposit and the first of its kind in Indonesia, was novel.

Subsequent exploration and in-house resource modeling in Dairi indicated that the deposit hosts approximately 25.1 Mt ore at 10.2% Zn, 6.0% Pb and 8.4 g/t Ag. This resource is considered to be a giant SEDEX deposit (Singer 1995; Large et al. 2002). Only a few other similar deposits with much smaller resources have been discovered in Sumatra (e.g. Harahap et al. 2015). Therefore, the Dairi Zn-Pb-Ag deposit offers a significant opportunity to develop model for SEDEX Zn-Pb-Ag metallogenesis in Sumatra. This paper presents the most recent results from Dairi, confirming a SEDEX origin and offering insight into its broader genesis.

2 Geologic background

The Dairi Zn-Pb-Ag deposit is situated in the West Sumatra Block which has an Indochina affinity (Barber et al. 2005). The Indochina Super-Terrane was detached from Gondwana in the Early to Middle Devonian and had arrived at the equator by the Early Carboniferous. The Sibumasu Block collided with the Indochina Super-Terrane in the Late Permian. The West Sumatra Block was displaced along the Medial Sumatra Tectonic Zone and emplaced to the west of the Sibumasu Block in the Triassic. The Woyla Arc was thrusted over the West Sumatra Block in the Middle Cretaceous completing the tectonic assembly of present-day Sumatra (Metcalfe 2013).

The Dairi Zn-Pb-Ag deposit is located on the eastern flank of the Sopokomil Dome which is a portion of the Lower Carboniferous Kluet Formation (Fig. 1). From the bottom of stratigraphy, the rocks in the Sopokomil Dome consists of massive and brecciated dolostones (the Jehe unit), interbedded black shales and dolomitic siltstones (the Julu unit) and interbedded dolomitic sandstones and siltstones (the Dagang unit). The main composition of the Jehe unit is dolomite while that of the Julu and Dagang units are quartz, dolomite, muscovite, organic matter and K-feldspar. Diagenetic pyrite occurs in trace amounts. These rocks were subject to sub-greenschist metamorphism.

Structures in the Sopokomil Dome are predominantly controlled by NW-SE-trending thrusts and an anticline. NE-SW-trending normal faults are also present. These structures are related to deformation events during collisions of tectonic blocks and the current strike-slip Sumatra Fault System (Reynolds and Geerdts 2012).

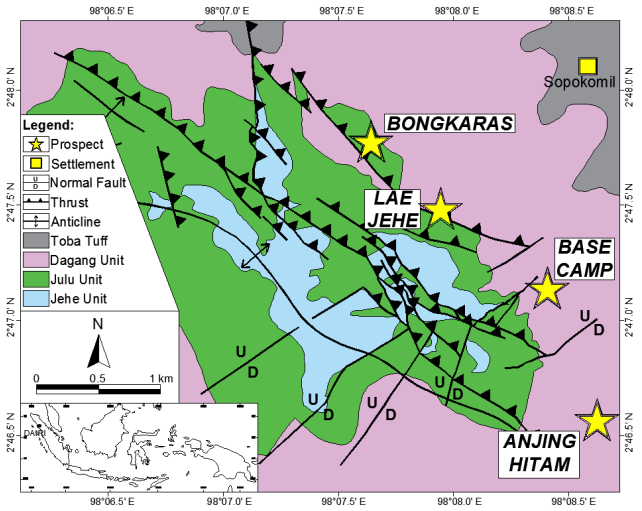

Figure 1. Geologic map of the Sopokomil Dome and distribution of prospects in the Dairi Zn-Pb-Ag deposit.

3 Dairi basin

Rocks in the Sopokomil Dome (the Dagang, Julu and Jehe units) represent a sag-phase sequence known to be favorable for SEDEX deposition (Lydon 1996). Correlation with Paleozoic stratigraphy in the Indochina Super-Terrane (Metcalfe 2017) suggests that the rift-fill sequence in the Dairi Basin may be similar to its sag-phase sequence. The similarity between the rift-fill and sag-phase sequence in the Dairi Basin is comparable to Phanerozoic SEDEX-hosting basins in North America (e.g. Selwyn, Belt-Purcell; Cooke et al. 2000).

4 Orebodies

Orebodies in the Dairi Zn-Pb-Ag deposit are present in four prospects (Anjing Hitam, Basecamp, Lae Jehe, Bongkaras) extending from SE to NW in a 4-km strike line (Fig. 1). The structurally highest Dagang unit hosts no orebodies. The Julu unit (Fig, 2) hosts stratiform orebodies consisting of three stacked layers: lower (LH), main (MH) and upper (UH) horizons. LH is limited to Lae Jehe and Bongkaras, MH is present in all prospects, and UH occurs as lenses ore horizons in Anjing Hitam, Basecamp and Bongkaras. The maximum thickness of orebodies hosted in the Julu unit is 30 m in Anjing Hitam while 5 m in Basecamp. The maximum thickness of orebodies increases to 20 m in Lae Jehe and decreases to 5 m in Bongkaras. In the Jehe unit, orebodies are discordant, but stratabound at deposit scale.

According to textures and the abundance of ore minerals, the orebodies hosted in the Julu unit are divided into pyrite-rich massive sulfide (PyMs), sphalerite-rich massive (SpMs), bedded sulfide (BS), galena-rich breccia (GnBx) and vein (V-Ju) ore types. PyMs is an ore consisting of abundant cubic hydrothermal pyrite and sphalerite-galena intergrowths filling their interstices. Cubic, hydrothermal pyrite overgrew framboidal, diagenetic pyrite in the NW portion of the deposit. In LH, pyrrhotite occurs as a dominant iron sulfide intergrown with metamorphic pyrite. SpMs is an ore type consisting of abundant sphalerite-galena intergrowths and trace pyrite. As lithic and rock layers incorporated in the orebodies increase toward the NW, the ore type changes from SpMs and PyMs to BS. GnBx is an ore type consisting of abundant galena and large, corroded, euhedral pyrite. Pyrite size is up to 3 mm. Tetrahedrite and bournonite occur as inclusions in galena. GnBx is only present in Anjing Hitam. V-Ju is dominated by sphalerite-galena intergrowths. In LH, V-Ju contains pyrrhotite as well. Gangue minerals consist of quartz, dolomite, hyalophane, trace barite and calcite.

Unit	Lithology	Mineralization
Dagang Unit	Interbedded dolomitic siltstone, dolomitic sandstone, and minor carbonaceous shale	-
Julu Unit	Interbedded carbonaceous shale and dolomitic siltstones	Concordant, stratiform, multi-horizons orebodies
Jehe Unit	Arenaceous massive and brecciated dolostone	Discordant, stratabound orebodies
Sopokomil Unit	Silicified dolostone intercalated by argillaceous sediments	-
Bongkaras Unit	Massive dolostone and deeply weathered in the surface	Zn-Pb oxide ores
Dang Takkas Unit	Magnetite-rich, feldspar-rich metasandstones; Green phyllite	-

Figure 2. Stratigraphic column of sedimentary sequence present in the Sopokomil Dome.

In the Jehe unit, the orebodies consist of vein (V-Je) and disseminated (Ds) ore types. In contrast to V-Ju, V-Je contains significant tetrahedrite, tennantite and chalcopyrite in addition to sphalerite and galena. Trace arsenopyrite coexists with tennantite. In Ds, sphalerite is associated with cubic pyrite. Galena contains Ag-sulfides and Ag-Cu-Pb sulfosalts: acanthite, pyrargyrite, boulangerite, freieslebenite and diaphorite.

Chalcopyrite, Ag-sulfides and Ag-Cu-Pb sulfosalts are abundant in the orebodies hosted in the Jehe unit. The presence of Ag-Cu-Pb sulfosalts in Anjing Hitam suggests that the SE portion of the deposit was more proximal to the feeder zone. The distribution of Cu and Ag which are less soluble in low temperature solutions compared to Pb, and that of Pb which is less soluble compared to Zn in low temperature fluids agree with the flow direction of ore-forming fluid from SE to NW in seafloor and sub-seafloor environments (Reed and Palandri 2006). This paleoflow direction is also supported by the decrease of orebody thickness and the increase of abundance of bedded sulfide ore toward NW

(Lydon 1996; Rajabi et al. 2015). In addition, the presence of LH reflects the likelihood of another feeder zone in Lae Jehe.

Deformation of orebodies are visible at mega-, hand-specimen and micro-scales. Tilting (15-50°) and disruption of ore horizons indicate deformation at mega-scales. At hand-specimen scale, the deformation is indicated by folding of ore horizons, piercement of sulfide and durchbewegung textures. Recrystallization, cataclastic deformation and fracturing of pyrite are microscopic indications of deformation (Gilligan and Marshall 1987; Vokes and Craig 1993). Fractures of pyrite were healed by soft sulfides, such as bournonite, chalcopyrite, galena, sphalerite and pyrrhotite (Barrie et al. 2010).

5 Geochemical halo

A SEDEX Alteration Index (AI) is used to identify geochemical haloes around SEDEX deposits. The equation used in the AI is ((FeO + 10MnO) x 100)/(FeO + 10MnO + MgO) (Large and McGoldrick 1998). In the Dairi Zn-Pb-Ag deposit, the AI from a barren area on the western flank of the Sopokomil Dome ranges from 41 to 53. In Anjing Hitam, the AI systematically increases from the Dagang unit (AI = 43-53) through the Jehe unit (AI = 51-75) to the stratiform orebodies (AI = 62-99). SEDEX AI of orebodies was added to compare the values in the host rocks and orebodies, although the index was designed for host rocks.

Another indicator was introduced to reveal a geochemical halo in the Dairi Zn-Pb-Ag deposit, i.e. SEDEX AI-Ba. In this indicator, Ba is used as a key enriched element and K as a key depleted element and thus the equation used in the AI-Ba is ((Ba/1000) x 100)/(Ba/1000 + K_2O). The AI-Ba in the barren area ranges from 8 to 10. In Anjing Hitam, the AI-Ba increases from the Dagang unit (7-11) through the Julu unit (9-73) to the stratiform orebodies (54-99). The increasing AI coupled with AI-Ba in the immediate hanging wall and footwall suggests that the geochemical halo in the Dairi Zn-Pb-Ag deposit is controlled by compositional change of dolomite and K-feldspar to ankerite and hyalophane, respectively.

6 Ore-forming fluid

6.1 Salinity, temperature and density

Salinity of the ore-forming fluid in the Dairi Zn-Pb-Ag deposit is distributed over three main intervals: 18-25 wt%, 3-7 wt% and 1-3 wt% NaCl eq. The saline fluid (18-25 wt% NaCl eq.) allowed the fluid to leach metals from the rift-fill sequence and to carry them to the depositional site as chloride complexes (Seward et al. 2014). Dilution by seawater reduced salinity (3-7 wt% NaCl eq.) and led to precipitation of metal sulfides and sulfosalts. The origin of the much-diluted fluid inclusions (1-3 wt% NaCl eq.) remains unexplained.

Homogenization temperatures (Th) of fluid inclusions hosted in the Julu unit are distributed over a wide range from 110° to 350°C (no distinguishable modes) which may have been affected by metamorphism. Unlike their counterpart in the Julu unit, fluid inclusions hosted in the Jehe unit range from 117° to 195°C with a distinctive mode at 160°-170°C. Probably, higher confining pressures due to deeper position of the Jehe unit could have inhibited the stretching of fluid inclusions (e.g. Leach et al. 2004).

Density of the evolved solution due to dilution was estimated using a formula proposed by Sato (1972). The end-members include ore-forming fluid (T = 170°C, salinity = 25 wt% NaCl eq.) and seawater (T = 3°C, salinity = 3.5 wt% NaCl eq.). The density model suggests that the ore-forming fluid was denser than seawater. The density of the fluid decreased to that of seawater as the fraction of seawater reached infinity. The density of the evolved fluid, which was consistently higher than that of seawater, implies that the ore-forming fluid may have formed a bottom-hugging fluid upon its discharge on the paleo-seafloor. Conceptually, capacity of the fluid to carry metals was maintained as it flowed to a local topographic depression. The density barrier then disappeared due to contact between the stagnant fluid and seawater allowing mixing to occur. The mixing resulted in the precipitation of metal sulfides to form stratiform orebodies hosted in the Julu unit.

6.2 Redox state and pH

The redox state and pH of the ore-forming fluid were strongly controlled by those of rift-fill sequence (Cooke et al. 2000). The similarity between the host rocks and rift-fill sequence in the Dairi basin may have equilibrated the ore-forming fluid to reduced and acidic conditions. The presence of pyrrhotite in LH and lack of hematite in the orebodies and immediate hanging and footwall rocks also suggest that the ore-forming fluid was reduced. Assuming total S content, dominated by $H_2S_{(aq)}$, in the ore-forming fluid was 10^{-4} *m*, the temperature of pyrrhotite and pyrite equilibrium was 125°-175°C. At 170°C, >1 ppm Zn and >1 ppm Pb can be transported by a reduced fluid at pH 3 in forms of metal-chloride complexes.

6.3 Sources of sulfur

Sulfur isotope ratios systematically increased from barren sedimentary rocks ($\delta^{34}S$ = -4.1 to +9.7‰) to orebodies in the Jehe unit ($\delta^{34}S$ = +3.5 to +8.0‰), LH ($\delta^{34}S$ = +6.4 to +18.1‰), MH ($\delta^{34}S$ = +13.5 to +28.8‰) and UH ($\delta^{34}S$ = +18.7 to +26.7‰). Sulfur isotope ratios in the barren sedimentary rocks suggest that reduced sulfur in diagenetic pyrite was generated via bacterial sulfate reduction of Carboniferous seawater sulfate. In the stratiform orebodies, the much isotopically heavier sulfides could have possibly resulted in restricted basin and anoxia development prior to mineralization, and more active bacterial systems during the discharge of ore-forming fluid into the seafloor. Distinctive isotopically light sulfides in the orebodies hosted by the Jehe unit may have been influenced by hydrothermal $H_2S_{(aq)}$ carried by the ore-forming fluid.

7 Genetic processes

Genetic processes for the formation of the Dairi Zn-Pb-Ag deposit are divided into precursor and mineralization stages. In the precursor stage, saline ore-forming fluids were generated within the rift-fill sequence and equilibrated with rift-fill sequence in reduced and acidic conditions. On the seafloor, microbes actively reduced Carboniferous seawater sulfate and precipitated dissolved ferrous ions as diagenetic pyrite along with other marine sediments. However, limited ferrous ions resulted in trace amounts of diagenetic pyrite and led to build-up of reduced sulfur concentrations in the bottom waters (anoxia development).

The onset of deeply penetrated syn-sedimentary Carboniferous faults initiated the mineralization stage by providing a pathway for the ore-forming fluid to ascend to the seafloor. The ore-forming fluid encountered descending seawater along the pathway to the seafloor thereby lowering salinity and temperature of ore-forming fluids. This encounter eventually led to the decreased solubilities of metal as chloride complexes in the ore-forming fluid. Reduced sulfur carried by the ore-forming fluid fixed metal ions to precipitate sulfide within the fractures of the Jehe unit. The amount of reduced sulfur transported in the ore-forming fluid had to be low in order for the ore-forming fluid to transport significant amounts of metals. Reduced sulfur served as the limiting reactant in sulfide precipitation within the fractures and therefore excess metal ions were transported to the seafloor by the remaining fluid.

Upon its discharge on the seafloor, the remaining ore-forming fluid, which was denser than seawater (even though it had been diluted), flowed to a local topographic depression on the seafloor. A density barrier preserved the carried metals during the flow. After the fluid was settled on the local depression, heat exchange between the ore-forming fluid and seawater decreased the temperature of the ore-forming fluid. Incorporation of biologically reduced sulfur allowed precipitation of metal sulfides forming stratiform orebodies hosted by the Julu unit.

Acknowledgements

The authors would like all colleagues in Kyushu University, Bandung Institute of Technology, PT Dairi Prima Minerals, Scottish Universities Environmental Research Centre and Geological Survey of Japan for their assistance, guidance and discussion that improve the quality of this study.

References

Barber AJ, Crow MJ (2005) Pre-Tertiary stratigraphy. In: Barber AJ, Crow MJ, Milsom JS (eds) Sumatra: Geology, Resources and Tectonic Evolution. Geological Society Memoir 31, the Geological Society, London, pp 24-62.

Barrie CD, Boyle AP, Cook NJ, Prior DJ (2010) Pyrite deformation textures in the massive sulfide ore deposits of the Norwegian Caledonides. Tectonophysics 483:269-286.

Cooke DR, Bull SW, Large RR, McGoldrick PJ (2000) The importance of oxidized brines for the formation of Australian Proterozoic stratiform sediment-hosted Pb-Zn (sedex) deposits. Econ Geol 95:1-18.

Crow MJ, van Leeuwen TM (2005) Metallic mineral resources. In: Barber AJ, Crow MJ, Milsom JS (eds) Sumatra: Geology, Resources and Tectonic Evolution. Geological Society Memoir 31, the Geological Society, London, pp 147-174.

Gilligan IB, Marshall B (1987) Textural evidence for remobilization in metamorphic environments. Ore Geol Rev 2:205-229.

Harahap BH, Abidin HZ, Gunawan W, Yuniarni R (2015) Genesis of Pb-Zn-Cu-Ag deposits within Permian Carboniferous-Carbonate Rocks in Madina Regency, North Sumatra. Indones J Geosci 2:167-184.

Large RR, McGoldrick PJ (1998) Lithogeochemical halos and geochemical vectors to stratiform sediment hosted Zn-Pb-Ag deposits, 1. Lady Loretta Deposit, Queensland. J Geochem Explor 63:37-56.

Large RR, Bull S, Selley D, Yang J, Cooke D, Garven G, McGoldrick P (2002) Controls on the formation of giant stratiform sediment-hosted Zn-Pb-Ag deposits: With particular reference to the north Australian Proterozoic. In: Cooke DR, Pongratz J (eds) Giant Ore Deposits: Characteristics, Genesis, and Exploration. CODES Special Publication 4, University of Tasmania, Australia, pp 107-149.

Leach DL, Marsh E, Emsbo P, Rombach CS, Kelley KD, Anthony M (2004) Nature of hydrothermal fluids at the shale-hosted Red Dog Zn-Pb-Ag deposits, Brooks Range, Alaska. Econ Geol 99:1449-1480.

Lydon JW (1996) Sedimentary exhalative sulphides (Sedex). In: Eckstrand OR, Sinclair WD, Thorpe RI (eds) Geology of Canadian Mineral Deposit Types. Geology of Canada 8, Geological Survey of Canada, pp 130-152.

Metcalfe I (2013) Gondwana dispersion and Asian accretion: Tectonic and paleogeogrpahic evolution of eastern Tethys. J Asian Earth Sci 66:1-33.

Metcalfe I (2017) Tectonic evolution of Sundaland. Bull Geol Soc Malays 63:27-60.

Middleton TW (2003) The Dairi zinc-lead project, North Sumatra, Indonesia – discovery to feasibility study. http://www.smedg.org.au. Accessed 15 February 2019.

Rajabi A, Rastad E, Canet C (2015) The early Cambrian Chahmir shale-hosted Zn-Pb deposit, Central Iran: An example of vent-proximal SEDEX mineralization. Miner Deposita 50:571-590.

Reed MH, Palandri J (2006) Sulfide mineral precipitation from hydrothermal fluids. Rev Mineral Geochem 61:609-631.

Reynolds NA, Geerdts M (2012) Structural controls and modification of the Sopokomil SHMS Zn-Pb deposits, Dairi, Indonesia. In: Structural and Resources – Extended Abstracts, Australian Institute of Geoscientists 56, pp 149.

Sato T (1972) Behaviours of ore-forming solutions in seawater. Mining Geol 22:31-42.

Singer DA (1995) World class bases and precious metal deposits – a qualitative analysis. Econ Geol 90:88-104.

Van Bemmelen RW (1949) The geology of Indonesia, volume II economic geology. Government Printing Office, The Hague.

Vokes FM, Craig JR (1993) Post-recrystallisation mobilization phenomena in metamorphosed stratabound sulphide ores. Mineral Mag 57:19-28.

Coupled control of intra-basinal and deep-seated geologic processes on formation of some super-large uranium and base-metal deposits in sedimentary basins

Guoxiang Chi
Department of Geology, University of Regina, Canada

Zenghua Li, Deru Xu
Faculty of Earth Sciences, East China University of Technology, China

Patrick Ledru
Orano Canada Inc.

Haixia Chu and Chunji Xue
Faculty of Earth Sciences and Resources, China University of Geosciences (Beijing), China

Abstract. The largest uranium and base metal deposits in the world are hosted in sedimentary basins. Although intra-basinal processes play important roles in mineralization, the formation of many of these deposits appears to be also related to deep-seated geologic processes. This paper provides two case studies of such coupled control of mineralization.

The unconformity-related uranium deposits in the Proterozoic Athabasca Basin, including several super-large (and high-grade) ones, are closely associated with reactivated basement faults crosscutting the basal unconformity. Despite the involvement of the basement, the mineralization processes have been general considered of basinal nature (the diagenetic-hydrothermal model), as the mineralizing fluids were basinal brines. However, the elevated fluid temperatures (up to 200 °C) at a relatively shallow burial environment (3 km or less), thus abnormal geothermal gradient, suggests that deep-seated geologic processes were involved in the mineralization.

The super-large Jinding Zn-Pb deposit in the Meso-Cenozoic Lanping Basin (China) displays many geologic characteristics similar to those of Mississippi Valley-type deposits, such as epigenetic features and association with hydrocarbons. However, the tectonically active nature of the basin, evidence of strongly overpressured mineralizing fluids, and mantle-derived noble gas and Pb isotope signatures, suggest that deep-seated processes were also involved in the mineralization.

1 Introduction

Some mineral deposits are mainly controlled by deep-seated geologic processes (e.g., diamond deposits associated with kimberlite), and some are mainly controlled by shallow or surficial processes (e.g., potash deposits in sedimentary basins), whereas some are results of coupled control of both shallow and deep-seated processes (e.g., Cu-Ni sulfide deposits associated with mafic-ultramafic magmatic rocks) (Robb 2005). For mineral deposits hosted in sedimentary basins, it is generally believed that they were formed from intra-basinal processes, although the driving forces of fluid flow may still be from outside the basin (e.g., Mississippi Valley-type Zn-Pb deposits) (Garven and Raffensperger 1997).

However, some mineral deposits in sedimentary basins, including super-large ones, appear to be controlled by both intra-basinal and deep-seated geologic processes. In such deposits, the basinal processes are relatively well manifested, whereas the effects of the deep-seated processes, concealed at great depths, are generally cryptic at the sites of mineralization, requiring careful examination of various geologic, geochemical and geophysical signatures (Fig. 1). The actual deep-seated geologic processes may be variable depending on the tectonic setting, and their contributions to mineralization may include providing fluid, metals, and heat driving fluid flow. The approaches to decipher the relationship between mineralization and the deep-seated processes thus include geochemical, geophysical, structural and hydrodynamic studies (Fig. 1).

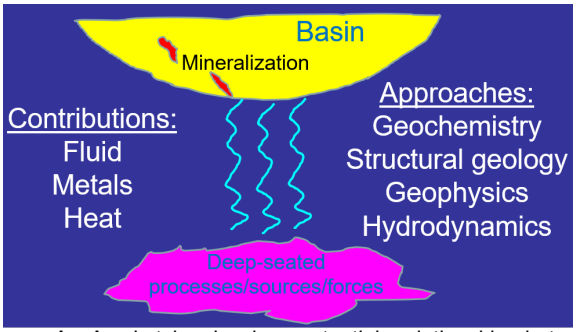

Figure 1. A sketch showing potential relationship between mineralization in the basin and deep-seated geologic processes.

This paper provides two case studies of mineralization associated with sedimentary basins that are jointly controlled by basinal and deep-seated geologic processes: the unconformity-related uranium deposits associated with the Proterozoic Athabasca

Basin in Canada and the sandstone-hosted Jinding Zn-Pb deposit in the Meso-Cenozoic Lanping Basin in China. In both cases, the traditional views are that the mineralization is mainly related to basinal processes, but we propose that deep-seated processes played a critical role in their formation.

2 Unconformity-related U mineralization in the Proterozoic Athabasca Basin (Canada)

The unconformity-related U deposits in the Proterozoic Athabasca Basin, including several super-large ones with reserves of >100 million pounds of U_3O_8 and grades of >10 wt.% U_3O_8 (IAEA 2018; NEA and IAEA 2018), are among the largest and richest U deposits in the world. These deposits have the following common characteristics: 1) they occur near the unconformity between the sedimentary basin fill and the underlying crystalline metamorphic basement rocks (thus the name "unconformity-type" or "unconformity-related"); 2) they are located at the apex of basement-hosted graphitic lithologies or shear zones marked by large low resistivity anomalies at the crustal scale; and 3) they are associated with illite ± chlorite ± tourmaline alteration halos in both the sedimentary cover and basement (Hoeve and Sibbald 1978; Hoeve and Quirt 1984; Kotzer and Kyser 1995; Fayek and Kyser 1997; Jefferson et al. 2007; Kyser and Cuney 2015).

It has been generally agreed that the mineralizing fluids were basinal brines of evaporated sea water origin derived from the Athabasca Basin (Hoeve and Sibbald 1978; Hoeve and Quirt 1984; Kyser et al. 2000; Richard et al. 2011, 2014; Mercadier et al. 2012). The uranium is inferred to be sourced either from the basin detritus (Hoeve and Sibbald 1978; Hoeve and Quirt 1984; Kotzer and Kyser 1995; Fayek and Kyser 1997; Kyser et al. 2000), or from the basement rocks (Dahlkamp 1978; Annesley and Madore 1999; Hecht and Cuney 2000; Cuney et al. 2003; Richard et al. 2010, 2016; Mercadier et al. 2013; Martz et al. 2018).

Both fluid mixing and fluid-rock interactions have been proposed as mechanisms for ore precipitation, with graphite and ferrous iron-rich minerals being invoked as the main sources of reducing agents, either in the form of mobile hydrocarbons and dissolved species in solutions, or as solid reactants (Hoeve and Sibbald 1978; Hoeve and Quirt, 1984; Alexandre et al. 2005; Yeo and Potter 2010). More recently, fluid boiling or phase separation has been suggested to have also played a role based on observation of vapor-rich fluid inclusions in many uranium deposits (Chi et al. 2017; Wang et al. 2018). The fluid flow related to mineralization has been inferred to be caused by thermal gradient-induced fluid convection and/or deformation-driven fluid flow (Raffensperger and Garven 1995; Cui et al. 2012; Li et al. 2016, 2017, 2018).

The above geological characteristics and interpretations appear to support a general model in which the ore-forming fluids, the metals and the driving forces of fluid flow are derived from within the basin or its immediate basement rocks, as described in the conventional diagenetic-hydrothermal model (Pagel 1975; Hoeve and Sibbald 1978; Pagel et al. 1980; Hoeve and Quirt 1984; Kotzer and Kyser 1995). It is inferred that the mineralization took place at burial depth >5 km in order to explain the elevated fluid temperatures of > 200 °C, which seems to be supported by elevated fluid pressures (up to 1500 bars) calculated from fluid inclusion data (Pagel 1975). In such a model, the thermal gradient in the basin and basement would be about 35 °C/km, which is normal for an intracratonic basin or foreland basin. The mineralization processes can thus be linked with normal diagenesis within the basin and infiltration of the basinal brines into the upper part of the basement, without the need to invoke deep-seated processes.

However, as discussed in Chi et al. (2018), the high fluid pressures estimated by Pagel (1975) are inconsistent with a hydrostatic fluid pressure regime as predicted for a sand-dominated basin (Chi et al. 2013). Furthermore, based on regional geochronological and stratigraphic data and the interpretation that the ore-forming fluids originated from evaporated sea water (Richard et al. 2011), Chi et al. (2018) inferred that the primary uranium mineralization in the Athabasca Basin took place during the deposition of the stromatolitic carbonates of the Carswell Formation, which contains evidence of development of evaporites (Ramaekers et al. 2007). At this time of the basin history, the burial depth of the basal unconformity was likely less than 3 km (Chi et al. 2018) (Fig. 2).

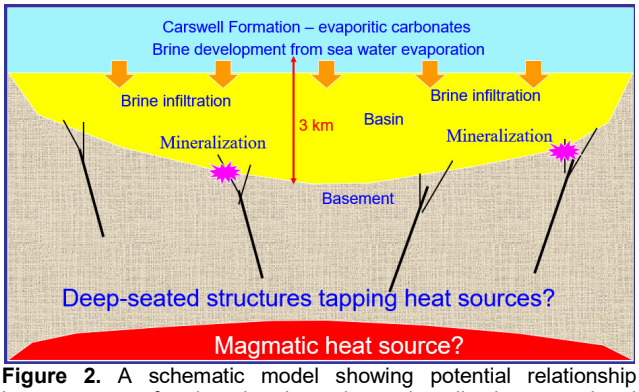

Figure 2. A schematic model showing potential relationship between unconformity-related uranium mineralization associated with the Athabasca Basin and intra-basinal processes (especially development of basinal brines) as well as deep-seated processes, which may have played an important role in driving fluid flow leading to mineralization.

Based on this shallow-burial hypothesis, and in order to explain the elevated fluid temperatures of > 200 °C (Chu and Chi 2016), the geothermal gradient during the time of mineralization may be up to two times higher than the normal geothermal gradient. This abnormal geothermal gradient is likely caused by some deep-seated geologic processes, although their nature (e.g., magmatic or structural) remains to be investigated (Fig. 2). It is interesting to note that the basement architecture inherited from the Paleoproterozic orogenes is characterized by steeply dipping, large shear zones separating continental-scale blocks exhumed from the

lower granulitic crust prior to the deposition of the basin. These deeply rooted fault systems have been reactivated several times due to far field tectonic events after the deposition of the basin, and may have served as conduits of crustal-scale fluid flow transferring fluids from deep crustal level to shallow basement structures near the unconformity, some of which host uranium mineralization. In summary, based on the above discussion, it is proposed that the unconformity-related uranium deposits associated with the Athabasca Basin resulted from the coupling of basinal processes (especially development of basinal brines) and deep-seated processes (Fig. 2), the latter of which may have played an important role in driving fluid flow.

3 Sandstone-hosted Jinding Zn-Pb deposit in the Meso-Cenozoic Lanping Basin (China)

The Jinding Zn-Pb deposit is hosted by Cretaceous to Tertiary sandstones and conglomerates in the Lanping Basin in southwestern China (Xue et al. 2007). It has a reserve of approximately 220 million tons of ore grading 6.1% Zn and 1.3% Pb, and represents the largest sandstone-hosted Zn-Pb deposit in the world (Xue et al. 2007).

The deposit shares many geological characteristics with the Mississippi Valley-type deposits, however it differs from the latter not only in terms of host rocks, but also in terms of tectonic setting in that the Lanping Basin is a tectonically active basin linked with tectonic processes at depth, as evidenced by strong deformation of the strata in the basin and development of deep-penetrating faults and mantle-derived magmatic intrusions (Xue et al. 2007).

Fluid inclusion studies indicate that the deposit formed from interaction between hot, metal-carrying brines and H2S generated by bacterial sulfate reduction (BSR) through reaction with hydrocarbons in a reservoir hosted by the Jinding dome (Chi et al. 2017). Although this may appear to be a typical intra-basinal process, noble gas isotopes of fluid inclusions and Pb isotopes of sulfides in the ores suggest that a significant amount of the ore-forming fluid may have been derived from a mantle source (Xue et al. 2007).

Furthermore, fluid inclusion data, coupled with field observations such as sand injection structures (Chi et al. 2007), suggest that the mineralization system was episodically overpressured, which cannot be explained by intra-basinal processes (e.g., sediment compaction; Chi et al. 2006) and requires extra-basinal input (e.g., volatiles from the mantle) (Fig. 3).

In addition, the inference that H2S accumulated in the gas cap of the paleo-oil and gas reservoir participated in the mineralization necessitates that the ore-forming fluids were overpressured and able to penetrate the oil in the reservoir and reach the gas cap (Fig. 3), supporting the hypothesis that the ore-forming fluids were driven by deep-seated driving forces.

Therefore, the Jinding deposit represents another example of mineralization that resulted from joint action of intra-basinal processes (development of oil and gas reservoirs and basinal brines), which provide part of the ore-forming fluids and metals as well as geochemical traps, and deep-seated geological process which may have provided additional ore-forming fluids, metals and fluid flow driving forces.

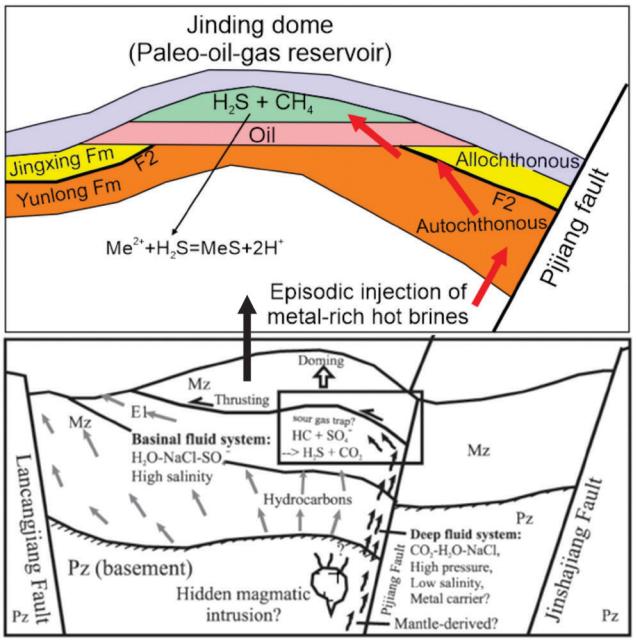

Figure 3. A schematic model showing potential relationship between the Jinding Zn-Pb deposit, intra-basinal processes (especially development of basinal brines and an oil-gas reservoir with a sour gas cap) as well as deep-seated processes, which may have played an important role in driving fluid flow and contributing part of the ore-forming fluid and metals.

Acknowledgements

This study is supported by NSERC-Discovery grant and Orano Canada Inc.

References

Alexandre P, Kyser K, Polito P, Thomas D (2005) Alteration mineralogy and stable isotope geochemistry of Paleoproterozoic basement-hosted unconformity-type uranium deposits in the Athabasca Basin, Canada. Econ Geol 100:1547–1563

Annesley IR, Madore C (1999) Leucogranites and pegmatites of the sub-Athabasca basement, Saskatchewan: U protore? In: Stanley CJ (ed), Mineral Deposits: Processes to Processing, Balkema, Rotterdam, 297–300

Chi G, Qing H, Xue C, Zeng R (2006) Modeling of fluid pressure evolution related to sediment loading and thrust faulting in the Lanping basin – implications for the formation of the Jinding Zn-Pb deposit, Yunnan, China. J Geochem Explor 89:57–60

Chi G, Xue C, Lai J, Qing H (2007) Sand injection and liquefaction structures in the Jinding Zn-Pb deposit, Yunnan, China: indicators of an overpressured fluid system and implications for mineralization. Econ Geol 102:739–743

Chi G, Bosman S, Card C (2013) Numerical modeling of fluid pressure regime in the Athabasca basin and implications for fluid flow models related to the unconformity-type uranium mineralization. J Geochem Explor 125:8–19

Chi G, Haid T, Quirt D, Fayek M, Blamey N, Chu H (2017) Petrography, fluid inclusion analysis and geochronology of the

End uranium deposit, Kiggavik, Nunavut, Canada. Miner Deposita 52:211–232
Chi G, Xue C, Sun X, Luo P, Song H, Li S, Zeng R (2017) Formation of a giant Zn-Pb deposit from hot brines injecting into a shallow oil-gas reservoir in sandstones, Jinding, southwestern China. Terra Nova 29:312–320
Chi G, Li Z, Chu H, Bethune KM, Quirt DH, Ledru P, Normand C, Card C, Bosman S, Davis WJ, Potter EG (2018) A shallow-burial mineralization model for the unconformity-related uranium deposits in the Athabasca Basin. Economic Geology 113:1209–1217
Chu H, Chi G (2016) Thermal profiles inferred from fluid inclusion and illite geothermometry from sandstones of the Athabasca basin: Implications for fluid flow and unconformity-related uranium mineralization. Ore Geol Rev 75:284–303
Cui T, Yang JW, Samson IM (2012a) Tectonic deformation and fluid flow: Implications for the formation of unconformity-related uranium deposits. Econ Geol 107:147–163
Cuney M, Brouand M, Cathelineau M, Derome D, Freiberger R, Hecht L, Kister P, Lobaev V, Lorilleux G, Peiffert C, Bastoul AM (2003) What parameters control the high-grade-large tonnage of Proterozoic unconformity related uranium deposits? Proc Int Conf U Geochem, Nancy, France, pp123–126
Dahlkamp FJ (1978) Geological appraisal of the Key Lake U-Ni deposits, northern Saskatchewan. Econ Geol 73:1430–1449
Fayek M, Kyser TK (1997) Characterization of multiple fluid-flow events and rare-earth element mobility associated with formations of unconformity-type uranium deposits in the Athabasca Basin, Saskatchewan. Can Mineral 35:627–658
Garven G, Raffensperger JP (1997) Hydrogeology and geochemistry of ore genesis in sedimentary basins. In Barnes HL (ed) Geochemistry of Hydrothermal Ore Deposits (third ed), John Wiley and Sons, New York, pp 125–189
Hetch L, Cuney M (2000) Hydrothermal alteration of monazite in the Precambrian basement of the Athabasca Basin: implications for the genesis of unconformity-related deposits. Mineral Deposita 35:791–795
Hoeve J, Quirt DH (1984) Mineralization and host rock alteration in relation to clay mineral diagenesis and evolution of the Middle-Proterozoic Athabasca basin, northern Saskatchewan, Canada. Sask Research Council Tech Rpt 187, pp1–187
Hoeve J, Sibbald TII (1978) On the genesis of Rabbit Lake and other unconformity-type uranium deposits in northern Saskatchewan, Canada. Econ Geol 73:1450–1473
IAEA (2018) Geological classification of uranium deposits and description of selected examples. IAEA-TECDOC-1842, 415 p
Jefferson CW, Thomas DJ, Gandhi SS, Ramaekers P, Delaney G, Brisbin D, Cutt C, Quirt D, Portella P, Olson RA (2007) Unconformity-associated uranium deposits of the Athabasca Basin, Saskatchewan and Alberta. Geol Surv Can Bull 588:23–67
Kotzer T, Kyser T (1995) Petrogenesis of the Proterozoic Athabasca Basin, northern Saskatchewan, Canada, and its relation to diagenesis, hydrothermal uranium mineralization and paleohydrogeology. Chem Geol 120:45–89
Kyser K, Cuney, M (2015) Chapter 8: Basins and U and deposits. Mineralogical Association of Canada Short Course Series 46:225–304
Kyser TK, Hiatt E, Renac C, Durocher K, Holk G, Deckart K (2000) Diagenetic fluids in Paleo- and Meso-Proterozoic sedimentary basins and their implications for long protracted fluid histories. Mineral Assoc Can Short Course 28:225–262
Li Z, Chi G, Bethune KM (2016) The effects of basement faults on thermal convection and implications for the formation of unconformity-related uranium deposits in the Athabasca Basin, Canada. Geofluids 16:729–751
Li Z, Chi G, Bethune KM, Thomas D, Zaluski G (2017) Structural Controls on Fluid Flow During Compressional Reactivation of Basement Faults: Insights from Numerical Modeling for the Formation of Unconformity-Related Uranium Deposits in the Athabasca Basin, Canada. Econ Geol 112:451–466
Li Z, Chi G, Bethune KM, Eldursi E, Thomas D, Quirt D, Ledru P (2018) Synchronous egress and ingress fluid flow related to compressional reactivation of basement faults: the Phoenix and Gryphon uranium deposits, southeastern Athabasca Basin, Saskatchewan, Canada. Miner Deposita 53: 277–292
Martz P, Mercadier J, Cathelineau M, Boiron M-C, Quirt D, Doney A, Gerbeaud O, De Wally E, Ledru P (2018) Formation of U-rich mineralizing fluids through basinal brine migration within basement hosted shear zones: A large-scale study of the fluid chemistry around the unconformity-related Cigar Lake U deposit (Saskatchewan, Canada). Chemical Geology: doi.org/10.1016/j.chemgeo.2018.05.042
Mercadier J, Richard A, Cathelineau M (2012) Boron- and magnesium-rich marine brines at the origin of giant unconformity-related uranium deposits: $\delta^{11}B$ evidence from Mg-tourmalines. Geology 40:231–234
Mercadier J, Annesley IR, McKechnie CL, Bogdan TS, Creighton S (2013) Magmatic and metamorphic uraninite mineralization in the western margin of the Trans-Hudson Orogen (Saskatchewan, Canada): major protores for unconformity-related uranium deposits. Econ Geol 108:1037–1065
NEA & IAEA (2018) Uranium 2018: Resources, production and demand. OECD 2018, NEA No. 7413, 457 p
Pagel M (1975) Détermination des conditions physico-chimiques de la silicification diagénétique des grès Athabasca (Canada) au moyen des inclusions fluides. Comptes Rendus Académie Sciences Paris 280:2301–2304
Pagel M, Poty B, Sheppard MFS (1980) Contribution to some Saskatchewan uranium deposits mainly from fluid inclusion and isotopic data. In: Ferguson J, Goleby A (eds), Uranium in the Pine Creek Geosyncline. IAEA, Vienna, 639–645
Raffensperger JP, Garven G (1995) The formation of unconformity type uranium ore deposits: 1. Coupled groundwater flow and heat transport modeling. Am J Sci 295:581–636
Ramaekers P, Jefferson CW, Yeo GM, Collier B, Long DGF, Drever G, McHardy S, Jiricka D, Cutts C, Wheatley K, Catuneanu O, Bernier S, Kupsch B, Post RT (2007) Revised geological map and stratigraphy of the Athabasca Group, Saskatchewan and Alberta. Geol Surv Can Bull 588:155–191
Richard A, Pettke T, Cathelineau M, Boiron M, Mercadier J, Cuney M, Derome D (2010) Brine-rock interaction in the Athabasca basement (McArthur River U deposit, Canada): consequences for fluid chemistry and uranium uptake. Terra Nova 22:303–308
Richard A, Banks D, Mercadier J, Boiron M, Cuney M, Cathelineau M (2011) An evapourated seawater origin for the ore-forming brines in unconformity-related uranium deposits (Athabasca Basin, Canada): Cl/Br and delta 37Cl analysis of fluid inclusions. Geochim Cosmochim Acta 75:2792–2810
Richard A, Kendrick MA, Cathelineau M (2014) Noble gases (Ar, Kr, Xe) and halogens (Cl, Br, I) in fluid inclusions from the Athabasca Basin (Canada): Implications for unconformity-related U deposits. Precambrian Res 247:110–125
Richard A, Cathelineau M, Boiron M-C, Mercadier J, Banks DA, Cuney M (2016) Metal-rich fluid inclusions provide new insights into unconformity-related U deposits (Athabasca Basin and Basement, Canada). Miner Deposita 51:249–270
Robb L (2005) Introduction to ore-forming processes. Blackwell Publishing, 373 p
Wang K, Chi G, Bethune KM, Li Z, Blamey N, Card C, Potter EG, Liu Y (2018) Fluid P-T-X characteristics and evidence for boiling in the formation of the Phoenix uranium deposit (Athabasca Basin, Canada): implications for unconformity-related uranium mineralization mechanisms. Ore Geol Rev 101:122–142
Xue C, Zeng R, Liu S, Chi G, Qing H, Chen Y, Yang J, Wang D (2007) Geologic, fluid inclusion and isotopic characteristics of the Jinding Zn-Pb deposit, western Yunnan, South China: A review. Ore Geol Rev 31:337–359
Yeo GM, Potter EG (2010) Review of reducing mechanisms potentially in the formation of unconformity-type uranium deposits and their relevance to exploration. Sask Geol Survey, Summary of Investigation 2010, 2:13.

Influence of inherited structures as fluid-thermal conduits applied to the formation of uranium mineralisation in the Athabasca Basin, Canada

Jonathan Poh[1], Philippe Yamato[1], Thibault Duretz[1], Philippe Yamato[2], Khalifa Eldursi[3], Guoxiang Chi[3], Patrick Ledru[4]
[1]*Univ Rennes, CNRS, Géosciences Rennes, France*
[2]*Institut Universitaire de France, Paris, France*
[3]*Department of Geology, University of Regina, Canada*
[4]*Orano Canada Inc., Saskatoon, Canada*

Abstract. Ore deposit formation requires the synchronisation of multiple processes with transportation of fluids and heat. Ancient inherited structures found within the basement of the Athabasca Basin were formed as a result from of orogenic processes (i.e nucleation and accretion processes). It is established that their reactivation played a significant role for the formation of the unconformity-related uranium deposits. The time gap between the inherited structures' inception and mineralisation event is sufficient for any traces of hydrothermal systems to reach steady state. The aim of this study is to determine the role for these inherited structures affecting the hydrothermal dynamics, by using a pre-existing tectonic structure generated from a thermo-mechanical study and incorporating fluid-thermal processes until steady-state conditions. The models are then experimented with permeability fields of increasing complexity in three types of tectonic scenarios. Results indicate that deep-seated structures operate as fluid-thermal conduits that bring fluids and heat towards the upper portions of the crust. In addition, thermal convection occurs at favourable permeability conditions. The experimentation of models in different permeability fields provides a general framework for the Athabasca Basin suggesting the transportation of basement-associated fluids and heat to the surface.

1 Introduction

The formation of ore deposits is related to hydrothermal systems at depth in order to precipitate and concentrate minerals (McCuaig and Hronsky 2010 and references therein). One of the known vehicles for fluid-flow, a favourable whole lithosphere architecture, is capable of pre-determining location of future ore deposits (e.g. Cathes and Adams 2005, Cox 2005). The extent of these lithospheric-scale structures can be masked from subsequent geological events and would require the use deep sub-surface imaging techniques (seen in the Indian orogeny in McCuaig and Hronsky, 2010). These deep-seated inherited structures were formed as the result of orogenic processes (Audet and Bürgmann 2011).

Similarly, the nucleation of the western Canadian Shield and its subsequent Proterozoic accretion (such as the Trans-Hudson Orogeny (THO), Alexandre et al. 2007) led to the formation of steeply-dipping shear zones within the Archean Basement of the Athabasca Basin. In between the Archean Mudjatik and Paleoproterozoic Wollaston domains lies a NE-SW trending structural corridor characterised by a highly strained zone presenting steeply dipping anastomosed shear zones that extends over several hundred kilometres along strike (i.e the Wollaston-Mudjatik Transition Zone). This tectonic evolution has been sealed from around 1.75 Ga with the deposition of the Athabasca Basin that rest unconformably over these two deeply eroded domains. Recent geochemical analysis along the structural corridor established that uranium mineralisation was coeval with the reactivation of those fore-mentioned structures (e.g. Mercadier et al. 2013) and is later confirmed in recent numerical experiments (e.g. Li et al. 2018). This event occurred 150 Ma after the deposition of the Athabasca Basin (e.g. Jefferson et al. 2007). Additionally, there was a period of 190 to 240 Ma of tectonic silence between peak-metamorphic THO and the deposition of the Athabasca Basin.

With such long durations between significant tectonic events, any potential fluid-flow activity will eventually reach steady-state conditions. Using a pre-generated tectonic model in relation to the basement of the Athabasca Basin, three types of fluid-thermal modelling scenarios leading up to the deposition of the Athabasca Basin are then constructed to determine hydrodynamic behaviour and ascertain the role of these deep-seated structures in multiple permeability configurations. The implications to how the geological environment prepares for mineralisation is discussed.

2 Modelling Approach

2.1 MDoodz and FLAC3D - Adding fluid-thermal processes to regional lithospheric settings

The experiments were conducted using a numerical code that solves Darcy's law equation to compute the fluid flow rate anytime in a solid matrix controlled by its given permeability (e.g. a tectonic structure prior to tectonic reactivation). The initial geological and structural geometry input (MGeol in Fig. 1) was the outputs taken from a 2D thermo-mechanical study made to understand Precambrian orogenic processes under hot lithospheric conditions (Poh et al. in prep). The

reference model was chosen from the parametric study according to its agreement with the available geological and metamorphic observations of the Trans-Hudson Orogeny, West Canadian Shield. The fluid-thermal code used here is the Fast Lagrangian Analysis of Continua in 3 Dimensions (FLAC3D, Itasca 2012) that has been widely applied to low-temperature geothermal and mineral system simulations (e.g. Li et al. 2018).

2.2 Model setup and boundary conditions

The vertical structures marking the Wollaston-Mudjatik Transition Zone correlates to large shear zones that could predetermine the locations for mineral deposits (e.g. Jefferson et al. 2007). The selected geological and associated geometry is used as inputs and permeability values are assigned to the different rock units (Fig. 1). All models M1 to M4 Topo have the rocks assigned with constant permeability values. The meta-sediments are assigned as permeable (k = 1.e-14 m^2) whereas the basement is assigned as impermeable (k = 1.e-18 m^2). Models M2 and M3 employ a simplified depth-dependent permeability in the basement and in the meta-sediments. Models M4 and M4 Topo introduce the deformed rocks (deformed basement at k = 1.e-16 m^2 and deformed meta-sediments at k = 2.e-14 m^2) as regions of slightly higher permeability. M4 Topo has the same permeability configuration as M4 but also takes into account the effect of topography. The third scenario, M5 (not shown here due to lack of space), consider the tectonic events leading to the deposition of the Athabasca Basin and the model design is inspired from Li et al. (2018). The geometry for the deformed zones were taken from the accumulated strain profile in the thermo-mechanical study. These strains were recorded in the preceding period of orogenic build up.

For all the experiments, the horizontal and vertical boundary conditions were set to no fluid flow across the boundary. The entire model box is initially saturated in fluids. The initial thermal profile is made in two parts depending on depth. The surface temperature is set at 20˚C and is then computed as a linear geothermal gradient of 30˚C/km until 600˚C (i.e. z ~ 20 km depth). Below, the thermal gradient is such as it reaches 1300˚C at the bottom boundary. This thermal profile hence corresponds to a standard geothermal gradient for Precambrian craton.

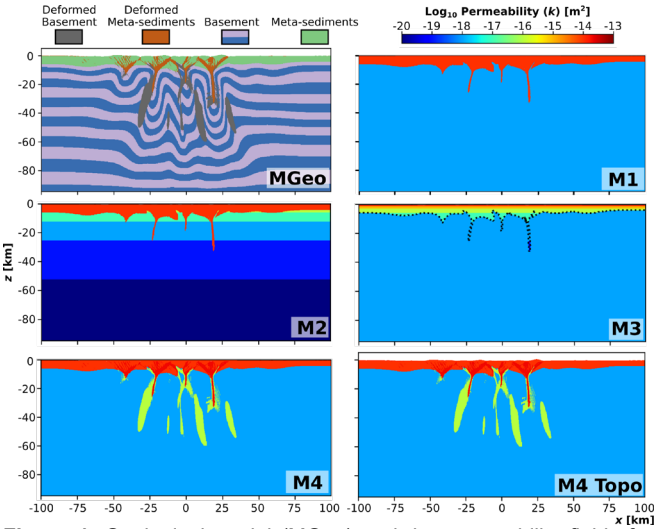

Figure 1. Geological model (MGeo) and the permeability fields for models M1 - M4 Topo of increasing levels of complexity. See text for description

The estimation of rock permeability, k (m^2), in any geologic model is a requirement for any fluid flow processes. Assigning permeability values to rocks is a challenge considering its wide range and sensitive to physical processes to either enhance or degrade its value (Rutqvist and Stephansson 2003). Here we use an initial background permeability field in which rock permeability is assumed to be homogenous and it undergoes an exponential decay according to depth, expressed as: log k = -14 - 3.2 log z, where z corresponds to depth in km (Manning and Ingebitsen 1999).

The width for the deformed zones (seen in Fig. 1) is perhaps the most controversial. Previous fluid-thermal modelling simulations on the Ashanti belt had the dimensions of 10 km (x) by 15 km (z) with an assigned constant permeability of 1.e-15 to 1.e-14 m^2 (Harcouët-Menou et al. 2009). The dimensions for the deformed zones in our models have 5 km as maximum width (M4 and M4 Topo in Fig. 1) and 3 km width for the deep-rooted structures (M1 and M2 in Fig. 1). The assigned permeability values are similar with what Harcouët-Menou et al. (2009) used and is considered as conservative.

3 Results

3.1 Fluid-thermal reference models (M1 – M3)

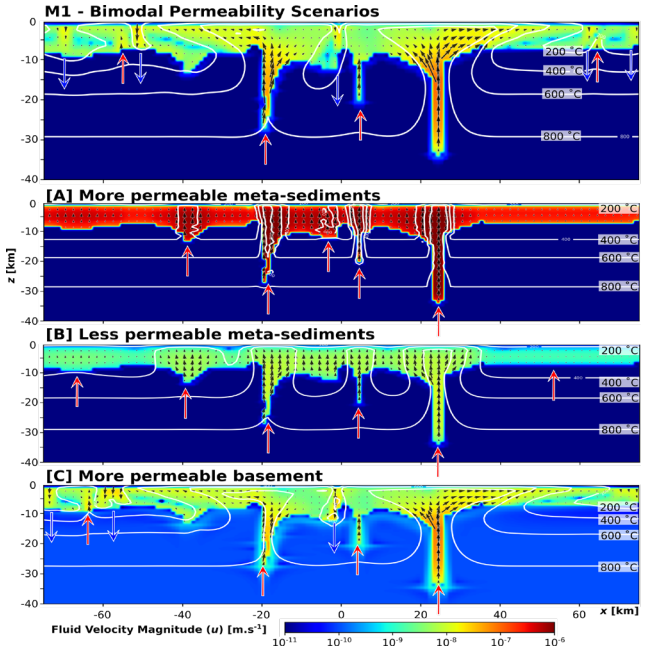

Figure 2. Fluid flow results are shown as fluid velocity magnitude and their corresponding vectors at steady state for M1 models with their variations in A, B, and C. White lines represent isotherms. Red and blue arrows correspond to the vertical direction of fluid vectors. A pair of blue and red arrows indicate fluid-thermal convection occurrence.

The reference model (M1 in Fig 2) shows thermal anomaly outputs (up to 800 ˚C) and fluid velocities up to 2 orders of magnitude within the tectonic structures when compared to the rest of the model. Occurrence for convection currents is represented by the cycle shape of the 200 ˚C isotherms within the meta-sediments and vector outputs (illustrated by red and blue arrows in Fig. 2). The results in the model variations of M1 (Fig. 2A, B and C) reinforce the fact that deep-seated structures operate as fluid-thermal conduits in all model variations (i.e. high thermal upwelling anomaly and fluid velocities). When the permeability in meta-sediments was changed, two notable changes ensured; 1) fluid-thermal convections did not occur and 2) the change of the permeability reflects the corresponding increase (Fig. 2A) and decrease (Fig. 2B) in fluid velocity by an order of magnitude. The thermal anomaly distribution in Fig. 2B is more gentle compared to Fig. 2A. An additional scenario was conducted by making the basement more permeable (Fig. 2C). The results for the fluid patterns are comparable with M1 except for the fluid velocity within the basement increased by an order of magnitude.

Depth-dependent permeability fields were applied within the basement for M2 (Fig. 3) and the meta-sediments in M3 (Fig. 4). The permeability for the basement in M3 is set to impermeable (1.e-18 m^2). In M2, the fluid-thermal patterns are similar to the results in M1 but with increasing in the number of fluid-thermal convection cells. Fluid velocities near the contact between the basement and the meta-sediments at 10 km depth are increased by an order of magnitude. The simplified depth-permeability of the basement gave additional 'space' for the fluid-thermal convections to occur. When the permeability of the meta-sediments changed (Fig. 3A and B), the corresponding changes to the fluid velocities are observed. However, in in both permeability cases, occurrence for convection currents did not occur. Instead, a secondary build-up of temperature within thermal anomaly (black arrow in Fig. 3A). Additionally, the chaotic thermal anomaly did not occur under when the meta-sediments are less permeable by an order of magnitude (Fig. 3B).

The power-law permeability-decay function was applied within the meta-sediments while maintaining an impermeable basin in M3 (Fig. 4). Overall fluid velocity was significantly reduced within the vertical structures. However, the 200 ˚C isotherm's cyclical behaviour suggest micro-circulation of fluids closer to the surface, which can be viewed by plotting a line plot of the horizontal component of the fluid velocity. The model variation to a more permeable basement (Fig. 4A), the thermal profile became more homogeneous without any fluid convections. Implementing a less permeable basement resulted in a periodic 200 ˚C isotherm with the observable instance of circulation of fluids (Fig. 4B).

3.2 M4 and M4 Topo: retrograde metamorphic THO tectonic setting

The results obtained for M4 and M4 Topo are consistent with previous scenarios, by displaying high fluid-thermal anomalies as a result of large permeable zones (Fig. 3).

Fluid velocities within the pre-deformed meta-sediments and basement were observed to have half

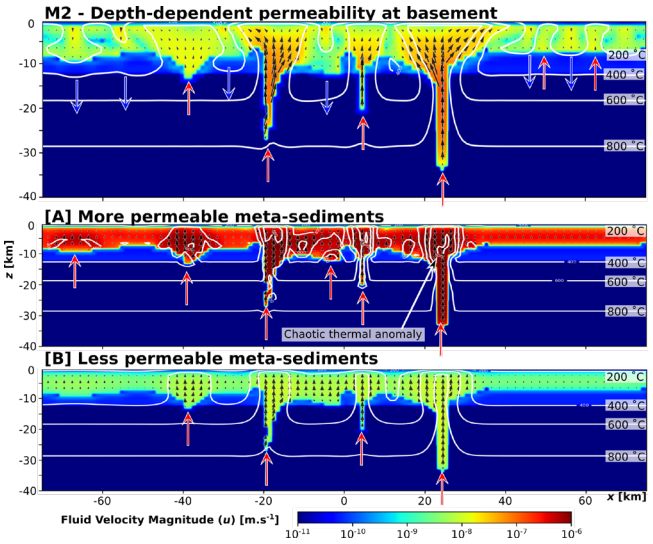

Figure 3. Fluid flow results shown as fluid velocity magnitude and their corresponding vectors at steady state for M2 models with their variations in A and B. Legend is as for figure 2.

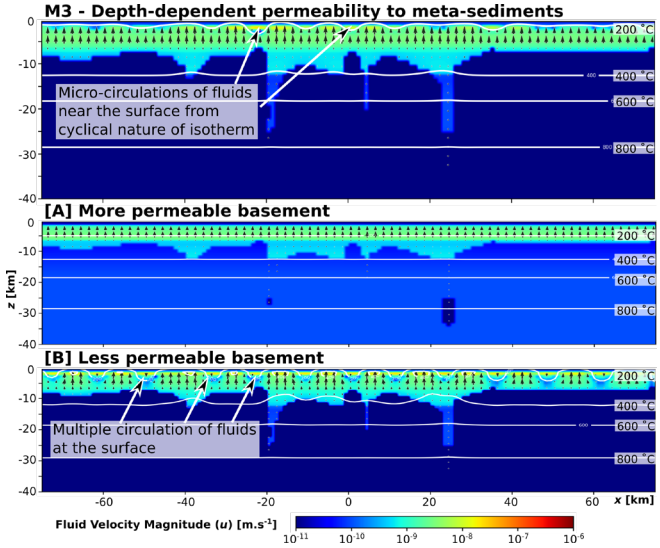

Figure 4. Fluid flow results shown as fluid velocity magnitude and their corresponding vectors at steady state for M3 models with their variations in A and B. White lines represent isotherms.

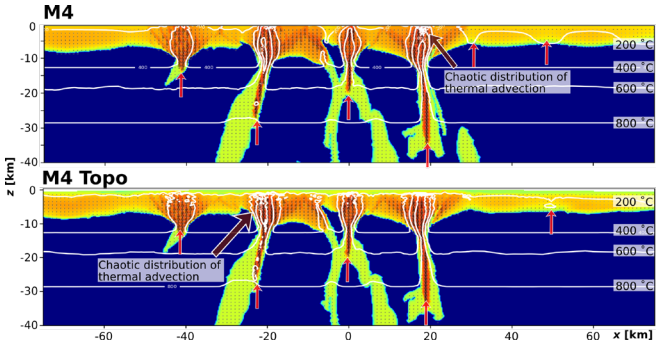

Figure 5. Fluid flow shown as fluid velocity magnitude and their corresponding vectors at steady state for M4 and M4 Topo. Fluid velocity magnitude colour scale follows the scale in Figure 4.

and 2 times order of magnitude greater than their parent rocks respectively.

Under this permeability setting, fluid-thermal convection did not occur in these scenarios. When the geometries of the deformed zones were included, this not only increases the overall area of more permeable zones, but the rate of fluid-thermal advection is increased as well. The numerical simulation became more unstable as simulation progressed. The difference between the upper thermal boundary (20 ˚C) and the thermal-fluid anomaly (~ 800 ˚C at u > 1.e-7 $m.s^{-1}$) resulted from a chaotic distribution of thermal advection close to the surface. An additional test was conducted at reduced permeability for the meta-sediments and deformed counterparts, chaotic thermal anomalies did not occur.

M4 Topo included the topography seen in the MGeol (Fig. 1) in which to simulate the effects of topography (max topography ~1 km). Previous fluid-thermal results indicate topography enhances the lateral distribution of the fluids (Hayba and Ingebritsen 1987). However, we did not observe the enhancement of lateral distribution due to the high fluid-thermal advection at depth.

3.3 M5: initial Athabasca basin formation prior to tectonic reactivation setting

The fluid-thermal results for M5 (not shown here) continue to be consistent with the previous scenarios that the deep-seated structures operate as fluid-thermal conduits. Above each aperture of the permeable deep-seated structures, the assigned permeability was conducive for fluids to undergo free convection. The main convection cells found within the basin and permeable deep-seated structures has a wavelength of 5 km, accompanied with fluid velocities of 10^{-7} $m.s^{-1}$. Elevated thermals were also observed at the contact between the permeable deep-seated structures and basin reaching at least 250 ˚C at 6 km depth (~ 41.67 ˚C.km^{-1}).

4 Discussion

In every tested scenario, these deep-seated structures provides the necessary infrastructure to transport fluids and heat to the surface through the form of elevated thermals and faster fluid velocities. The elevated temperatures at the permeable deep-seated structures in M5 correlates well to the fluid inclusion data for uranium mineralisation (e.g. Mercadier et al. 2013) as well as meeting the thermal requirements for the chloritisation of biotite during retrograde metamorphic THO. This particular alteration pattern is essential for the precipitation of graphite, a key chemical reductant for precipitating uranium. Together with the physical conditions required for convection currents is essential for the mixing of basinal and basement fluids, will increase fluid-rock interactions.

5 Conclusion

The fluid-thermal results from the experimentation of different permeability configurations of increasing complexity generate two main conclusions: 1) the deep-seated inherited structures (up to 30 km depth) function as fluid-thermal conduits, bringing fluid and heat towards the upper portions of the crust, and 2) convection cells appearing laterally away from the structures under favourable permeability configurations. The presence for these permeable deep-seated structures are hence instrumental in providing the necessary physical conditions as well as the structural infrastructure to enhance fluid-rock interaction and form regions of key chemical reductants essential for uranium mineralisation.

Acknowledgments

This work is a part of the first author's PhD thesis and is supported financially by Orano Canada Inc. Special thanks to the GeoFluids lab at the University of Regina for running the numerical simulations.

References

Alexandre P, Kyser K, Thomas D, et al (2009) Geochronology of unconformity-related uranium deposits in the Athabasca Basin, Saskatchewan, Canada and their integration in the evolution of the basin. Miner Depos 44:41–59. doi: 10.1007/s00126-007-0153-3

Audet P, Bürgmann R (2011) Dominant role of tectonic inheritance in supercontinent cycles. Nat Geosci 4:184–187. doi: 10.1038/ngeo1080

Cathles L, Adams J (2005) Fluid flow and petroleum and mineral resources in the upper (<20 km) continental crust. Econ Geol 100th Anni:77–110

Cox SF (2005) Coupling between Deformation, Fluid Pressures and Fluid Flow in Ore-Producing Hydrothermal Systems at Depth in the Crust. Econ Geol Economic G:39–75

Harcouët-Menou V, Guillou-Frottier L, Bonneville A, et al (2009) Hydrothermal convection in and around mineralized fault zones: insights from two- and three-dimensional numerical modeling applied to the Ashanti belt, Ghana. Geofluids 9:116–137. doi: 10.1111/j.1468-8123.2009.00247.x

Hayba DO, Ingebritsen SE (1997) Multiphase groundwater flow near cooling plutons. J Geophys Res Solid Earth 102:12235–12252. doi: 10.1029/97JB00552

Itasca (2012) FLAC3D: Fast Lagrangian Analysis of Continua in 3 Dimensions, User Manual, Version 5.0. Itasca Consulting Group Inc., Minneapolis, Minnesota

Jefferson CW, Thomas DJ, Gandhi SS, et al (2007) Unconformity-associated uranium deposits of the Athabasca basin, Saskatchewan and Alberta. Bull Geol Surv Canada 23–67

Li Z, Chi G, Bethune KM, et al (2018) Numerical simulation of strain localization and its relationship to formation of the Sue unconformity-related uranium deposits, eastern Athabasca Basin, Canada. Ore Geol Rev 101:17–31. doi: 10.1016/j.oregeorev.2018.07.004

Manning CE, Ingebritsen SE (1999) Permeability of the continental crust: Implications of geothermal data and metamorphic systems. Rev Geophys 37:127–150. doi: 10.1029/1998RG900002

McCuaig TC, Hronsky JMA (2014) The Mineral System Concept: The Key to Exploration Targeting. Build Explor Capab 21St Century 153–175

Mercadier J, Annesley IR, Mckechnie CL, et al (2013) Magmatic and metamorphic uraninite mineralization in the western margin of the Trans-Hudson Orogen (Saskatchewan, Canada): A uranium source for unconformity-related uranium deposits? Econ Geol 108:1037–1065. doi: 10.2113/econgeo.108.5.1037

Rutqvist J, Stephansson O (2003) The role of hydromechanical coupling in fractured rock engineering. Hydrogeol J 11:7–40. doi: 10.1007/s10040-002-0241-5

The uranium metallogeny in the South Armorican detachment zones, Variscan belt, France: geology, tracing (in space and time), numerical modelling

Philippe Boulvais[1], Marc Poujol[1], Yannick Branquet[1,2], Nathan Cogné[1], Thibault Duretz[1]
[1]Géosciences Rennes-UMR 6118, University of Rennes, France
[2]University of Orléans, France

Christophe Ballouard
Department of Geology, University of Johannesburg, South Africa

Romain Tartèse
The University of Manchester, School of Earth and Environmental Sciences, UK

Camille Dusséaux, Aude Gébelin
The University of Plymouth, School of Geography, Earth and Environmental Sciences, UK

Abstract. Uranium mineralization is common in geological environments where oxidized uranium-bearing fluids interact with reduced lithologies. This was the case for Variscan detachments in the South Armorican Massif, France. Numerous syn-tectonic peraluminous granites were emplaced in the footwall of detachments during the Carboniferous. Surface-derived fluids infiltrated the detachment planes and leached out the uranium from the magmatic uraninite that crystallized in these granites at the end of magmatic differentiation. On their way back to the surface, these fluids interacted with reducing black schists, which triggered precipitation of hydrothermal uraninite. This conceptual model serves as a basis for thermal-hydraulic-mechanical modeling.

Introduction

Detachments are syn- to -post-orogenic, crustal-scale extensional shear zones. The lower crust is exhumed at their footwall, and the upper crust is stretched at their hangingwall. Numerous fluid circulations are documented in these detachments, originating from deep crustal levels up to the Earth surface. Detachments also control the emplacement of syn-tectonic granites and the geometry of sedimentary basins. Most of these syn-tectonic granites form from partial melting of crustal sources, and, as such, are enriched in Large Ion Lithophile and High Field Strength elements, among which uranium. Where magmatic differentiation was sufficiently advanced in peraluminous granitic liquids, uranium may have reached contents large enough to crystallize uraninite. Detachment zones are thus the place where reduced uranium in crystallizing granite may interact with oxygenated aqueous fluids derived from the surface.

This situation occurred at the end of the Variscan orogeny in the south Armorican Massif, western France. In this contribution, we present a general model of uranium mobilization from fertile granites by surface-derived fluids followed by uranium precipitation where these fluids interacted with reducing lithologies. The conceptual model presented here serves as a basis for a thermal-hydraulic-mechanical numerical modeling.

2 Regional geology

The Armorican Massif is divided in three domains separated by two dextral crustal-scale shear zones, the North (NASZ) and South (SASZ) Armorican Shear Zones that were active during the Carboniferous (Gumiaux et al. 2004). The Central Armorican Domain is mostly made of weakly deformed and low-grade sediments of Neoproterozoic to Carboniferous ages.The south Armorican Domain is made of high grade metamorphic rocks, including migmatites, and crustal-derived peraluminous granites. Migmatites have been exhumed due to vertical displacements along the detachment zones from ca. 310 to 310 Ma while the South Armorican Shear zone was also active (Tartèse et al. 2011, 2012, 2013; Ballouard et al., 2015; Gapais et al. 2015). Numerous syn-tectonic highlyperaluminous two-mica leucogranites were emplaced within the SASZ and detachments. Several metal deposits, mainly Sn and U mineralization (Chauris 1977), are spatially associated with the peraluminous leucogranites. Uranium represents the most important resource in the region and has been mined within the three uraniferous districts of Pontivy, Mortagne and Guérande (Ballouard et al. 2017, 2018; Cathelineau et al. 1990; Cuney et al. 1990).

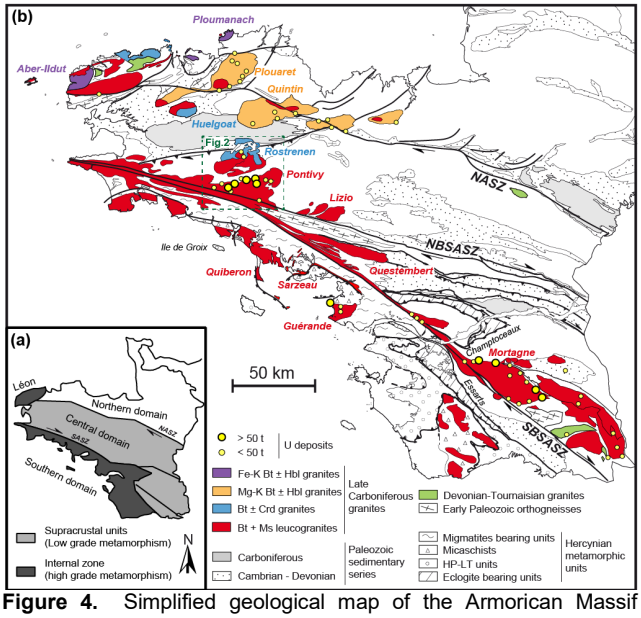

Figure 4. Simplified geological map of the Armorican Massif highlighting the Carboniferous granites, the detachment zones (Quiberon and Guérande), and the location of uranium deposits (yellow circles).

Field observations

The most interesting outcrops showing the syn-tectonic granites emplaced in detachment zones are located along the coastline, near Quiberon and Guérande (Fig. 1).

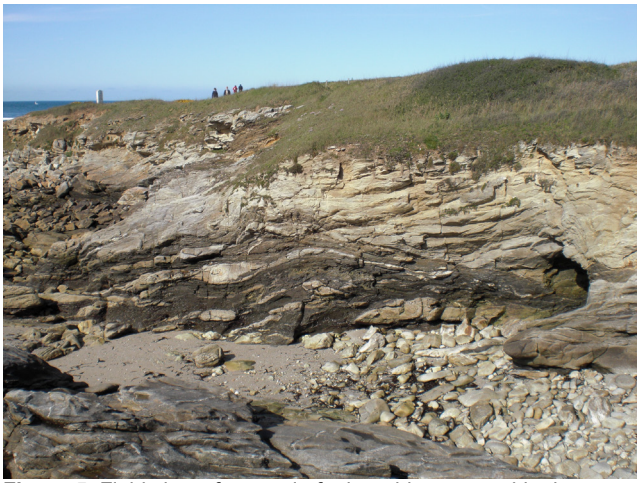

Figure 5. Field view of a panel of micaschist wrapped in the upper levels of the Quiberon granite. The foliation is dipping toward the West (left side of the picture).

Both the Guérande and Quiberon granites display a strain gradient with deformation increasing toward the top of the detachment zone footwall.

In the Quiberon granite, the width of the deformed zone reaches tens of meters. The strain pattern is rather heterogeneous, with deformation being localized in syn-tectonic pegmatites transposed into the foliation (Gapais and Laouan Brem Boundi 2015), leaving volumes of granites much less deformed. Where granite is more homogeneous, typical C/S structure developed.

In the Guérande granite (Fig. 3), a kilometric scale strain gradient is visible towards the detachment zone. Decametric normal faults cut the ductile fabric; this is clearly visible between the cities of Piriac and La Turballe (Fig. 3). The resulting graben-like structure exposes country rocks, comprised of metavolcanic rocks of Ordovician age and black schists. .

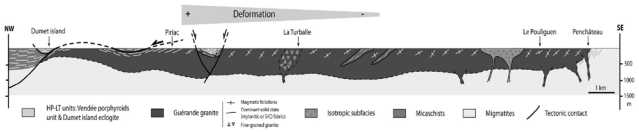

Figure 3. Schematic cross-section of the Guérande granite showing an increase of the strain gradient toward the detachment zone to the NW, and the location of a graben between Piriac and La Turballe.

4 Magmatic differentiation vs. hydrothermal alteration

In the Guérande leucogranite (Ballouard et al. 2015, 2017), magmatic and magmatic-hydrothermal differentiation progressed toward the apical zone of the intrusion, namely toward the detachment. There, tourmaline-bearing highly peraluminous granites reach extremely high content in highly incompatible hygromagmaphile elements such as Sn, Cs and Rb but are paradoxically depleted in U compared to the biotite-bearing samples from the deeper levels of the intrusion. Also, the oxygen isotope composition of the apical samples is lowered by several per mil compared to unaltered samples (Ballouard et al. 2017). This peculiar signature is interpreted to reflect an influx of meteoric water as also supported by low hydrogen isotope ratios of syntectonic muscovite in the upper part of detachment footwalls (Dusséaux et al. in press).

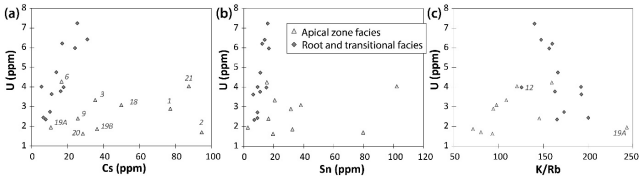

Figure 6. Bivariant diagrams showing that uranium is well correlated with highly incompatible elements for samples from the deep parts of the Guérande granite, and deoupled from them in the apical parts of the intrusion.

The petrographic characterization of the Quiberon granite is currently in process. First results show that the granite close to the detachment is more evolved than the deeper levels. Interestingly, the hydrothermal alteration seems well recorded by apatite grains (Fig. 5).

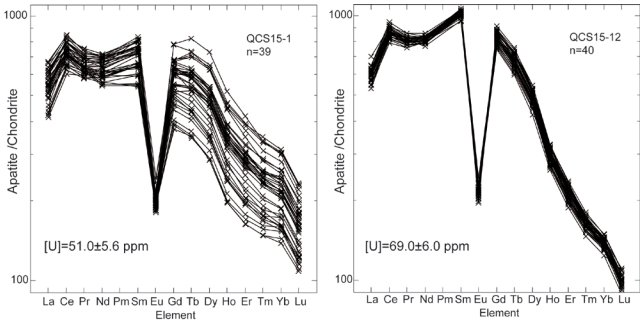

Figure 5. Chondrite-normalized REE patterns of apatite grains from the Quiberon granite. To the left, the sample is deformed; to the right, the sample is undeformed. The uranium content is lower in the deformed, and altered, sample. Note also that the U-Pb age of the deformed facies is 10 Ma younger than the undeformed one.

As a summary, the petrological and geochemical characteristics of syn-tectonic granites emplaced in the footwall of detachment are as follows: the most evolved facies and the most altered facies are those emplaced in the higher structural levels of intrusions, close to detachments. Hydrothermal alteration thus affected the most differentiated granitic rocks.

5 Uranium mineralization

The Guérande granite is the only hosts of uranium mineralization. The main mineralization occurs in a fault zone of the graben affecting the apical zone of the granite. There, quartz-uranium oxide bearing veins crosscut the foliation of metavolcanics rocks and are blocked at the contact with black shales (Cathelineau 1981). The age of mineralization is somewhat variable, and comprised between the age of the last magmatic events (around 300 Ma) and Permian times (around 270 Ma; Ballouard et al. 2017).

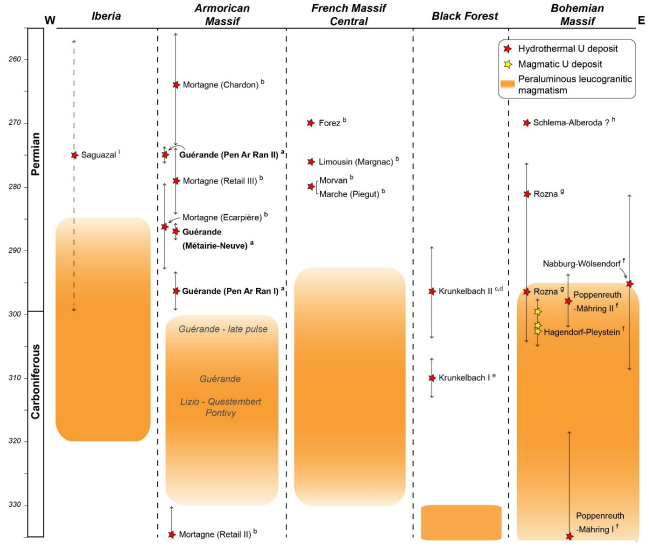

Figure 6. Chronological sequence comparing the timing of U mineralization in the Variscan belt and the emplacement ages of the associated granites.

It is thus clear that uranium mineralization immediately follows magmatic activity; this relationship is also visible for several other magmatic systems in the Variscan belt (Fig. 6).

From all these observations, a conceptual model of uranium mineralization has been derived (Fig. 7; Ballouard et al. 2017). Fertile granites emplaced below detachment zones. Magmatic differentiation promoted magmatic uraninite crystallization in the apical zone of the granites. The flow of surface-derived fluids induced leaching of uranium from magmatic uraninite. On their way back to the surface along permeable pathways, such as steeply dipping normal faults that control the geometry of the graben in the Guérande granite, these fluids interacted with reducing lithologies (black schists), which triggered precipitation of hydrothermal uraninite.

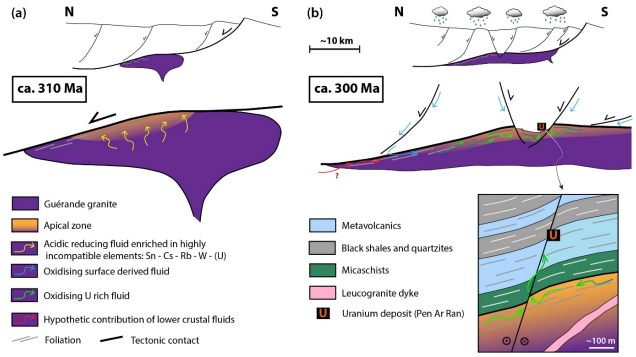

Figure 7. Conceptual model of uranium mineralization associated with granitic magmatism at the footwall of Variscan detachment zones (Ballouard et al. 2017).

6 Numerical modeling

Such a heuristic conceptual model can be tested through hydro-thermal simulations accounting for darcyan flow. Preliminary simulations have been realized in order to test and combine the effect of different driving forces for fluid flow (e.g. thermal convection, topographic gradient). The permeability of the detachment is assumed to be temperature-dependent. This relationship was designed by analogy with ductile rheology, which is at first order controlled by the temperature. The first results indicate that (i) pluton emplacement and cooling are unfavorable periods for infiltration of surface-derived fluids along detachment. Topographic gradients have to develop in order to create strong pressure gradients that can counterbalance thermal convection triggered by magmas; (ii) after cooling of the pluton, uplift and erosion, the pluton apical zone (source of U, Fig. 7) is in the brittle field strain which implies higher permeabilities along the neighbouring detachment segment. Here, in this internal zone of the Variscan belt, topographic gradients were large enough to promote downward flow circulation of fluids that could be responsible for supplementary cooling (Fig. 8). A next step in the modeling will consist in integrating solute transfer equation for U flux and mass balance calculation. In addition, future models will account for the role of solid rock deformation on the patterns of fluid circulation. Brittle and ductile deformations have different impacts

on the distribution of permeability. Detachments thus appear as ideal geological objects to study the role of hydro-thermo-mechanical processes on the genesis of mineralizations.

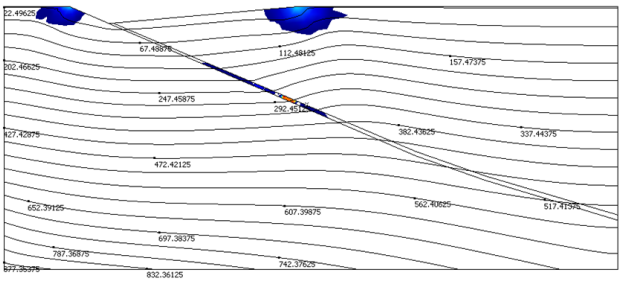

Figure 8. Snapshot of a detachment model with thermal convection and topography as driving forces. Advective downward flow of surface-derived fluids is efficient to cool down deeper parts of the detachment.

7 Conclusion

In the southern part of the Armorican Massif, Variscan Belt (France), detachment zones worked during the late Carboniferous. In this context, lower crustal units were exhumed, syn-tectonic peraluminous granites emplaced in the footwall of these structures and downward infiltration of meteoric fluids occurred. Magmatic differentiation of the peraluminous granites led to the crystallization of magmatic uraninite. This crystal was leached through the interaction with oxidized surface-derived fluids. These fluids were then focused on high-permeability zones, like the steeply dipping normal faults associated with the regional extension. Where the faults crosscut black schists in the haningwall of the detachment, uranium precipitation occurred as hydrothermal uranitite. This conceptual model allows building the set up for a dedicated thermo-hydro-mechanical numerical modeling.

Acknowledgements

We would like to thank the PF NEEDS for funding the development of the numerical aspect of this research. Fieldwork, petrological, geochemical and geochronological analyses were possible thanks to various funding to PB and MP.

References

Ballouard C, Boulvais P, Poujol M, Gapais D, Yamato P, Tartèse R, Cuney M (2015) Tectonic record, magmatic history and hydrothermal alteration in the Hercynian Guérande leucogranite, Armorican Massif, France. Lithos 220–223:1–22.

Ballouard C, Poujol M, Boulvais P, Mercadier J, Tartèse R., Venneman T, Deloule E., Jolivet M, Kéré, I, Cathelineau M, Cuney, M (2017) Magmatic and hydrothermal behavior of uranium in syntectonic leucogranites: The uranium mineralization associated with the Hercynian Guérande granite (Armorican Massif, France). Ore Geol Rev 80:309-331.

Ballouard C, Poujol M, Mercadier J, Deloule E, Boulvais P, Baele JM, Cuney M, Cathelineau M (2018) Uranium metallogenesis of the peraluminous leucogranite from the Pontivy-Rostrenen magmatic complex (French Armorican Variscan belt): the result of long-term oxidized hydrothermal alteration during strike-slip deformation. Min Dep 53 :601–628.

Cathelineau M (1981) Les Gisements Uraniferes de la Presqu'ile Guerandaise (Sud Bretagne); Approche Structurale et Metallogenique. Min Dep 16 :227–240.

Cathelineau M, Boiron MC, Holliger P, Poty B (1990). Metallogenesis of the French part of the Variscan orogen. Part II: Time-space relationships between U, Au and Sn-W ore deposition and geodynamic events — mineralogical and U-Pb data. Tectonophysics 177:59–79.

Cuney M, Friedrich M, Blumenfeld P, Bourguignon A, Boiron MC, Vigneresse JL, Poty B (1990) Metallogenesis in the French part of the Variscan orogen. Part I: U preconcentrations in pre-Variscan and Variscan formations — a comparison with Sn, W and Au. Tectonophysics 177 :39–57.

Chauris, L., 1977. Les associations paragenetiques dans la metallogenie varisque dumassif armoricain. Min Dep 12:353–371.

Dusséaux, C., Gébelin, A., Boulvais, P., Gardien, V., Grimes, S., Mulch, A. (in press) Meteoric fluid-rock interaction in Variscan shear zones. Terra Nova.

Gapais D, Brun JP, Gumiaux C, Cagnard F, Ruffet G, Le Carlier De Veslud C (2015) Extensional tectonics in the Hercynian Armorican belt (France). An overview. Bull Soc Geol Fr 186:117–129.

Gapais D, Laoun Brem Boundi A (2015) Pegmatite mylonites: origin and significance. Geol Soc, London, Special Publications, 409:167–173.

Gumiaux C, Gapais D, Brun JP, Chantraine J, Ruffet G (2004) Tectonic history of the Hercynian Armorican Shear belt (Brittany, France). Geodyn Acta 17:289–307.

Tartèse R, Ruffet G, Poujol M, Boulvais P, Ireland T (2011) Simultaneous resetting of the muscovite K-Ar and monazite U-Pb geochronometers: a story of fluids. Terra Nova 23:390-398.

Tartèse R, Boulvais P, Poujol M, Chevalier T, Paquette JL, Ireland TR, Deloule E (2012) Mylonites of the South Armorican Shear Zone: insights for crustal-scale fluid flow and water–rock interaction processes. J Geodyn 56–57:86–107.

Tartèse R, Boulvais P, Poujol M, Gloaguen E, Cuney M (2013) Uranium mobilization from theVariscan Questembert syntectonic granite during fluid-rock interaction at depth. Econ Geol 108:379–386.

Cyclical development of roll front-type uranium deposits

Christophe Bonnetti
State Key Laboratory breeding base of nuclear resources and environment, East China University of Technology

Lingli Zhou, Thomas Riegler
iCRAG, School of Natural Sciences, Department of Geology, Trinity College Dublin, Ireland

Joël Brugger
School of Earth, Atmosphere and the Environment, Monash University, Australia

Abstract. In roll front (RF) deposits across the world, complex ore-stage pyrite textures associated with extreme changes in isotopic and trace element compositions reflect the dynamic internal evolution of the biogeochemical processes responsible for sulfate reduction, thus demonstrating the cyclical development of roll front systems. Upon percolation of oxidizing fluids into the reduced sandstones, RF systems become self-sufficient, with a systematic repetition of their activity cycle. Reducing-dominant conditions at the redox interface favor the formation of biogenic framboidal pyrite by bacterial iron and sulfate reduction ($\delta^{34}S$ from -30.5 to -12.5 ‰) and the genesis of the uranium mineralization. When the redox interface becomes oxidizing-dominant, RF systems enter in a translation stage characterized by the re-oxidation of reduced sulfur minerals inducing an increased supply of sulfate and metals in solution to the bacterial sulfate reduction (BSR) zone. Hence, this stage is marked by increased rates of the BSR associated with the crystallization of variably As-Co-Ni-Mo-enriched concentric pyrite with moderately negative $\delta^{34}S$ values. A final stage of pyrite cement with low trace element contents and heavier $\delta^{34}S$ signatures marks the end of the RF activity cycle and the transition from open to closed system behavior.

1 Introduction and geological setting

Sandstone-hosted RF type uranium deposits represent the most cost-effective type of uranium resource (30% of the world annual production; OECD-NEA-IAEA 2016), as they are amenable to in-situ recovery. Studies on roll front deposits from the U districts of Wyoming and South Texas, U.S.A; the Central Asia Uraniferous Province (CAUP) extending from Kazakhstan to North China; and Lake Frome Embayment, South Australia, show evidence for biogenic mechanisms for both sulfate reduction and uranium mineralization that were mediated by sulfate-reducing bacteria (SRB) (Fig. 1; Reynolds and Goldhaber 1982, 1983; Min et al. 2005; Cai et al. 2007; Ingham et al. 2014; Bonnetti et al. 2015a, 2015b, 2017, 2018; Lach et al. 2015). They also revealed that RF deposit ore-stage pyrites share remarkably similar evolution of their textures (i.e., early framboidal, followed by concentric overgrowth, and finally idiomorphic cement), with extreme variations in trace element and $\delta^{34}S$ signatures (i.e., from -72.0 to +32.4 ‰), up to the maximum theoretical value of sulfur isotope fractionation for microbial sulfate reduction (i.e., about -70 ‰; Brunner and Bernasconi 2005). To date, these features have been interpreted as reflecting protracted geological histories and multiple sources of S (e.g., Ingham et al. 2014). Strongly negative $\delta^{34}S$ values recorded in pyrite are an unambiguous indicator of bacterial sulfate reduction (BSR) producing reduced sulfur species (H_2S, HS^-; Machel 2001) that are strongly enriched in ^{32}S (i.e., isotopically light) compared to the initial sulfate (Habicht and Canfield 1997; Brunner and Bernasconi 2005). Pyrite also incorporates a number of trace elements; uptake is controlled by a combination of equilibrium (P, T, solubility composition) and kinetic processes (Large et al. 2009; Morin et al. 2017). Recent experimental and numerical modeling studies (e.g., Druhan et al. 2014) have demonstrated that large variations in $\delta^{34}S$ values (-4 to +12 ‰ in experiments; up to +30 ‰ in the model) of bisulfide formed via BSR occur during steady injection of nutrient- and sulfate-bearing water through a meter-long sediment column over 43 days. Such a steady flow of oxidized waters defines an open system that closely matches the well-accepted model for roll front deposit formation.

Here, we demonstrate that a dynamic BSR-driven model explains the distribution of S isotopes and trace elements in RF system ore-stage pyrites. We show for the first time that the observed complexity of pyrite signatures reflects the successive stages characterizing the activity cycle of uranium RF systems and their biogeochemical internal dynamic setting, rather than external forcing and multiple element sources. The variations in the signatures of ore-stage pyrites, interpreted as a continuum reflecting the evolution of the processes responsible for RF ore genesis, were examined based on the study of ore-stage pyrites from the Bayinwula deposit, a typical RF uranium deposit located in the southeastern part of the CAUP (Bonnetti et al. 2015b, 2017).

The Mesozoic sedimentary basins of northeast China and southeast Mongolia (e.g., the Ordos, Erlian, Songliao and East Gobi basins) host numerous RF deposits (Cai et al. 2007; Bonnetti et al. 2015b, 2017). RF deposits in the Erlian Basin are mostly hosted by confined reduced braided river sandstones (Bonnetti et al. 2015b). The Bayinwula deposit, located in the north of the Basin, is characterized by disseminated P-rich coffinite, ningyoite and pitchblende in association with

ore-stage pyrite, inherited organic matter (OM) and altered Fe-Ti oxide.

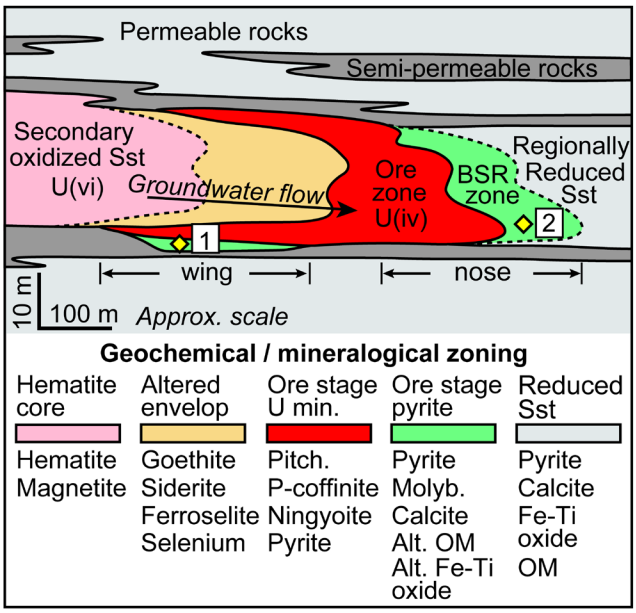

Figure 1. Model section with geochemical and mineralogical zoning of the Bayinwula deposit (modified from Devoto 1978; Bonnetti et al. 2015b). The yellow diamonds indicate the location of the two representative samples used for the study. BSR = bacterial sulfate reduction; Sst = sandstone; Approx. = approximate; U min. = uranium mineralization; Pitch. = pitchblende; Molyb. = molybdenite; Alt. = altered.

2 Material and methods

As the signature evolution of ore-stage pyrites that defines the model presented in this study occurs at the mineral scale, we selected two samples for detailed characterization. These samples were selected based on the detailed geochemical and mineralogical study conducted by Bonnetti et al. (2015b) on the Bayinwula deposit from an extensive sample set comprising sixty-three samples collected on several drill holes distributed along a profile oriented perpendicular to the main geochemical/mineralogical zoning of the deposit. These two samples represent the wing and nose of the deposit (Fig. 1); they are representative of the signatures observed throughout the deposit and display the most complete paragenetic relationships of ore-stage pyrite populations.

Ore-stage pyrite populations from the Bayinwula deposit were characterized by: (i) petrographic observations using a reflected-light optical microscope and a Scanning Electron Microscope (SEM), (ii) in situ mineral analysis using an Electron Microprobe Micro-Analyzer (EPMA) to determine their major and minor elements chemical composition and high-resolution trace element mapping by Laser Ablation Inductively-Coupled-Plasma Mass-Spectrometry (LA-ICP-MS), and (iii) in situ measurements of sulfur isotopes by Secondary Ion Mass Spectrometry (SIMS).

3 Results

3.1 Morphology and texture

Ore-stage pyrites were formed in the pyrite zone (Fig. 1), identified as the BSR zone by Bonnetti et al. (2015b), either located at the nose or at the wings of the RF. Ore-stage pyrite morphologies display the following sequence of crystallization: (i) framboidal, (ii) concentric overgrowth and (iii) sub-idiomorphic to idiomorphic cement (Fig. 2a-a). Clusters of authigenic framboidal pyrite, predominantly replacing OM fragments and Fe-Ti oxides, are the most widespread type of pyrite observed in the BSR zone. The concentric pyrite forms overgrowth rims around the framboids in either colloform or idiomorphic textures. The framboids and the concentric overgrowth were both cemented by a final stage of sub-idiomorphic to idiomorphic pyrite. These three generations of pyrite were then partly to totally replaced by uranium minerals that occur in the ore zone (Fig. 1) during the downward translation of the RF (Bonnetti et al. 2015b). In the oxidized sandstone, ore-stage pyrites were re-oxidized into hematite or limonite by fresh batches of oxygenated groundwater.

3.2 Trace element distribution in pyrite

LA-ICP-MS trace element maps of As, Ni, Co and Mo revealed highly contrasted compositions of ore-stage pyrites (Fig. 2). As a general trend, the trace element contents of pyrite located at the nose of the RF are one order of magnitude higher than pyrite from the wings. At the wings, the framboids have low to high concentrations of As, Ni and Co (10's to 1000's of ppm) but relatively low Mo content (< 100 ppm; Figs. 2c-c to f). The first rim(s) of concentric pyrite has almost systematically higher Ni, Co, Mo and in particular As contents (10's to 1000's of ppm) relative to the framboids (Fig. 2c-a). Moving outwards, the concentric pyrite shows variable and rim-dependent As, Ni, Co and Mo contents, but generally the most abundant for the first rim (Fig. 2c-a). The final stage of pyrite cement is low in As, Ni and Co (several ppm to 100's of ppm) but can contain moderate Mo concentrations (up to 500 ppm) locally. At the nose of the RF, the variations of trace element concentrations in the three populations of pyrite are similar to pyrites at the wings. However, here the framboids and the concentric pyrite have moderate to very high concentrations of Ni, Co and Mo (100's to 10,000's of ppm), and especially high As contents (to 50,000 ppm). The higher trace element concentrations in pyrite from the nose compared with pyrite from the wings is mainly related to higher permeability of the host sediment at the nose (Fig. 1), hence more fluid-mobile trace metals transported by the fluid will be concentrated at the nose.

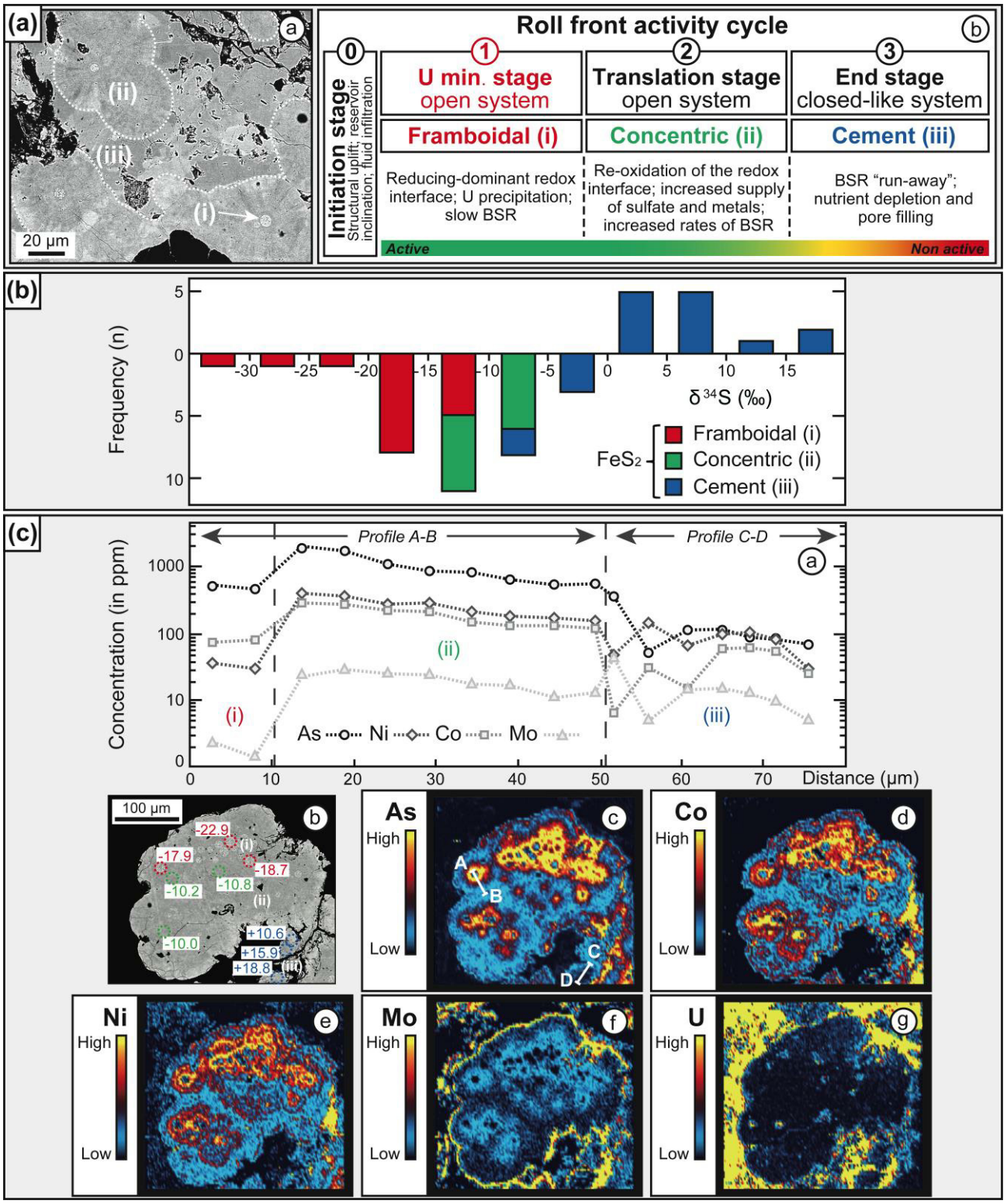

Figure 2. Petrographic, chemical and isotopic signatures of ore-stage pyrites characterizing the activity cycle of the Bayinwula roll front deposit. (**a**) Development of roll front deposits. (a) Back-scattered electron (BSE) image of the three ore-stage pyrite populations in the Bayinwula deposit (sample 1). (i) = framboidal, (ii) = concentric, (iii) = cement; (b) The main stages of the roll front activity cycle. BSR = bacterial sulfate reduction; SRB = sulfate-reducing bacteria. (**b**) Sulfur isotopes signature of ore-stage pyrites (modified from Bonnettic et al., 2015). (**c**) Trace element concentrations in ore-stage pyrites. (a) LA-ICP-MS profile (AB-CD) showing the evolution of concentrations in As, Ni and Co from framboidal to cement pyrite; (b) BSE image of the mapped pyrite zone from sample 1. Annotated values correspond to $\delta^{34}S$ in ‰; (c-f) LA-ICP-MS semi-quantitative element maps showing the distribution of trace element concentrations (As, Co, Ni, Mo) in ore-stage pyrites; (g) LA-ICP-MS semi-quantitative element map showing the distribution of uranium concentration/mineralization associated with ore-stage pyrites.

3.3 Sulfur isotopes signatures

The $\delta^{34}S$ signatures for the three ore-stage pyrites measured from samples throughout the deposit range from -30.5 to +18.8 ‰ (Fig. 2B): (i) the framboids have a very light signature ranging from -30.5 to -12.5 ‰ (mean -18.4 ‰), (ii) the concentric overgrowth presents moderately negative values ranging from -13.7 to -7.5 ‰ (mean -9.6 ‰), and (iii) the late stage of pyrite cement has a heavier signature from -6.9 to +18.8 ‰ (mean +4.0 ‰).

4 Discussion and conclusions

The well-accepted model for RF deposits involves formation of a translating redox interface under the influence of oxidizing groundwater flow within a confined, reduced aquifer. Based on ore-stage pyrite signatures from the Bayinwula deposit, we propose for the first time that the complex textural, chemical, and isotopic signatures observed in ore-stage pyrite from RF deposits are a directed result of the dynamic, continuous and cyclical nature of these systems, which generally form from a single fluid. The biogenically driven evolution of sulfate reduction at the redox interface defines their activity cycle, which can be subdivided into four main stages (Fig. 6a-b): (0) the initiation stage, (1) the mineralization stage, (2) the translation stage and (3) the end stage. Upon percolation of oxidizing meteoric water, RF systems become self-sufficient in their development with a repetition of the sequence Stage (1) to (3) for each new influx of oxidizing groundwater, until the reservoir is completely oxidized, or major tectonic uplifts disrupt the system. The cyclical development of roll front deposits is characterized by alternating reducing and oxidizing conditions at the redox interface and transitional open to closed system behavior. In this context, ore-stage pyrite signatures in RF systems reflect the internal dynamic evolution of the biogeochemical processes responsible for sulfate reduction with sulfur derived from a single source, rather than externally driven changes in fluid or sulfur sources through time. The remarkable wide range of their chemical and isotopic signatures recorded during roll front activity cycles originated from BSR-mediated extreme S isotopes and trace elements fractionation.

Acknowledgements

Funding was provided by the National Natural Science Foundation of China (Grant number: 41750110482). We thank Cora McKenna for her kind collaboration during the LA-ICP-MS data acquisition.

References

Bonnetti C, Cuney M, Malartre F, Michels R, Liu X (2015a) The Uranium Metallogenic Cycle in the Intracontinental Erlian Basin, NE China: From Source to Deposit. Proceedings of the 13th SGA biennial meeting: “Mineral resources in a sustainable world”, Nancy, France.

Bonnetti C, Cuney M, Michels R, Truche L, Malartre F, Liu X, Yang J (2015b) The multiple roles of sulfate-reducing bacteria and Fe-Ti oxides in the genesis of the Bayinwula roll front-type uranium deposit, Erlian Basin, NE China. Econ Geol 110: 1059-1081

Bonnetti C, Liu X, Zhaobin Y, Cuney M, Michels R, Malartre F, Mercadier J, Cai J (2017) Coupled uranium mineralisation and bacterial sulphate reduction for the genesis of the Baxingtu sandstone-hosted U deposit, SW Songliao Basin, NE China. Ore Geol Rev 82:108-129

Bonnetti C, Zhou L, Riegler T, Brugger J (2018) New visions in the genesis of roll front uranium deposits. Goldschmidt Abstracts, 2018 231

Brunner B, Bernasconi S (2005) A revised isotope fractionation model for dissimilatory sulphate reduction in sulphate reducing bacteria: Geochim Cosmochim Acta 69:4759-4771

Cai C, Li H, Qin M, Luo X, Wang F, Ou G (2007) Biogenic and petroleum-related ore-forming processes in Dongsheng uranium deposit, NW China. Ore Geol Rev 32:262-274

Devoto RH (1978) Uranium in Phanerozoic sandstone and volcanic rocks: Short course in uranium deposits; their mineralogy and origin. Mineralogical Association of Canada, Short Course Handbook 3:293-305

Druhan JL, Steefel CI, Conrad ME, DePaolo DJ (2014) A large column analog experiment of stable isotope variations during reactive transport: I. A comprehensive model of sulfur cycling and δ34S fractionation. Geochim Cosmochim Acta 124:366-393

Habicht KS, Canfield DE (1997) Sulfur isotope fractionation during bacterial sulfate reduction in organic-rich sediments. Geochim Cosmochim Acta 61:5351-5361

Ingham ES, Cook NJ, Cliff J, Ciobanu CL, Huddleston A (2014) A combined chemical, isotopic and microstructural study of pyrite from roll-front uranium deposits, Lake Eyre Basin, South Australia. Geochim Cosmochim Acta 125:440-465

Lach P, Cathelineau M, Brouand M, Fiet N (2015) In-situ isotopic and chemical study of pyrite from Chu-Sarysu (Kazahkstan) roll-front uranium deposit. Procedia Earth Planet Sci 13:207-210

Large RR, Danyushevsky L, Hollit C, Maslennikov V, Meffre S, Gilbert S, Bull S, Scott R, Emsbo P, Thomas H, Singh B, Foster J (2009) Gold and Trace Element Zonation in Pyrite Using a Laser Imaging Technique: Implications for the Timing of Gold in Orogenic and Carlin-Style Sediment-Hosted Deposits. Econ Geol 104:635-668

Machel HG (2001) Bacterial and thermochemical sulphate reduction in diagenetic settings – old and new insights. Sediment Geol 140:143-175

Min MZ, Xu MH, Chen J, Fayek M (2005) Evidence of uranium biomineralization in sandstone-hosted roll-front uranium deposits, northwestern China. Ore Geol Rev 26:198-206

Morin G, Noël V, Menguy N, Brest J, Baptiste B, Tharaud M, Ona-Nguema G, Ikogou M, Viollier E, Juillot F (2017) Nickel accelerates pyrite nucleation at ambient temperature. Geochem Perspectives Lett 5:6-11

OECD-NEA/IAEA (2016) Uranium 2016: Resources, Production and Demand: OECD, Paris, 508 p

Reynolds RL, Goldhaber MB (1982) Biogenic and nonbiogenic ore-forming processes in the South Texas uranium district: evidence from the Panna Maria deposit. Econ Geol 77:541-556

Reynolds RL, Goldhaber MB (1983) Iron disulfide minerals and the genesis of roll-type uranium deposit. Econ Geol 78:105-120

Methaniferous active faults and seismic cycle in the genesis of the Athabasca giant U deposits: conceptual and numerical investigation

Yannick Branquet[1], Philippe Boulvais[2], Julien Mercadier[3], Patrick Ledru[4], Charles Khairallah[4]
[1]ISTO UMR 7327, University of Orléans, CNRS, BRGM, France
[2]Géosciences Rennes-UMR 6118, University of Rennes, CNRS, France
[3]Université de Lorraine, CNRS, CREGU, GeoRessources Lab., Campus Aiguillettes, Faculté des Sciences et Technologies, France
[4]Orano Canada., Canada

Abstract. The reduction process of uranyles and the graphitic faults dynamics are still unconstrained in the formation of giant unconformity-related uranium deposit of Athabasca. Previous and new data on graphitc faults and mineralization are suggestive of paleo-seismicity, possibly during the mineralizing event. Highlighted by data from current active methaniferous fault, we proposed a new model based on seismic cycle for that mineralization, implying seismic pumping, methane production and discharge. Numerical modeling shows that consequences are of first order on paleo-hydrodynamics.

1 Introduction

The Athabasca Paleo- to Mesoproterozoic basin in northern Saskatchewan hosts the largest reserves of high-grade unconformity-related uranium deposits in the world. The major U deposits from the eastern part of the basin (e.g. Mc Arthur, Cigare Lake) are located at the intersection between graphitic shear zones and faults (GSZF) within the basement and the basal unconformity, frequently in the apical zone of basement structural highs. The GSZF are inherited from the Trans-Hudsonian orogen (ca. 1800-1720 Ma) and are localized where Paleoproterozoic carbonaceous sediments have been buried, deformed and metamorphosed between orthogneisses slices during thickening and tectonic escape at crustal scale (Jeanneret et al., 2016)

Updated metallogenic models postulate that (Fig. 1): (i) concerning U source-extraction, the mineralizing fluids were brines, derived from primary brines issued from seawater evaporation. These brines percolated in the Trans-Hudsonian basement and leached U from U-bearing bearing minerals like monazite. The infiltration of brines was favored by an high-permeability paleo-weathering horizon at the top of the basement; (ii) concerning U trap-deposit, driven by free convection within the basin/basement interface, reduction of uranyles-bearing brines and precipitation of UO_2 occurred in spatial relation with GSZF. Mineralization occurred at 120-200°C and under fluid pressure close to hydrostatic regime below a maximum basin thickness of about 5-6 km (Pagel, 1975; Hoeve and Sibbald, 1978; Richard et al., 2013). Duration of a single mineralizing event is about 0.1-1 Myrs (Richard et al., 2012); (iii) primary mineralization events were post Athabasca sedimentation and spanned at least the 1600-1300 Ma period during uplift, tilting and unroofing of the basin (Jefferson et al., 2007)

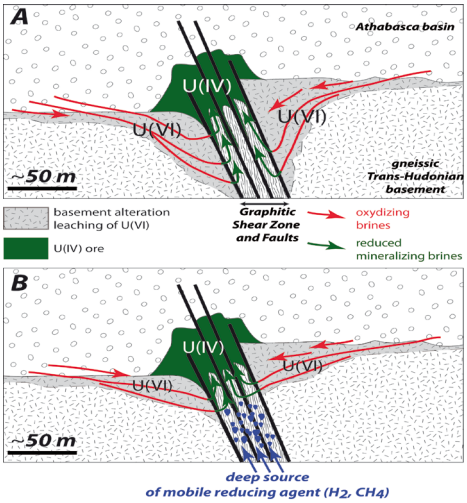

Figure 1. Simplified metallogenic models of Athabasca unconformity-related uranium deposits (modified from compilation of Martz, 2017 and references therein).

At least two major points still deserve better understanding: (i) The reducing agent and process for uranyles is not clearly identified. In fluid inclusions, traces of methane have been measured (Derome et al., 2003); methane has been therefore proposed as a possible reducing agent. Also, whether the reducing agent, like methane, was derived from “internal” sources, through the reaction between the infiltrated brines and a local reducing lithology (graphite precursor, sulfides… Derome et al., 2005; Fig. 1a) or corresponded to the upward flow of a deeply-originated “external” reducing fluid, (Dargent et al., 2015, Fig. 1b), is a matter of debate (Fig. 1); (ii) Although recognized as a major exploration guide (e.g. conductors), little is known about the mechanical behavior and fluid flow dynamics of GSZF within the basement, particularly during the mineralizing events.

Here, we address these two points. We compile and present recent data allowing discussing the dynamics of the GSZF to better understand their role in the metallogeny of uranium. In the light of the studies

dedicated to methaniferous active faults, we propose a new conceptual model for the Athabasca-like giant U deposits involving a seismic cycle for the GSZF and the influx of externally-derived methane. Thereafter, we develop numerical hydro-thermal simulations to test this mechanism and discuss the implications on paleo-hydrodynamics of the mineralizing system

2 Dynamics of graphitic shear zones and faults (GSZF)

2.1 Overview through geological times

The graphitic shear zones and faults (GSZF) are distributed following an anastomosing pattern of steeply dipping structures within the basement (Jeanneret et al., 2016). Since the Trans-Hudsonian ductile shearing HT metamorphic conditions, the GSZF have had a long-lasting history as they record multiple brittle reactivations (Jefferson et al., 2007; Martz, 2017): (i) during the late Trans-Hudsonian orogen exhumation and uplift. Graphite enrichment of the faults is supposed to have occurred at this stage through precipitation of hydrothermal graphite; (ii) during the Athabasca basin deposition and subsidence (not well documented); (iii) durin the basin border “inversion” uplift and unroofing through reverse faulting, a period corresponding to the main mineralization stage (between ca. 1600 and 1300, Alexandre et al., 2007); (iv) during multiple post-Athabasca reactivation increments depicted through late U mineralization and remobilization events (up to 200 Ma at Cigar Lake; Martz, 2017). The successive reactivations of the GSZF resulted in basement highs associated with reverse offsets (Fig. 2a) as frequently observed for major U deposits (e.g. McArthur). Therefore, the GSZF represent weak inherited crustal structures which have been reactivated several times during late and Post Trans-Hudsonian events.

2.2 Structural and textural fingerprint, links with the mineralization

From damage zone to fault core, fault-rocks present nearly all the textural facies produced by cataclastic flow (Fig. 2b). In the graphite-rich fault core foliated ultracataclasites display rounded clasts in a gouge matrix composed of fine-grained white micas, crushed carbonaceous material, pyrite and quartz (Fig. 2c, d). Timing of that cataclastic flow is attributed to late Trans-Hudsonian brittle reactivation and exhumation near 450°C coeval with hydrothermal graphite precipitation (Martz et al., 2017).

Some GSZF are mineralized, some are not. In a fertile GSZF with various aligned branches, the ore bodies are restricted to few segments. Ore is basically massive and/or disseminated but is also present in veins (Khairallah, 2017) in fault damage zone. Primary ore is abundantly reworked, fractured, and brecciated by sulfides and secondary U deposition.

During the mineralization stage at Cigar Lake, Martz et al. (2018) demonstrate that mineralizing brines percolated within the GSZF by re-opening of previous cracks during a bulk brittle reactivation of the faults. They suggest that during this reactivation, methane traces detected in mineralizing brines fluid inclusions were issued from the release of former Late Trans-Hudsonian volatile-rich fluids responsible for hydrothermal graphite precipitation (from re-opened fluid inclusions or from desorption from minerals surfaces like chlorite). To summarize, GSZF were active during mineralization and part of the cataclastic flow observed (Fig. 2) is coeval with mineralizing brines circulation and methane mobility.

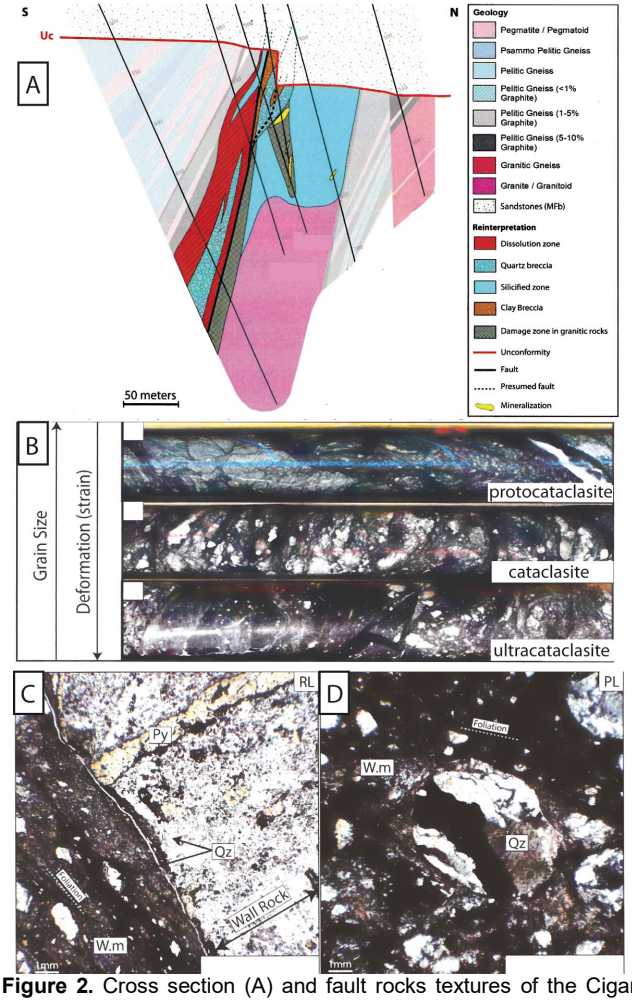

Figure 2. Cross section (A) and fault rocks textures of the Cigar North conductor (Cigar Lake trend, from Khairallah, 2017). Between fractured damage zones, the GSZF core present ultracataclasites (B) and foliated gouges (C) in a white micas matrix (W.m) supporting rounded clasts (D). Former hydrothermal graphite is reworked, crushed and brecciated in faults rocks.

The fact that GSZF were active does not imply that these structures were seismogenic during the mineralization history. Rowe and Griffith (2015) performed a detailed review of fault textures diagnostic of different slip rates over the course of the seismic cycle. Even though no pseudotachylite has been unequivocally identified in drill cores crossing GSZF, the zonation of fault-rocks types, the rounded clasts within a fined-grained matrix, the degree of tectonic comminution in foliated gouge (Fig. 2) are significant of high

(ultracataclasites) and low (protocataclasites) slip rates along active faults. Therefore, activity of GSZF during mineralization might record seismic cycles.

3 Lessons from current seismogenic methane seepage

Fluid venting, gas and specially methane cold seeps in seawater or sediments above active fault systems are known for a long time and currently receive much attention for seismic hazard monitoring/forecasting. Submarine dives and acoustic techniques indicate that seismogenic fault segments release more gas than non-seismic ones (Géli et al., 2008). Moreover, Gasperini et al. (2012) demonstrate that methane seepages are persistent (up to tens of years) after the seismic event. In those studies dealing with the Marmara Sea the methane is microbial in origin and derives from young sediments lying close to the seafloor. However, deeper methane reservoirs participating to seismic methane venting have also been identified (Geersen et al., 2016). In spite of those assessments, the dynamics of methane seeps and generally the fluid venting above active fault still remain unclear relatively to the seismic cycle itself.

4 A new conceptual model

The GSZF in the Athabasca systems were active, likely seismogenic, and in the meantime the locus of methane influx. We thus propose that U deposits of Athabasca may results from fossils seismogenic methane-rich flows along GSZF (Fig. 3).

Actually, the distribution of mineralized bodies itself, restricted to peculiar segments of the GSZF also argues for seismicity. Indeed, If hydrodynamics of the mineralizing brines was likely controlled by large convections cells (Li et al., 2016), this 3D mineralized pattern implies channeling of flow within reactivated high-permeable segments of GSZF. Among other explanations, the seismic failure of loaded segments of an active fault and its associated fluid discharge is a good candidate.

Two main sources of methane can be envisaged: (i) the thick GSZF are vertical fractured structures that can be viewed as reservoirs at depth with residual methane trapped in microcracks and/or adsorbed on phyllitic minerals. In the case permeability increased through seismic reactivation of GSZF would be quite similar to the effects of hydraulic fracturing used in gas shale recovery exploitation. Nevertheless, the probability to trap methane from Trans-Hudsonian HT metamorphism to basement uplift and erosion is low, and this scenario may not be favored; (ii) methane may have been produced at depth by downward flows of diagenetic aqueous fluids (not necessary the mineralizing brines themselves even if they represent a good candidate) which reacted with graphite. Production of such reducing agent through consumption of graphite by water has been extensively invoked in metallogenic models. One could argue that textural evidence of graphite consumption are very scarce within and around the U deposits (Martz et al., 2018). Note then that in the present scenario methane generation occurred in the basement much deeper than the actual sites of mineralization. Abrupt permeability increase of GSZF during seismogenic reactivation may have induced seismic pumping of basinal aqueous fluids and subsequent methane production at depth (Fig. 3). This downward flow was possibly favored by pre-existent high-permeability funnels or corridors around GSZF issued from the weathering of the basement before the deposition of the Athabasca sediments.

No structural and textural evidence of fluid overpressure regime has been reported during the U mineralizing stage. Therefore, GSZF might not behave as “classical” seismic valve implying a permeability barrier. Fault-induced pressure gradients (compaction, dilatancy) have been addressed for the U deposits through numerical modeling (Li et al., 2017). Such compaction might induce successive methane pulse during inter-seismic reloading of active segment (Fig. 3).

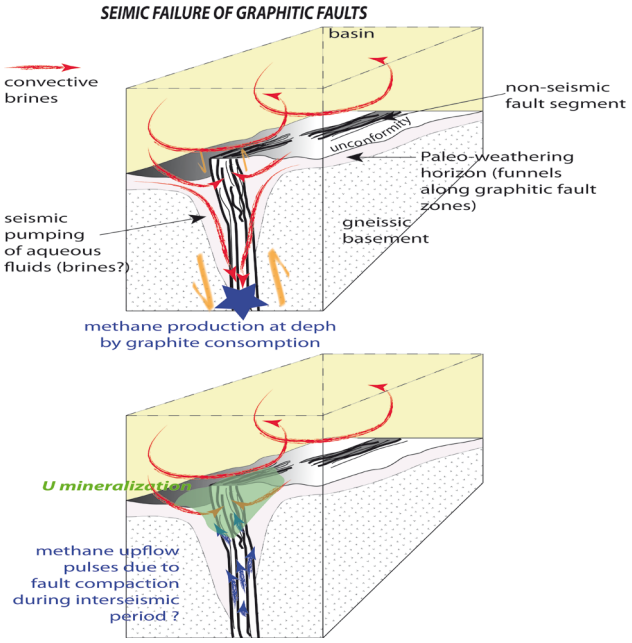

Figure 3. Proposed model for the formation of Athabasca giant U deposits implying seismic cycle and methane production and flow.

5 Numerical modeling

We performed transient numerical simulations in order to investigate impacts of such conceptual model on bulk hydrodynamics and thermal pattern. At this stage, the models were not designed to simulate brines penetration within the basement. We used a darcyan hydro-thermal coupling accounting for topography and buoyancy (temperature dependent fluid density) as fluid driving forces. The fault domains are vertical and extend through all the basement thickness. Seism’s along faults and subsequent methane-rich fluid discharges have been simulated through successive and abrupt fluid pressure variations of low amplitude at the basal limit of faults domains. Such single set up allows to roughly

reproduce successive seismic cycle and to explore how hydrodynamics are modified near the unconformity (Fig. 4). Benchmarks have been run based on the works of Li et al. (2016).

We found that for the cases in which topographic gradient controls the fluid flow in the basin, abrupt methane discharge from faults triggers thermal convection cells which tend to regulate the thermal and fluid flow regime. This result has important implication on brines availability and the extraction of U(VI) from basement through hydrothermal alteration. Indeed, convection cells likely increased the time integrated water/rock ratio and thus increased the mass transfer between fluids and rocks.

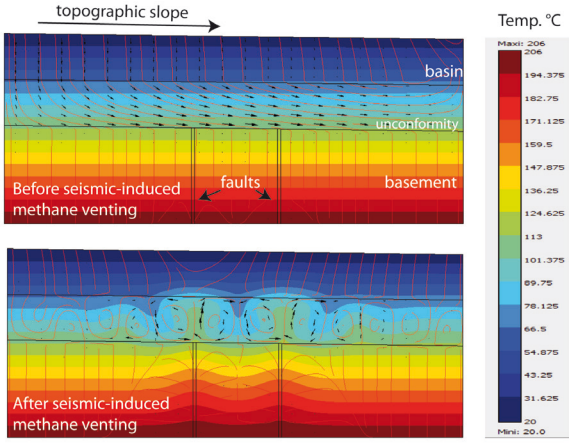

Figure 4. 2D Hydro-thermal modeling simulating seismogenic methane discharge near the basin/basement unconformity. Black arrows: l fluid velocity (normalized), red lines are streamlines.

References

Alexandre P, Kyser K, Thomas D, Polito P, Marlat J (2007) Geochronology of unconformity-related uranium deposits in the Athabasca Basin, Saskatchewan, Canada and their integration in the evolution of the basin. Mineralium Deposita 44:41–59.

Dargent M, Truche L, Dubessy J, Bessaque G, Marmier H (2015) Reduction kinetics of aqueous U(VI) in acidic chloride brines to uraninite by methane, hydrogen or Cgraphite under hydrothermal conditions: implications for the genesis of unconformity-related uranium ore deposits. Geochim. Cosmochim. Acta 167: 11‐26.

Derome D, Cathelineau M, Lhomme T, Curley M (2003) Fluid inclusion evidence of the differential migration of H2 and O2 in the McArthur River unconformity-type uranium deposit (Saskatchewan, Canada). Possible role on post-ore modifications of the host rocks. J. Geochem. Explor. 78–79:525–530.

Derome D, Cathelineau M, Cuney M, Fabre C, Lhomme T, Banks, D (2005) Mixing of sodic and calcic brines and uranium deposition at McArthur River, Saskatchewan, Canada: a Raman and laser-induced breakdown spectroscopic study of fluid inclusions. Econ. Geol. 100:1529‐1545.

Gasperini L, Polonia A, Del Bianco F, Etiope G, Marinaro G, Favali P, Italiano F, Çağatay MN (2012) Gas seepage and seismogenic structures along the North Anatolian Fault in the eastern Sea of Marmara. Geochem. Geophys. Geosyst. 13(10):Q10018.

Geersen J, Scholz F, Linke P, Schmidt M, Lange D, Behrmann JH, Völker D, Hensen C (2016) Fault zone controlled seafloor methane seepage in the rupture area of the 2010 Maule earthquake, Central Chile, Geochem. Geophys. Geosyst. 17:4802–4813.

Géli L et al (2008) Gas emissions and active tectonics within the submerged section of the North Anatolian Fault zone in the Sea of Marmara, Earth Planet. Sci. Lett. 274:34–39.

Khairallah C (2017) The Cigar North conductor (Cigar Lake Trend, East Athabasca): macro/micro-structural characteristics, mineralogy and relationships with hydrothermal alterations, Msc Thesis, unpublished, Univ. Orleans, France.

Hoeve J, Sibbald T (1978) On the genesis of Rabbit Lake and other unconformity-type uranium deposits in northern Saskatchewan, Canada. Economic Geology 73:1450–73.

Jeanneret P, Goncalves P, Durand C, Trap P, Marquer D, Quirt,D, Ledru,P (2016) Tectono-metamorphic evolution of the pre-Athabasca basement within the Wollaston‐Mudjatik Transition Zone, Saskatchewan. Can. J. Earth Sci. 53:231‐259.

Jefferson CW, Thomas DJ, Gandhi SS, Ramaekers P, Delaney G, Brisbin D, Cutts C, Portella P, Olson RA. (2007) Unconformity-associated uranium deposits of the Athabasca basin, Saskatchewan and Alberta. Geological Association of Canada, Mineral Deposits Division, Special Publication No. 5, pp. 273-305.

Li Z, Chi G, Bethune KM (2016) The effects of basement faults on thermal convection and implications for the formation of unconformity-related uranium deposits in the Athabasca Basin, Canada. Geofluids 16(4):729-751.

Li Z, Chi G, Bethune KM, Zenghua L, David T, Gerard Z (2017) Structural Controls on Fluid Flow During Compressional Reactivation of Basement Faults: Insights from Numerical Modeling for the Formation of Unconformity-Related Uranium Deposits in the Athabasca Basin, Canada. Economic Geology 112(2) :451-466.

Martz, P., 2017. Caractéristiques, chronologie et rôles des circulations fluides dans le bassin d'Athabasca et son socle : implications dans la formation et l'évolution du gisement d'uranium de Cigar Lake. Unpublished PhD, INPL, Nancy, France.

Martz P, Cathelineau M, Mercadier J, Boiron MC, Jaguin J, Tarantola A, Demacon M, Gerbeaud O, Quirt D, Doney A (2017) C‐O‐H‐N fluids circulations and graphite precipitation in reactivated Hudsonian shear zones during basement uplift of the Wollaston-Mudjatik Transition Zone: example of the Cigar Lake U deposit. Lithos 294‐295:222‐245.

Martz P, Mercadier J, Cathelineau M, Boiron MC, Quirt D, Doney A, Gerbeaud O, De Wally E, Ledru P. (2018) Formation of U-rich mineralizing fluids through basinal brine migration within basement-hosted shear zones: A large-scale study of the fluid chemistry around the unconformity-related Cigar Lake U deposit (Saskatchewan, Canada). Chemical Geology 508:116-143.

Pagel M (1975) Détermination des conditions physico-chimiques de la silicification diagénetique des grès Athabasca (Canada) au moyen des inclusions fluids. Comptes Rendus de l'Académie des Sciences, 280:2301–2304.

Richard A, Rozsypal C, Mercadier J, Banks DA, Cuney M, Boiron MC Cathelineau M (2012) Giant uranium deposits formed from exceptionally uranium-rich acidic brines. Nat. Geosci. 5:142–146.

Richard A, Boulvais P, Mercadier J, Boiron MC, Cathelineau M, Cuney M France-Lanord C (2013) From evaporated seawater to uranium-mineralizing brines: isotopic and trace element study of quartz–dolomite veins in the Athabasca system. Geochim. Cosmochim. Acta 113:38–59.

Rowe CD, Griffith WA (2015) Do faults preserve a record of seismic slip: A second opinion. Journal of Structural Geology 78:1-26.